DOCTOR OF PHILOSOPHY

Analysis and Modelling of a Type II White-light Solar Flare

Procházka, Ondrej

Award date:
2019

Awarding institution:
Queen's University Belfast

Analysis and Modelling of a Type II White-light Solar Flare

A thesis submitted for the degree of
Doctor of Philosophy

by

Mgr. Ondřej Procházka
(Univerzita Karlova v Praze 2015)

Faculty of Engineering and Physical Sciences

Astrophysics Research Centre
School of Mathematics and Physics
Queen's University Belfast
Belfast, Co. Antrim, Northern Ireland

March 2019

Acknowledgements

This research did not only bring an extension of our knowledge of solar flares, it did not correct some of the old partialities that my fellow scientists expressed in their works. This thesis is actually an embodiment of my deep belief that if we work hard, we can reach any goals. We shall never get scared when facing a big challenge, we shall never let anyone to discourage us from fighting for what we believe in.

When I was a schoolboy, some members of my family were doubtful when I told them I wanted to study at a grammar school. When I showed them that it was doable and told them that I wanted to study maths and physics, they did not think it was a very good idea. Well, I tried and failed, then again and again and after 5 years I passed all my exams. It was tough, at some moments it looked like a miracle, but it worked and was worth it. Not because I wanted to prove myself right, but because it allowed me to start my new life in Belfast shortly after I graduated.

After my first arrival in Northern Ireland I fought with many things in everyday life since everything was different than on the continent - from left-side traffic through washbasins with two taps - one with cold and one with hot water - up to an existence of a galaxy of local accents that made me think that I will never really understand English. But later on I noticed that life on Irish island is pretty similar to what I used to know, but without the residua from communism still persisting in behaviour of most Czechs, that made me feel unwelcome in the country where I was born.

Belfast became my home that I chose myself, not the one that was given by an accident at the moment of birth. This strong bound was probably created at the moment when I realised that in Ireland I have always been treated equally, even when it was obvious that I was not born there. For me this is a real value and I would like to thank to all Irish/N. Irish people for this.

Now I am just a step from being awarded a PhD degree. It is an achievement that my parents, grandparents or broader family do not even understand, since none of them has a higher education. It is a degree that demonstrates resilience and persistence a lot more than a knowledge of equations. It also brings responsibility and expectations from the society, especially in the current unstable world that needs wise leaders more than anything else.

I would like to thank to all my friends who made me feel happier than before my move to Belfast, especially my flatmates Ben, Daniel and Stefano, people from University Christian Outreach Paul, Peter, Jonasz, Tadhg, Kinga and Jason, my fellow

students from QUB Photosociety and Floorball Club Neil, Paula, Kevin, Paul and Saud, my colleagues Micha, Jamie, Mike and other people I met by accident but will never forget: Eleni, Jerry, David and many more.

I must not forget about my colleagues who helped me with my work and who co-authored my papers: Ryan Milligan, Aaron Reid, Paulo Simões, Adam Kowalski, Joel Allred and Pavel Kotrč. My special thank is for my supervisor Prof. Mihalis Mathioudakis, who gave an advice and freedom according to my needs, and more importantly secured funding for my research.

Abstract

Type II white-light flares (WLFs) are rare impulsive events in solar atmosphere observed across the electromagnetic spectrum, but without the characteristic emission in hydrogen lines. A unique set of multi-instrument observations is presented with broad wavelength range spectra in the visible and UV range. Data from the RHESSI and Fermi satellites provide evidence of both non-thermal electron and proton beams during the studied flare. The observations put important constraints on the beam parameters and allow a deeper investigation using radiative hydrodynamic modelling.

Radiative hydrodynamic simulations show that the observed flare signatures cannot be explained with 'standard' electron beams, since such beams deposit at least part of their energy in the upper chromosphere where hydrogen lines are formed. Instead, the models suggest that the beams penetrate through the upper chromosphere and deliver their energy directly into the lower chromosphere. Such beams can be dominated by both electrons and/or protons, but electron beams require rather exotic parameters. On the other hand, proton beams penetrate easily through the upper chromosphere and deliver enough energy to power the white-light emission while their energy flux can remain relatively low.

The models show that the previously reported time lag between the X-ray emission and WL emission is not a type II WLFs' feature, instead these events do not show radiative losses via Lyman emission originating in the top chromosphere. The WL continuum is dominated by free-bound hydrogen emission originating in the mid-lower chromosphere.

Contents

Acknowledgements **i**

Abstract **iii**

List of Tables **v**

List of Figures **vi**

Publications **vii**

1 Introduction **1**

1.1 Description of solar atmosphere 2

1.1.1 Atmospheric profile 3

1.2 Solar flares 5

1.2.1 Flare evolution and classification 5

1.3 White-light flares 9

1.3.1 Flare continua 10

1.3.2 Previous studies of WLFs 12

1.3.3 Stellar flares 19

1.4 Diagnostics of particle beams 21

1.4.1 The role of protons in flares 27

1.5 Outline 31

2 Instrumentation **33**

2.1 Current ground-based instrumentation and solar flares 34

2.2 White-light observations 35

2.3 Spectroscopic instrument in the visible wavelength range 37

2.4 Ultra-violet wavelength range 42

2.4.1 SDO Extreme Ultraviolet Variability Experiment (EVE) 42

2.4.2 GOES/Extreme Ultraviolet Sensor 44

2.5 X-ray observatories 45

2.5.1 The Reuven Ramaty High-Energy Solar Spectroscopic Imager . 46

2.5.2 Fermi Gamma-ray Space Telescope 50

3 Data analysis **52**
3.1 The Balmer series of the 10 and 11 June 2014 X-class flares 53
3.2 Lyman series of the 10 and 11 June 2014 X-class flares 59
3.3 The HMI 617 nm continuum 61
3.4 X-ray spectroscopy 64
3.5 Summary 72

4 Radiative hydrodynamic modelling **74**
4.1 Radiative transfer equation 75
4.1.1 Thermodynamic equilibrium 77
4.1.2 Non-Local Thermodynamic Equilibrium 79
4.1.3 Continuum absorption coefficient 82
4.2 The RADYN code 84
4.3 The RH code 87
4.4 Contribution function 87

5 RADYN model atmospheres **90**
5.1 Initial atmosphere 91
5.2 Description of the particle beams 92
5.3 The effect of a return current 94
5.4 Attempts to reproduce the flare spectral signatures 96
5.4.1 Beam heating versus direct energy deposition 97
5.4.2 Beams with high low energy cutoff 102
5.5 Summary 104

6 Models constrained with observations **106**
6.1 Observational constraints 107
6.2 Electron beam-driven models 108
6.3 Proton beam-driven models 111
6.4 Contribution functions 113
6.5 Temperature profiles 115
6.6 Hydrogen continuum energy 115
6.7 Model uncertainties 117
6.8 Comparison with comparing codes 127
6.9 Summary 129

7 Concluding remarks and future work **130**

Bibliogrpahy **139**

List of Tables

1.1 Classification of flares by the soft X-ray flux registered with GOES. . . 8

2.1 Bandpass of EUVS's channel E on board of GOES13-15. 45
2.2 Comparison of RHESSI and Fermi observatories. The Fermi/GBM's temporal resolution is for CSPEC data type that provide high spectral resolution of 128 pseudo-logarithmically scaled energy channels (Yu et al. 2016). 47

3.1 Estimates of the power of non-thermal electrons in the impulsive phase of the flare and the derived maximum flux for given values of the low energy cutoff with respect to the HMI flaring area. 67
3.2 Fermi/BGO fitting results. $I_{E_p>30MeV}$ is a count rate of > 30 MeV ions averaged over the selected time interval. N_{30} is the total number of > 30 MeV ions detected. 71
3.3 Estimates of power in non-thermal protons during the impulsive phase of the flare and the derived maximum flux for given values of the low energy cutoff with respect to the HMI flaring area. 72

5.1 List of models with direct heating of TMR and lower chromosphere. A heating function used in the model marked with * is plotted in Figure 5.8. 101

6.1 Spectral diagnostics from electron beam-driven models 20 seconds into the simulation for a range of electron beam fluxes (F) and E_C. The signal presented in each waveband is the pure flaring signal relative to the initial/quiescent state. The models that comply with observations are typed in boldface. 109
6.2 Spectral diagnostics derived from proton beam-driven models for a range of proton fluxes and E_C. The data are presented in an identical way as in Table 6.1. 112
6.3 A summary of the beam parameters that are in best agreement with the observations. For the WL emission only the excess is quantified (4th, 5th and 6th columns). 114

6.4 Spectral diagnostics from electron beam-driven models 20 seconds into the simulation for a range of electron beam fluxes (F) and E_C. For the spectral diagnostics the intensity at an angle of 27.5° was used instead of the flux. 122

List of Figures

1.1 Temperature profile and formation heights of various spectral lines based on VAL-C (quiet solar) atmosphere. Reproduced from Vernazza et al. 1981. 4

1.2 A simplified schema of a solar flare showing the most important radiative processes. Reproduced from Dennis & Schwartz (1989). 6

1.3 An example of a WLF as captured by SDO/HMI (continuum at 617 nm) on 10 June 2014. 9

1.4 Three examples of WLF observations around the Balmer jump. The top spectrum shows a redward shifted Balmer jump, the middle shows an unshifted Balmer jump and the bottom spectrum does not show any signs of a Balmer jump. Reproduced from Hudson et al. (2010). 16

1.5 Penetration depth of electron beams in a VAL-C atmosphere. A&H 87 refers to the paper of Aboudarham & Henoux (1987). Reproduced from Fletcher et al. (2007b). 17

1.6 A flaring spectrum from 16 January 2009 megaflare on YZ CMi. The quiescent spectrum is plotted with purple colour and the red line marks the 10^5 K black-body fit. Reproduced from Kowalski et al. (2010). . . . 22

1.7 A typical X-ray and γ-ray spectrum of a large solar flare. At energies < 30 keV two thermal components dominate. The dashed straight line of different slopes at different energy bands represents bremsstrahlung from electrons. At energies of several MeV the de-excitation of nuclear lines dominate. At energies of several tens of MeV we can observe the decay of pions. Reproduced from Lin et al. (2002). 22

1.8 Effective ion energies for the 2.223 MeV neutron capture line and 4.44 MeV ^{12}C line production with respect to spectral index. The effective ion energy range is defined as a range where the yield fell to 50% of each side of the maximum. The horizontal line within each box marks the peak of the distribution. Reproduced from Murphy et al. (2007). . . 28

1.9 Locations of HXR and γ-ray sources in a X4.8 flare close to the limb. The background SOHO/MDI magnetogram was obtained 15 minutes before the flare. Reproduced from Hurford et al. (2003). 29
1.10 A schematic diagram of a magnetic loop with a charged particle moving parallel to the magnetic field and showing Larmor rotation. Reproduced from Aschwanden (2005). 30

2.1 The spectral profile of Fe I 617.3 nm line (black) together with six tuning position profiles of the filer (colour) spanning the range ±0.01725 nm from the line center. FWHM = 0.0076 nm, spacing 0.0069 nm. Reproduced from Schou et al. (2012). 36
2.2 A schematic diagram of the Image Selector. The light reflects from mirrors of a coelostat first and then is focused by a parabolic mirror to create a sharp image in a distance where IS is placed (red). Light that goes through the delimiting diaphragm is focused into an optical fibre that feeds up the spectrometer (blue). A small fraction of light is reflected from the glass wedge into the context imager (orange). Reproduced from Kotrč et al. (2016). 38
2.3 Front (left) and side (right) photographs of the IS. 39
2.4 HSFA2 telescope with covered mirrors. Light first hits the lower mirror that is fitted with a joint to allow declination adjustments. The upper mirror is sitting on a polar axis. Reproduced from Procházka (2014). . . 41
2.5 Correlation between Balmer continuum and Continuum 391 nm channels for two flares (X2.2 and X1.5 on 10 June 2014). Reproduced from Procházka (2014). 42
2.6 A schematic diagram of a part of EUVS. Detectors A and B are set on the opposite sides of the grating's optical axis. The same configuration is used for detectors C and D. Reproduced from Evans et al. 2010. . . . 46
2.7 A schematic diagram of the Rotating Modulation Collimators. Reproduced from Lin et al. 2002. 48
2.8 Positions of NaI (0 to 11) and BGO (12 and 13) detector units on board of Fermi. Reproduced from Meegan et al. (2009). 51

3.1 Observations of type I WLFs on 10 June 2014. Upper panel: Light curves of hard (black) and soft (red) X-rays from GOES. The vertical lines mark the times when the spectra and the images in the bottom panel were recorded. Bottom panel: The left column shows a context Hα filtergram, the second column shows the flare excess and the third column shows the excess related to a reference spectra taken at the end of observations, as recorded by the IS. The spectrum is integrated from the area within the bright circle. 54
3.2 Spectral profiles of Hγ, Hδ, H6 and Ca II K lines during the X1.5 flare peak. The vertical lines in the upper panel mark the colour coded times of spectra recording. The vertical axis on the lower panel is in relative units. 55
3.3 Observations of a type II WLF on 11 June 2014. For a description see a label of Figure 3.1. For all the snapshots a reference spectrum captured at 8:44 UT was used. The yellow bars mark the availability of UV/visible spectroscopic data. 56
3.4 Upper panel: Hα filtergram recorded at Kanzelhöhe Observatory, Austria, lower panel: colour coded light curves integrated over the Hα flare kernels. 57
3.5 Light curves of hydrogen emission (first and second panels) and the X-ray emission (third-RHESSI and fourth-GOES panels) of M3.0 and X1.0 events. Data in first, second and third panels are in relative units. The dashed green lines mark sudden brightenings (B1 and B2) in the Balmer continuum. The yellow bar highlights the type II WLF. 58
3.6 Observations of the X1.0 event. Description as in Figure 3.2. 59
3.7 The relative flare excess recorded during the flare peak (averaged over 9 : 04 : 45 – 9 : 05 : 15 UT). The reference spectrum was taken at 8 : 54 : 45 – 8 : 55 : 15 UT. The blue arrows mark heights of Ca II K line and half of the width of a fluctuation band, respectively. The red line marks the estimated level of continuum. 60
3.8 Light curves of GOES/EUVS Lyman α together with GOES X-ray data overplotted. 61
3.9 Spectral measurements in the EUV range during the studied event. The top panel shows the Lyman continuum and GOES HXR and SXR channels. The middle panel shows the flux in Lyman β, γ and δ lines as recorded by SDO/EVE. The lower panel shows the flux in Lyman α line as recorded by GOES. The vertical dashed lines show the flare peaks. 62

3.10 EVE spectra of X1-class flares. The upper panel shows a weak flare excess during the studied event, the lower panel shows another solar flare excess for comparison. The upper panel shows that the flare excess in all spectral lines is weaker compared to a 'typical' flare. The higher order Lyman lines and Lyman jump are hardly visible. 63
3.11 HMI image of the 10 June 2014 X2.2 event. The left panel shows an image of the solar photosphere taken at 11 : 39 : 40 UT. The right panel shows a difference image with the reference image taken at 11 : 38 : 10 UT. 64
3.12 HMI image of the 10 June 2014 X1.5 event. The left panel shows an image of the solar photosphere taken at 12 : 47 : 10 UT with red contours marking the WL kernels. The right panel shows a difference image with the reference image taken at 12 : 45 : 40 UT. 65
3.13 Emission in white-light from HMI. The upper filtergram shows the WL ribbons (green contours) with a location of the 40 – 70 keV HXR sources observed by RHESSI in time interval 9 : 04 : 14 – 9 : 04 : 40 UT (yellow contours). The lower panel shows light curves from the two WL ribbons (colour coded) and corrected count rate of the RHESSI 50 – 100 keV channel (grey). 66
3.14 HMI difference image with contours used to calculate the flaring area. . 67
3.15 RHESSI spectrum of the flare peak. The detector #7 was the least affected from the instrument degradation during this phase of the mission. In the upper panel the vertical lines show the energy interval within which the spectrum was fitted using the OSPEX software. The black line represents the data with the background subtracted and the red line represents the final fit. The green, yellow, pink, blue, purple and beige lines represents the fitted components - the thermal component, the non-thermal component, the Gaussian line, the pseudo function for fine-tuning RHESSI, the albedo and the pileup, respectively. The lower panel shows the fit normalised residua. 68
3.16 Graphical output of RHESSI fitting process with E_C fixed. The top panel shows light curves of the standard RHESSI energy channels, the following panels show results of the fitting process. The fits with different values of E_C are colour coded. 69
3.17 RHESSI 12 – 25 keV X-ray image of the 11 June X1.0 WLF peak (9 : 04 : 46 – 9 : 05 : 50 UT). The 30 – 60 keV white contours representing 0.5, 0.7 and 0.9 of the maximum signal are overlaid. An arc representing the flaring loop with the footpoints (contours) is clearly resolved. 70

3.18 The fitted Fermi/GBM spectrum in a time range 9 : 04 : 13 – 9 : 05 : 35 UT. The dotted lines mark an energy range used for the fitting process. The yellow line represents the sum of the fitted components that are the Gaussians for the 2.22 MeV (green) and the 511 keV (purple) lines, the power-law for the electron bremsstrahlung (purple), and the template for the de-excitation of nuclear lines (blue). 73

4.1 Notation for radiative and collisional transition rates between two energy levels in an atom. Reproduced from Hubeny (1997). 80
4.2 Absorption coefficient for bound-free transitions in neutral hydrogen atom. Reproduced from Rutten (2003). 83
4.3 Absorption coefficient of bound-free transition in negative hydrogen ion. Reproduced from Gray (2005). 85
4.4 Contribution functions (marked as shadows) of Hα (upper panel) and Hγ (lower panel) lines in the quiet atmosphere. Darker shades represent areas with a higher contribution. The red lines marking the surface of optical unity show that the Hα core originates purely in the top chromosphere, meanwhile the Hγ core is formed through a broad range of heights with the major contribution from the photosphere. The total contribution function in the lower right window of both panels composes of the components in the other three windows, as described in Equation 4.42. 89

5.1 Temperature (upper panel) and density (lower panel) profiles of the VAL-C atmosphere (solid line) and the active region-like atmosphere (QS.SL.LT and QS.SL.HT, respectively, from Allred et al. 2015, dashed line). 93
5.2 A comparison of the temperature profiles after the application of electron beams defined by McTiernan & Petrosian (1990) (black) and Emslie (1978) (red). The legend shows the beam flux in units of erg cm^{-2} s^{-1} and the E_C. The dotted line marks the initial temperature profile. . . 95
5.3 The effect of the return current (RC) on the Hγ line profiles. The upper and lower figures show the output of the electron and proton beam-driven models, respectively. The legend shows the beam flux in the units of erg cm^{-2} s^{-1} and E_C. The dotted line marks the initial line profile. 97

5.4 The effect of the return current (RC) on the atmospheric temperature profiles in the electron beam-driven simulations. The legend shows the beam flux in the units of erg cm^{-2} s^{-1} and E_C. The dotted line marks the initial temperature profile. 98
5.5 Synthetic spectra showing the difference between the standard electron beam heating and direct heating in the TMR. 98
5.6 Relative flare excess consisting of quiet and flaring contribution for beam heating and TMR direct heating. For filling factor see legend. . . 99
5.7 Temperature profile of the atmosphere 10 s into the simulation for a model with $F = 3.5 \times 10^{11}$ erg cm^{-2} s^{-1}, E_C = 20 keV, $\delta = 3$ electron beam (upper plot) and direct heating (lower plot). 100
5.8 Sample heating function with a lower boundary of heating at 600 km and peak of heating function of 8000 erg cm^{-3} s^{-1} that emulates a beam with a flux of 1.3×10^{11} erg cm^{-2} s^{-1}. 101
5.9 Profiles of the Hγ line in models of direct heating, as described in Table 5.1. The dotted line marks the quiescent profile. 102
5.10 Synthetic spectra from models of direct heating with a lower boundary of energy deposition at 300 km above photospheric floor. Filling factor = 0.04. 103
5.11 Hγ line profiles from models with high E_C. The legend shows the beam flux in units of erg cm^{-2} s^{-1} and E_C. The models with $E_C < 1$ MeV are driven by electron beams, the remaining models are driven by proton beams. The dotted line represents the quiescent line profile. 104
5.12 Temperature profiles of the models with high E_C. The legend shows the beam flux in units of erg cm^{-2} s^{-1} and E_C. The models with $E_C < 1$ MeV are driven by electron beams, the remaining models are driven by proton beams. The dotted line marks the initial temperature profile. . . . 105
5.13 Relative flare excess for models with high E_C. The legend shows the beam flux in units of erg cm^{-2} s^{-1} and E_C. The models with $E_C < 1$ MeV are driven by electron beams, the remaining models are driven by proton beams. The filling factor was 0.07. 105

6.1 Relative flare excess for electron beam-driven models for a filling factor of 0.07. 110
6.2 Pure Hγ line profiles for electron beam-driven models 20 s into simulation. The title of each box label beam flux in erg cm^{-2} s^{-1}. E_C is colour coded. The dotted line marks quiescent profile. 111
6.3 Pure Hγ line profiles for proton beam-driven models. The description is identical to Figure 6.2. 113

6.4 Relative flare excess for proton beam-driven models for a filling factor of 0.07. 114
6.5 Contribution functions to continuum at 615 nm of the favoured electron (e^-) and proton (p^+) beam-driven models. 115
6.6 Temperature profiles for the electron beam-driven models (panels a, b, and c) and proton beam-driven models (panel d). The dotted line indicates the initial pre-flare atmosphere. 116
6.7 Radiative gains in the solar atmosphere due to the precipitation of electron (left) and proton (right) beams that are able to reproduce the observations (left: $F = 3\times10^9$ erg cm^{-2} s^{-1}, $E_C = 80$ keV, right: $F = 1\times10^{10}$ erg cm^{-2} s^{-1}, $E_C = 4$ MeV). 118
6.8 Radiative gains in the solar atmosphere due to the precipitation of electron beams. Left: $F = 3\times10^9$ erg cm^{-2} s^{-1}, $E_C = 40$ keV, right: $F = 1\times10^{10}$ erg cm^{-2} s^{-1}, $E_C = 80$ keV. 118
6.9 Ionising and heating rates in the solar atmosphere due to the precipitation of electron beams. Left: $F = 3\times10^9$ erg cm^{-2} s^{-1}, $E_C = 40$ keV, right: $F = 1\times10^{10}$ erg cm^{-2} s^{-1}, $E_C = 80$ keV. 118
6.10 Radiative gains (left) and total energy balance (right) in the solar atmosphere due to the precipitation of a standard electron beam ($F = 3\times10^{10}$ erg cm^{-2} s^{-1}, $E_C = 20$ keV). Radiative backwarming of the TMR due to the Balmer continuum absorption is located at heights $\sim 300-500$ km above the photospheric floor. 119
6.11 RH synthetic spectra of the higher order Balmer (Lyman) series and Balmer (Lyman) jump from both the models that are able to reproduce the observations and a typical type I WLF (green) are in the upper left (right) panel. Synthetic spectral profile of the Lyman α line is in the bottom panel. The legend shows the beam flux in the units of erg cm^{-2} s^{-1} and E_C in the units of keV. The models with E_C of tens (thousands) of keV are driven by electrons (protons). The dotted lines mark the quiescent profiles. 120
6.12 Energy loss ratios in the Lyman and Balmer continua (black) and Lyman and Balmer α lines (red) for electron beam-driven models. The legend denotes the electron beam flux. 121
6.13 Geometry of the modelled atmosphere. Arrows show the directions in which the intensity was calculated (27.5°, 60° and 83.5°), the atmosphere's axis matches the vertical line. 122

6.14 RH contribution functions for Ca II K (left) and Hγ (right) lines in the F = 3×10^9 erg cm^{-2} s^{-1}, E_C = 100 keV electron beam-driven model (upper row) and the F = 1×10^{10} erg cm^{-2} s^{-1}, E_C = 4 MeV proton beam-driven model (lower row). The $\tau = 1$ surface and line profile are marked with red and green, respectively. The areas with darker shadow contribute to the total intensity greater than areas with lighter shadow. . 123
6.15 Estimates of Hα filling factor during the flare peak when threshold for flaring pixels equal to 2*median (upper left) and 2.2*median (upper right) are applied. Bottom picture: original image recorded at 9 : 04 : 32 UT. Flare area is red coloured. 124
6.16 Evolution of the Hγ line profile in electron beam-driven models with a flux equal to 3×10^9 erg cm^{-2} s^{-1}. 126
6.17 Evolution of the Hγ line core in selected electron beam-driven models (left panels) and proton beam-driven models (right panels). 127

7.1 Positions of electron (upper panel) and proton (lower panel) beam-driven models along with values of low energy cutoff in a phase diagram showing observational constraints. Green and yellow areas mark parts of the parameter space with Hγ vs. Ca II K ratio greater than 0.1 and WL contrast at 615 nm lower than 1.05, respectively. The models out of range of RHESSI and Fermi constraints are marked with red crosses. 132

Publications

A list of publications resulting from the work undertaken during my time as a Ph.D student.

Refereed Publications

1. **Procházka, O.**, Milligan, R. O., Allred, J. C., et al.
   Suppression of Hydrogen Emission in an X-class White-light Solar Flare
   2017 ApJ **837** 46

2. **Procházka, O.**, Reid, A. L., Milligan, R. O., et al.
   Reproducing Type II White-light Solar Flare Observations with Electron and Proton Beam Simulations
   2018 ApJ **862** 76

Non-refereed Publications

1. **Procházka, O.**, Milligan, R. O., Mathioudakis, M., et al.
   Suppression of Hydrogen Emission in a White-light Solar Flare
   2016, American Geophysical Union, Fall General Assembly, abstract SH31B-2561

2. **Procházka, O.**, Milligan, R. O., Reid, A., et al.
   Modelling of Electron and Proton Beams in a White-light Solar Flare
   2017, American Geophysical Union, Fall General Assembly, abstract SH41A-2756

Chapter 1

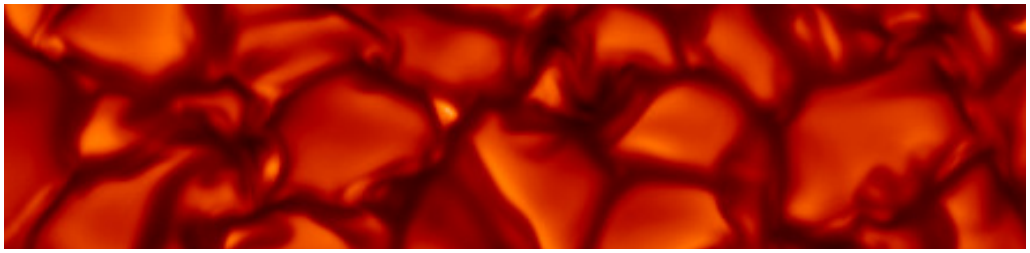

Introduction

An arrow can only be shot by pulling it backward. When life is dragging you back with difficulties, it means it's going to launch you into something great.

1.1 Description of solar atmosphere

The Sun is a main sequence star 4.57 billion years old (Bonanno et al. 2002). Its mass (1.9884×10^{30} kg, Luzum et al. 2011) puts it roughly in the middle between the very abundant red dwarfs like Proxima Centauri and the short lived blue giants like Spica or Bellatrix. The solar interior looks more like the interior of smaller stars with a zone in radiative equilibrium surrounding the core and a convective zone in the outer shell. In the case of the Sun the boundary between these two zones is at $\sim 0.7\ R_{\odot}$.

Chemical composition is crucial for the evolution of a star and becomes uniform when the star is fully convective before the nuclear reactions in the core begin. Since then the chemical composition in the core slowly changes but it remains constant in the outer layers, including the atmosphere. Thanks to that we can find out the initial chemical composition of most of main sequence stars from their spectra and hydrodynamical models (Asplund et al. 2009). The Sun is a G2 star with hydrogen and helium portions in the photosphere equal to 0.7381 and 0.2485, respectively, and metallicity equal to 0.0134 (portion of elements heavier than helium) which is lower than the previously thought value of 0.02 (Anders & Grevesse 1989).

The Sun's outer atmosphere can be divided into four layers:

- Photosphere

  This is an approximately 300 km thick base layer of solar atmosphere. Most of the radiation originates here and is observed mostly in the visual range. In the photosphere we observe granulation, sunspots and faculae fields. These features are manifestation of convective flows and magnetic fields. Their duration can vary from several minutes (granulation) up to several months (sunspots).

- Chromosphere

  The chromosphere is composed of gas with a temperature of about 10 000 K and its thickness reaches approximately 2 500 km. It can be observed in several narrow band filters, but Hα (656.3 nm) is the most common one. In this spectral

line filaments and prominences can be seen. These structures are basically lower temperature condensed clouds supported by the magnetic field.

- Transition region

  This is a thin layer of the solar atmosphere between the chromosphere and the corona, where we observe an increase in temperature from $\sim 10^4$ to 10^6 K. Due to the high temperature, all hydrogen is ionized and its lines can no longer be used as a diagnostic in this region. Instead, the transition region is imaged in C III (97.7 nm), O IV (103.2 nm) or Si IV (112.8 and 140.3 nm) lines, all in the UV range, unavailable from any ground-based instruments.

- Corona

  This is the outermost layer of the Sun's atmosphere with a quiet state temperature around 1 - 3 million K and much lower density compared to the photosphere and chromosphere. The corona can be observed in spectral lines of highly ionized species, such as Fe XIV (21.1 nm), Fe IX (17.1 nm) or Fe XII (19.3 nm). However, those observations have to be done by satellites as photons of these wavelengths are absorbed by the Earth's atmosphere. The corona can be also observed during rare solar eclipses or using coronagraphs. The general shape of the corona can reveal the phase of the solar cycle. Axial symmetry suggests a quiet phase but a more 'chaotic' structure is likely to appear during high solar activity.

1.1.1 Atmospheric profile

At the bottom of the photosphere, the frequency distribution of solar radiation follows the shape of the Planck function:

$$B_T(\nu) = \frac{2h\nu^3}{c^2} \frac{1}{e^{\frac{h\nu}{k_B T}} - 1}, \tag{1.1}$$

where ν is frequency, c is the speed of light, h is the Planck constant, k_B is the Boltzmann constant and T is the temperature. As the radiation travels through the atmo-

sphere, the frequency dependent absorption and transmission of radiation modify this distribution of radiation. The VAL-C atmosphere (Vernazza et al. 1981) is a semi-empirical model of the quiet solar atmosphere based on observations of multiple line and continuum diagnostics over a broad range of wavelengths and a solution of non-LTE (local thermodynamics equilibrium) optically thick radiative transfer equations. Figure 1.1 shows the VAL-C temperature profile together with the regions where the most important lines are formed. A characteristic minimum is located at a height of ~ 500 km above the photospheric floor and separates the photosphere and chromosphere, meanwhile the transition region lies at heights above 2000 km and separates the chromosphere from the corona. It also shows that well resolved observations of Ca II, Mg II or Hα line profiles are especially important, as they are used to constrain the temperature over a broad range of atmospheric heights. While many line cores are formed close or within the upper chromosphere, the formation of their far wings spans into the photosphere.

1.2 Solar flares

Solar flares are the most energetic events in the solar system. They take place in the solar atmosphere, but can affect interplanetary space in a great range via coronal mass ejections (CMEs), high energy radiation, protons and electrons.

Flares are driven by the reconnection of coronal magnetic fields and that is why we nearly always detect them in active regions (AR). These regions contain complex magnetic field configurations liable to destabilisation and in white-light (WL) we recognise them as groups of sunspots. In sunspots, convective motions are inhibited by the magnetic field, which in the umbra is mostly oriented perpendicular to the solar surface. In such a situation the plasma loses energy due to radiation, which leads to a temperature drop (down to ~4,000 K) with a corresponding drop in intensity in the visible range. ARs typically have a lifespan of several days or weeks and during that time they can release their magnetic energy by producing several solar flares.

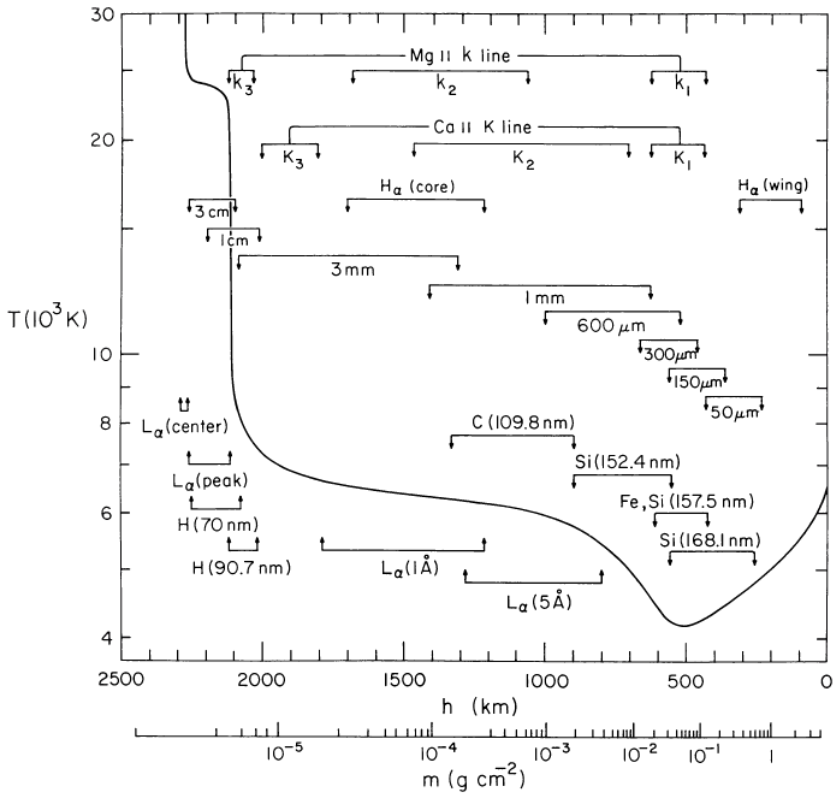

Figure 1.1: Temperature profile and formation heights of various spectral lines based on VAL-C (quiet solar) atmosphere. Reproduced from Vernazza et al. 1981.

1.2.1 Flare evolution and classification

The so-called *CSHKP* model by Carmichael (1964), Sturrock (1966), Hirayama (1974) and Kopp & Pneuman (1976) was introduced more then 40 years ago and was extended by Shibata (1999) and others. In this model a flare is triggered by *filament activation*, where a filament rises in the corona and stretches the magnetic field that it is connected to. The surrounding plasma is sucked into the space under the filament together with the magnetic field. This leads to an increase of magnetic flux as well as its gradient, creating a current sheet and finally magnetic reconnection. During this process the excess energy of the magnetic field is released in the form of heat, accelerating charged particles down to the chromosphere and the release of a magnetic cloud into interplanetary space. A place where accelerated charged particles hit the upper chromosphere (so-called *a footpoint* of a magnetic loop) is heated and can be seen in the Hα line. Because the filament is a 3D structure, a flare is developed along its whole length and

we observe a couple of ribbons - line of footpoints retreating from each other as the flare develops and the reconnection point rises in the corona. A schematic diagram can be seen in Fig. 1.2.

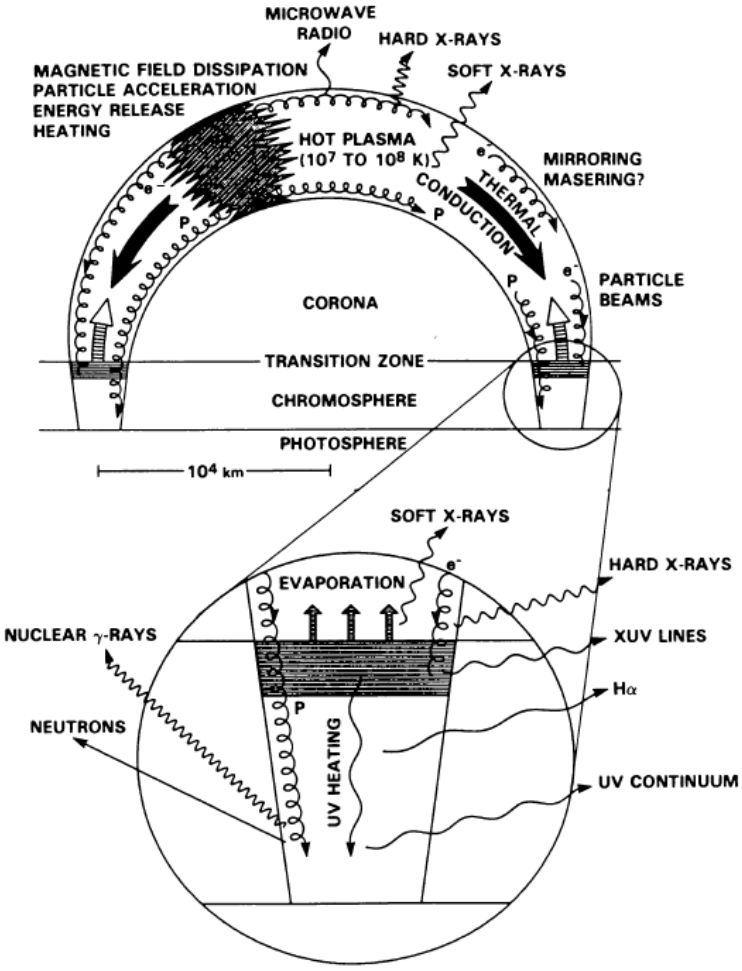

Figure 1.2: A simplified schema of a solar flare showing the most important radiative processes. Reproduced from Dennis & Schwartz (1989).

As described by Fletcher et al. (2011), according to both observational features and theory, flares have three stages:

- Onset phase

  During this phase the filament activation occurs together with a small brightening in ultra-violet (UV) and soft X-rays (SXR) detectable with instruments, which provide spatially resolved data, up to 30 minutes before the flare. It is connected

with the destabilization of the magnetic field. Broadening of spectral lines can also be detected.

- Impulsive phase

  During these few tens of seconds up to a few minutes, most of the total energy is released. In γ rays, hard X-rays (HXR) but also in microwaves, chromospheric lines and continua, we register a significant increase of flux coming from the footpoints. Very large movements of plasma are often registered.

- Gradual phase

  During this phase, characteristic loops appear in the corona. The timing of the loops depends on their temperature. First we detect them in SXR peaking immediately after the impulsive phase. Later, as their temperature drops, the loops appear in EUV wavelengths and finally in the Hα line.

After this phase a process called *chromospheric evaporation* occurs. Chromospheric plasma heated by charged particles evaporates and fills magnetic loops - a newly created magnetic structure. Very often we can observe an arcade of loops filled with very hot plasma which radiates even in soft X-rays.

It it estimated that the energy released in a flare can reach over 10^{25} J. Most of this energy (around 50 %) is spent on the acceleration of matter, around 30 - 50 % on accelerated particles and only 1 - 10 % is irradiated.

Solar flares are classified based on the SXR (0.1 - 0.8 nm) flux registered with the *Geostationary Operational Environmental Satellite* (GOES). Their classification, in a logarithmic scale, is noted in Table 1.1.

The spectral records of typical flares in the visible range show prominent emission

Class	Flux registered in SXR $[W/m^2]$
A	$< 10^{-7}$
B	10^{-7} - 10^{-6}
C	10^{-6} - 10^{-5}
M	10^{-5} - 10^{-4}
X	$> 10^{-4}$

Table 1.1: Classification of flares by the soft X-ray flux registered with GOES.

in many lines, such as Balmer lines and Ca II K & H (393.37 nm and 396.85 nm, respectively). Large flares are described as events with strong emission in line cores and 'extensive' wings, while less powerful flares can show central reversals (CR). During the very early stage of the flare, a blue asymmetry is observed in the Hα line and later on this develops into a red asymmetry (Švestka 1966a).

Early solar flare models attempting to reproduce the radiative emission were based on a homogeneous plane-parallel atmosphere. Machado & Linsky (1975) included a three-level hydrogen atom and a five-level calcium atom and suggested an increase in the temperature of the TMR and even of the photosphere of up to ~300 K during flares. They found significant changes in the atmospheric structure, especially in the transition region and upper chromosphere. These layers are pushed lower in the atmosphere and the pressure and density get enhanced by factors of 60-600. Both effects become more pronounced with the energy of the flare. Their observations of Ca II H & K lines suggest a great variety of conditions in the studied events. The lines can have single or three peaked profiles as well as double-reversed profiles. Several small spikes at the line cores close to the resolution limit were also observed and suggest an inhomogeneity of the active region. They also found that macroscopic motions have to be taken into account.

Using more precise partial redistribution (PRD) calculations of the Ca II K profiles, Machado et al. (1978) confirmed these conclusions and speculated that the TMR can be heated by EUV radiation originating in the corona or proton beams with energies ~10-20 MeV or a localised heating in the deep layers. Electron or lower energy proton

bombardment, or irradiation by soft X-rays were considered as ineffective to deliver energy sufficiently deep into the atmosphere.

1.3 White-light flares

Some of the energetic flares will often produce brightenings in the continuum in the visible. Such an event was first reported by Carrington (1859) who observed brigthenings lasting 5 minutes with a rapid onset. The two sources travelled about 56 000 km during that time. The next day it was followed by *a great magnetic storm* on both hemispheres. It was estimated that during this event an energy of $\sim 10^{32}$ erg was released (Tsurutani et al. 2003).

A presence of increased continua during flares puts several constraints on the physics involved, with the main problem to be the delivery of significant amounts of energy into the deeper layers of the solar atmosphere (up to $2{\times}10^{29}$ erg s^{-1}, Neidig 1989) that is needed to power the WL emission. An example of a recent white-light flare (WLF) recorded by SDO is in Figure 1.3 .

1.3.1 Flare continua

The analysis of flare spectra often requires differentiating between the various type of continua. This can be quite difficult especially for low resolution observations. A black-body continuum with T = 5777 K is always present, but on top of it another continuum or continua may be registered. The relative importance of these continua can change during the flare, as proposed by Kowalski et al. (2012), who described a temporal anti-correlation between the black-body continuum and Balmer continuum during a stellar megaflare.

- Hydrogen free-bound continuum

  Free electrons in the ionized plasma can recombine with hydrogen ions (protons)

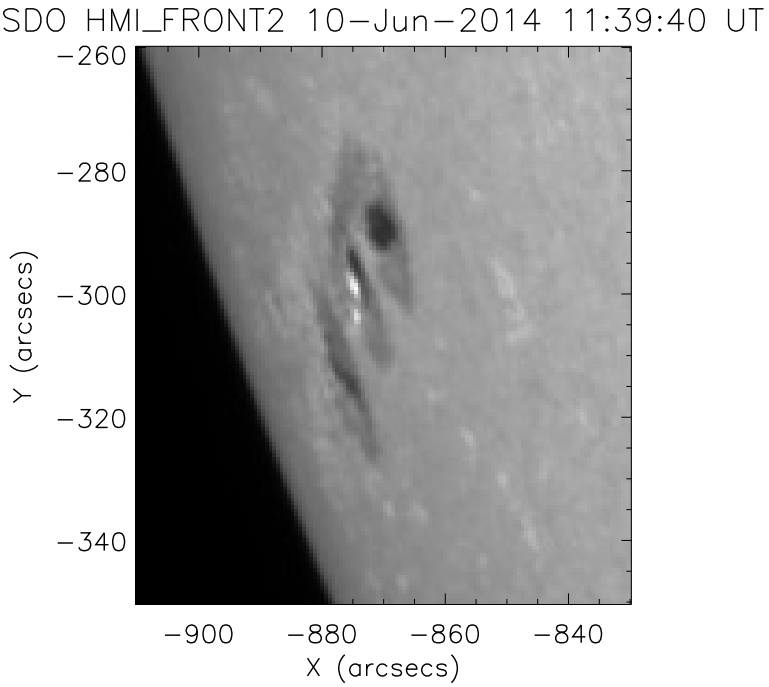

Figure 1.3: An example of a WLF as captured by SDO/HMI (continuum at 617 nm) on 10 June 2014.

and get captured at energy level

$$E_n = -13.6\frac{1}{n^2}\,eV \tag{1.2}$$

where n is an integer and marks the energy level in the hydrogen atom. When an electron of initial energy E_e is captured at a given energy level, a photon with energy

$$E_\nu = E_e - E_n \tag{1.3}$$

is emitted. Such a photon forms the so-called *Lyman continuum* when captured at $n = 1$, *Balmer continuum* for $n = 2$ or *Paschen continuum* for $n = 3$. The intensity of the continua is the highest for $E_e = 0$ and decreases towards to shorter wavelengths due to Boltzmann distribution of energies:

$$f(E_e) \sim e^{-\frac{E_e}{k_B T}} \tag{1.4}$$

- Black-body continuum

  As mentioned earlier, the solar spectrum can be in the first approximation described with the Planck function (Equation 1.1) where T = 5777 K (Cox & Pilachowski 2000). However, during a flare the active region gets heated and the spectrum changes its shape due to the presence of a black-body component with higher temperature. This change can be detected and the temperature of this component can be calculated.

- Negative hydrogen ion

  The radiation of the negative hydrogen ion (H^-) was used as a possible explanation for the WL emission lasting several minutes during the flare peak and the small scale brightenings that accompany large or small flares or appear in plage regions independently on flares. Švestka (1966b) came to the conclusion that in large flares the H^- ion can be responsible for WL emission if it originates at heights where the electron temperature is not greater than 7500 K. Such low temperatures are found rarely and only very deep in the chromosphere. He concluded that close to the limb such a continuum would reach its maximum intensity at $\lambda \approx$ 450 nm, while the relative intensity would decrease with increasing wavelength over the whole visible range. For the disc centre the relative maximum would be found at $\lambda \approx 550$ nm.

- Blue continuum

  The observed Balmer line broadening due to the Stark effect (Griem et al. 1959) can cause merging of the higher order Balmer lines and create a so-called *pseudo-continuum* or *blue continuum* at $\lambda < 400$ nm. This effect can help explain the shape of the measured continuum in some flares (Donati-Falchi et al. 1985). The effect is caused by local electric fields in the surrounding of the emitting atoms and can be seen even in weakly ionized plasma when the temperature is relatively low (for higher temperatures Doppler broadening becomes more dominant). The intensity of the effect strongly depends on the concentration of the charged parti-

cles and electron density, respectively. Kowalski et al. (2017) included a unified Stark effect theory for electrons and protons with an accurate electron perturbation treatment into the RH code (described in Section 4.3).

1.3.2 Previous studies of WLFs

Machado & Rust (1974) and Rust & Hegwer (1975) published photographic observations of the strongest WLF up to that date. Their spectroscopic data covered a broad range of wavelengths (353 - 589 nm) and were accompanied with filtergrams at 495 and 590 nm. Even when they did not capture the bright kernels with their slit spectrographs, they were still able to see strong emission in the higher order Balmer lines up to H_{15}. They analysed the level of continuum and found that at wavelengths around the Balmer jump the measured WL excess reaches ~12 % of the non-flaring signal, while at wavelengths longer than 400 nm this was below 5 % (so-called blue-ish flare continuum). They found their WL spectrum to originate in an optically thin layer with a temperature of 8500 ± 500 K located in the lower chromosphere. They also found a close temporal correlation between the WL excess and HXR and microwave bursts.

More events were analysed in their subsequent study including some of lower importance (Machado & Linsky 1975). Using a homogeneous plane-parallel model of the solar atmosphere they found that their observations are best explained when the atmosphere gets compressed during flares, which moves the transition region and upper chromosphere (where many observed lines are formed) into regions with higher density. They concluded that heating plays a significant role, especially in the photosphere, where a significant portion of energy is released. However, their energy estimates indicated that it may not be possible to deliver the necessary energy into the photospheric region from the corona, where in the standard model the major portion of energy is released, since hardly any particles would be able to penetrate that deep and no other energy transport was plausible. Thus, they suggested that WLFs are at least partly powered with a source of energy located in the photosphere.

The last conclusion was later seconded by Boyer et al. (1985), who analysed an X1 class flare observed close to the limb. This flare showed narrow Balmer lines and no Balmer jump, which indicates relatively low density in the emitting layer. They attempted to explain the WL emission with a single layer model while assuming two possible WL contributors: Paschen continuum and H^- continuum. In the first case the geometrical thickness would have to be extremely large to reproduce the observed WL contrast. Together with the lack of Balmer jump, this scenario was discarded. Since optically thin H^- emission would require a huge energetic input into the photosphere, they proposed an explanation incorporating heating of the whole atmosphere below TMR, starting at the $\tau_{500nm} = 1$ layer with $\Delta T \approx 150$ K, that can be simply an extension of heating in TMR/lower chromosphere described by Machado & Rust (1974) above. However, the delivery of the energy needed for the above described temperature rise remained unexplained.

Based on spectral observations, Machado et al. (1986) identified two types of WLFs that they suspected to have different emission mechanisms. Type I WLFs are described as flares with strong and broad Balmer lines in contrast with type II WLFs, which have much weaker Balmer lines and a flat wavelength dependence. Any flare could be the mixture of both types. They assumed that type I WLF originated in the chromosphere at a temperature of about 10^4 K and were caused by free-bound transitions, but type II WLF originated deeper in the photosphere with density higher than 10^{15} cm^{-3} and with a strong H^- contribution.

Metcalf et al. (1990) studied the Mg I lines at 457.1 and 517.3 nm in five solar flares, and compared them with their pre-flare states. These lines are formed in the TMR and low chromosphere. They proposed eight heating and ionisation mechanisms including H^- absorption of photospheric radiation, dissipation of electric currents and Alfvén waves, heating by non-thermal electron and proton beams, soft X-rays and UV irradiation and chromospheric backwarming. They stressed the importance of the ionisation level in order to distinguish between them. For example, the dissipation of

Alfvén waves cannot cause ionization at the TMR, so the increased ionization must be caused by a different mechanism. On the other hand, the collisions of hydrogen with electron or proton beams can cause ionization of up to 10^{11} cm^{-3}. They concluded that the temperature and ionisation changes in the TMR during the studied flares were caused by chromospheric backwarming by Balmer and Paschen continuum. According to Aboudarham & Henoux (1986) electrons would need energies of at least 350 keV to deposit energy in the TMR. Proton energies must be concentrated around 10 - 20 MeV range to do the same (Machado et al. 1978). Since such particles are not sufficiently abundant in flares, these mechanisms were excluded from the interpretation.

More recent observations were mostly based on satellite data and often incorporated analysis of the energy balance. In one case stereoscopic observations allowed the identification of the height of the flare above photospheric floor (Martínez Oliveros et al. 2012). Observations of WLFs do not give a consistent image of the flaring mechanism and sometimes authors contradict each other with their conclusions. However, it should be stressed that they usually studied different events that in principle, could be of a different nature.

Reconnection in the lower atmosphere: Based on observations of three WLFs Fang & Ding (1995) concluded that, apart from the observed spectral differences, a temporal mismatch between the WL and HXR emissions can also be an indication of a type II WLF. Due to the great difficulty in obtaining a spectroscopic record of flares at shorter wavelengths, authors sometimes distinguish between type I and type II WLF by looking for a match between WL and HXR emissions and refer to this paper. Metcalf et al. (2003) presented observations from the broadband WL channel (170 - 1000 nm) of the *Transition Region and Coronal Explorer* (TRACE, Handy et al. 1999) complemented with data from the Hard X-ray Telescope (HXT, Kosugi et al. 1991) on board *Yohkoh*. They studied an X5.3 class flare and solely based on a close correspondence between the HXR and WL emissions, they deducted that particle beams were responsible for the WL emission, and that their event was a type I WLF. Assuming that particle beams

cannot be responsible for type II WLF Ding et al. (1999) proposed an alternative scenario incorporating an energy release in the lower layers of the solar atmosphere and supported it with numerical simulations (see also Li et al. 1997; Litvinenko 1999; Chen et al. 2001). They claimed that in such a flare the high-energy particles first excite and ionise the surrounding atoms, leading to a decline of continuum intensity (black-light flare). Later on, the atmosphere gets heated causing a rise in the continuum, which turns into a positive WL contrast once the particle bombardment stops. If the heating was not caused by non-thermal particle bombardment, then there would not be any decline during the initial stages of the flare.

Hao et al. (2012) supported the idea of localised heating in the lower atmosphere when presenting flare observations with *two-step magnetic reconnection*. Their M6.3-class WLF (even when identified as type I based on a ratio between continua) showed a positive contrast at 360 and 425 nm as well as in the core and ±0.05 nm wings of the Hα line. Their data were accompanied with radio observations at 3.79 GHz that showed a second major peak ≈15 minutes after the impulsive phase and magnetic field topology based on extrapolation from HMI images. Based on the location of the WL source within the magnetic map, they concluded that this event was triggered by a reconnection in a low lying field region and the delayed radio burst was associated with an erupting magnetic rope.

Importance of the Balmer jump: When determining the dominant radiative processes in WLF, particular attention must be given to the Balmer jump. Observations by Neidig (1983), Hiei (1982) and Machado & Rust (1974) in Figure 1.4 show very different results, since the Balmer jump is not always detected, and even when it is, it can be redshifted. As admitted by Hudson et al. (2010), there are very few observations of continua in WLFs, and those that exist, yield to the idea that the continuum originates in a thin layer heated by collisions and ionized by non-thermal particles. The wavelengths around the Balmer jump are of a special importance, as photons with such energies can penetrate deeper and heat the photosphere. Also, in some flares a large portion of en-

ergy can be irradiated in this waveband (Fletcher et al. 2007a). Machado et al. (1989) showed that the presence of Balmer jump is the important spectral diagnostic that indicates the ongoing process of energy transport via chromospheric backwarming. They found that this process is very efficient in delivering the energy into the upper photosphere that consequently contributes to the WL continuum in the from of H^- radiation.

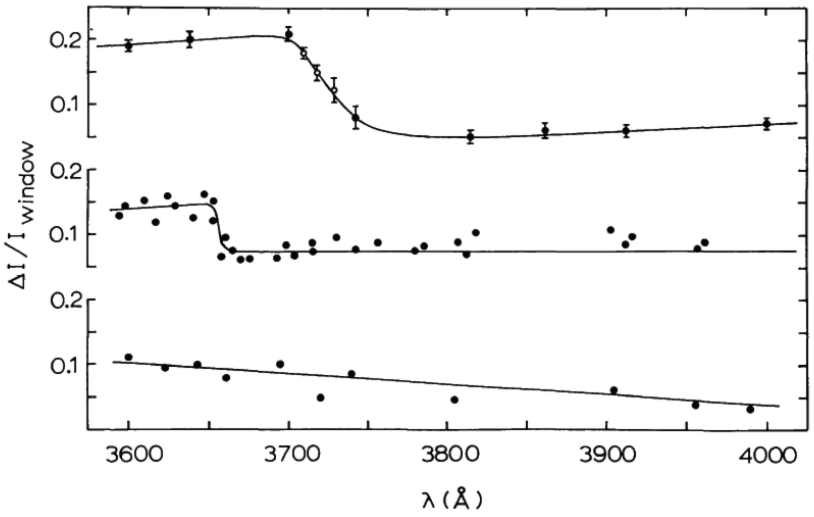

Figure 1.4: Three examples of WLF observations around the Balmer jump. The top spectrum shows a redward shifted Balmer jump, the middle shows an unshifted Balmer jump and the bottom spectrum does not show any signs of a Balmer jump. Reproduced from Hudson et al. (2010).

This problem was partly tackled by Heinzel & Kleint (2014), who first reported satellite observations of Balmer continuum with a temporal resolution of 75 s. They used data from the *Interface Region Imaging Spectrograph* (IRIS, De Pontieu et al. 2014) in rastering mode when observing an X1-class flare and found a positive continuum contrast reaching $100\% - 200\%$ at 281 nm. In their consequent study (Kleint et al. 2016) they found that both hydrogen recombination continuum and H^- contribute to the total emission, which is interpreted as contributions from both the chromosphere and photosphere. Based on RHESSI analysis they found that the total power in non-thermal electrons was $\approx 10^{28}$ erg s^{-1} while $E_C \approx 20$ keV. However, the energy in non-thermal

electrons was sufficient to power the WL emission even when E_C was equal to 40 keV.

Energetic balance: Studies of the energy balance in WLF may provide important constraints on the physics of the events. Based on observations of a set of large events in 1972, Lin & Hudson (1976) concluded that the bulk of the total energetic input into the deeper atmosphere is provided by electrons with energies $\sim$ 10 to 100 keV. Their pioneering work also states that protons do not contribute significantly to the energetic input as they are accelerated in the later stages of the flare. However, this statement is supported only by observations of a single flare in X-rays and γ-rays. Even when X-rays showed a bursty character in the impulsive phase of the flare, they had only four data points in γ-rays with a relative error of tens of percent. Their calculations showed that energy lost by protons was significantly lower than energy lost by electrons. On top of that they calculated that for a detectable WL emission (WL contrast = 1.05) an energetic threshold of $\sim 5 \times 10^{30}$ ergs in $>$ 20 keV electrons has to be overcome. Such a continuum would originate in the lower solar chromosphere as a result of free-bound transitions. Based on the work of Brown (1971), electron beams became generally accepted as the main drivers of the flare and the entity that delivers energy from the corona into the deeper layers. Proton beams were dismissed mainly due to a time lag (described in Section 1.4.1), though the temporal resolution of instruments capable to investigate γ-rays in that era was poor.

If particle beams are the main driver of flares, then their parameters are crucial for the development of the observational features - emission in lines and continua. Fletcher et al. (2007b) studied several moderate sized flares and analysed the electron beams of these events. They found that their E_C was in a range 13.5 to 22.9 keV and calculated their stopping depths (Figure 1.5). They concluded that in an undisturbed VAL-C initial atmosphere the beams cannot penetrate to depths where the Balmer-Paschen continuum is expected to be formed and suggested that some disturbances of the initial atmosphere in a pre-flare phase may be needed to let beams penetrate sufficiently deep.

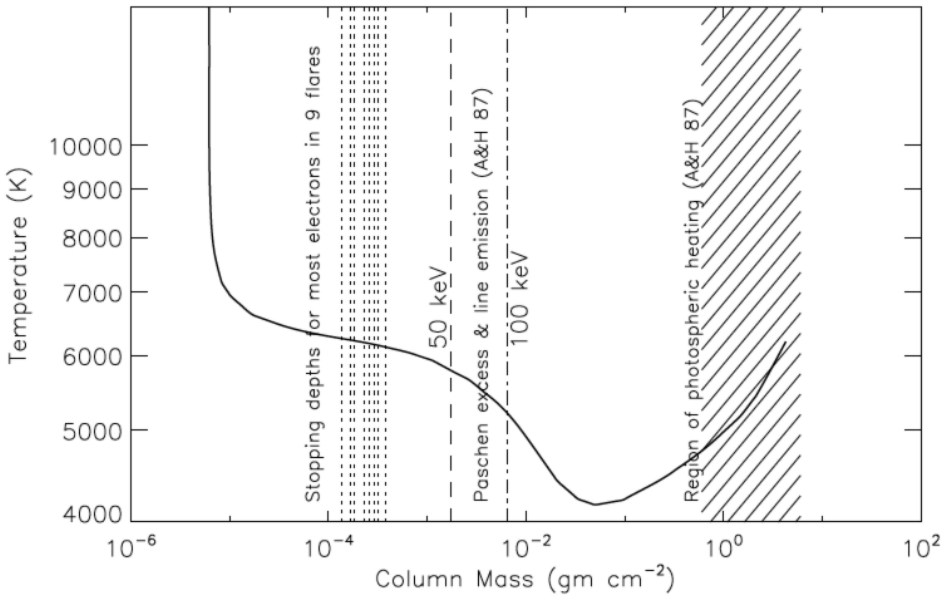

Figure 1.5: Penetration depth of electron beams in a VAL-C atmosphere. A&H 87 refers to the paper of Aboudarham & Henoux (1987). Reproduced from Fletcher et al. (2007b).

Statistical analysis: The first statistical study of WLFs using satellite data was presented by Matthews et al. (2003). Using *Yohkoh* observations they studied 28 WLFs and 31 non-WLFs. They found that high coronal pressure is a feature of WLFs and the power in electron beams was on average an order of magnitude higher in WLFs than in non-WLFs ($P_{WLF} = 1.29 \pm 2.25 \times 10^{29}$ vs. $P_{non-WLF} = 1.48 \pm 1.56 \times 10^{28}$ erg s^{-1}).

A similar work using more modern instruments was performed by Kuhar et al. (2016), who studied 43 rather stronger events (M and X class) and analysed features of their particle beams and WL emission. They found that HXR and WL emission were mostly co-spatial and co-temporal, at least within the cadence of HMI (45 s), and that HXR and WL fluxes correlate best for energies 30 keV. On top of that they found that there is a good correlation between energy deposited by electrons and WL emission for energies between 40 and 70 keV, and that for low energy electrons the correlation is significantly lower because such electrons do not penetrate sufficiently deep to generate the WL emission.

Stereoscopic observations: An attempt to measure the vertical extent of the emission in flares using observation of the limb was made by Martínez Oliveros et al. (2012), who used RHESSI data to identify the source of HXRs and images from HMI to locate the position of WL emission. The *Extreme Ultraviolet Imager* (EUVI, Wuelser et al. 2004) on board of *Solar-Terrestrial RElations Observatory* (STEREO-B) was fortunate to observe this flare from a different angle and was able to determine its heliographic longitude that allowed measurements of the distance between the flaring site and the photosphere at that longitude. Surprisingly, their analysis concluded that the HXR sources (> 30 keV) were located at 420 and 210 km, respectively, above the photosphere with an uncertainty of 240 km. This is well below the expected penetration depth of the electrons. The WL source was located just below the HXR sources - 230 and 160 km, respectively, with an uncertainty of 100 km. This suggests that in this flare the WL source was located at the photosphere.

Simple models: With regards to modelling efforts, attention shall be given to Potts et al. (2010), who used the *Michelson Doppler Imager* (MDI, Zayer et al. 1995) on board of the *Solar and Heliospheric Observatory* (SOHO) to observe photospheric variations along a ribbon and then tried to reconstruct the underlying photosphere. They subtracted the reconstructed photosphere from the measured one and calculated a correlation between the excess emission and the background along the ribbon. Their ribbon was found to be optically thin, as they were able to see the photospheric variations through the ribbon and concluded that it was located above the photosphere, in a region with high temperature far from LTE. Other models were presented by Kerr & Fletcher (2014), who attempted to determine the main WL contributor based on the analysis of *Hinode* Solar Optical Telescope (SOT, Suematsu et al. 2008) images with the RGB (red, green, blue) filter. They compared both the optically thick photospheric source scenario and the optically thin chromospheric slab scenario to estimate the power emitted in the flare and found that in the first case this would be of the order of 10^{26} erg s^{-1}, while in the second case it was $\sim 10^{27}$ erg s^{-1}. The optically thick scenario, where the radiating

source is described as the photospheric black-body component, is consistent with a rise in temperature of ≈ 200 K, but in the optically thin model the free-bound radiation is expected to provide the power output. However, in the later case there would be a slab in the mid-chromosphere with a temperature of ≈ 20 000 K during the flare peak. It is important to stress that their simple models do not allow radiative backwarming and while the first scenario looks plausible, their analysis was inconclusive as they could not explain how the necessary energy would be delivered into the photosphere.

More sophisticated models comprising both hydrodynamics and radiative transfer calculations are described in Chapter 4.2.

1.3.3 Stellar flares

The WL continuum is easier to detect in stars with lower effective temperature, because the fainter photosphere yields a higher flare contrast. The late spectral type stars (mostly M-class and K-class red dwarfs) are well known for their strong flaring activity. Results from NASA's *Kepler* Mission prove that all spectral type stars can have flaring activity (Van Doorsselaere et al. 2017). It was found that stars with large convective zones have the highest flare productivity (Pettersen 1989). Also, stars with faster rotation produce higher energetic flares and possibly a higher number of large spots suggesting a larger storage of magnetic energy (Candelaresi et al. 2014). But slower rotation does not exclude the possibility for the very high energetic event. The so-called superflares (events with an energy release $> 10^{34}$ erg) on solar-like stars were studied by Maehara et al. (2012), who found that such events occur in average once in 800 years, and events with energy release $> 10^{35}$ erg occur once in 5000 years.

The spectrum of the well-known flaring star AD Leo was studied by Mauas & Falchi (1996), who used the Pandora code (Avrett & Loeser 1992) to calculate the flare filling factor. When they assumed a filling factor 0.01, they found a good match between the observed and synthetic spectra for spectral features originating close to the stellar photosphere, like the Balmer line wings. But for the spectral features originating higher

in the atmosphere, e. g. Ca line profiles and Balmer decrement, a better match was found with the greater filling factor (0.05), which is consistent with solar observations (Mauas 1990).

One of the brightest stellar WLFs to day was observed by Kowalski et al. (2010) on M-class dwarf YZ CMi on 16 January 2009. They found the flare spectrum (Figure 1.6) to consist of a blackbody component (T $\approx$ 10 000 K), a Balmer continuum and the pseudo-continuum of the blended higher-order Balmer lines. They speculated that the Balmer continuum originates in the chromosphere, and the black-body component originates in the photosphere. However, in order to heat up the photosphere to reach the temperature of around 10^4 K, a significant energy input is required. Kowalski et al. (2015) introduced a new atmospheric model, better corresponding with the conditions on the M-class dwarf, and found that the flare spectrum can be reproduced with a non-thermal electron beam with energy flux of 10^{13} erg cm^{-2} s^{-1}. Such a beam is able to create a dense ($n > 10^{15}$ cm^{-3}) hot (12 000 - 13 500 K) layer in the dwarf's chromosphere ("chromospheric condensation") that produces a bright near-UV and optical continuum emission. Livshits et al. (1981) showed that such a layer would be created when the non-thermal electrons trigger a rapid downflow and a compression of the chromospheric material.

1.4 Diagnostics of particle beams

Magnetic reconnection in the corona typically leads to an acceleration of charged particles towards the denser layers of the solar atmosphere where they interact with the ambient plasma. Particles get de-accelerated (thermalised) in a process called *bremsstrahlung* (meaning "deceleration radiation"), which is a *free-free* interaction. In the case of electrons, they lose most of their energy in electron-electron Coulomb collisions when the density of plasma is sufficiently high (Holman et al. 2011). The hard X-ray emission that comes from loop foot-points is produced in electron-ion

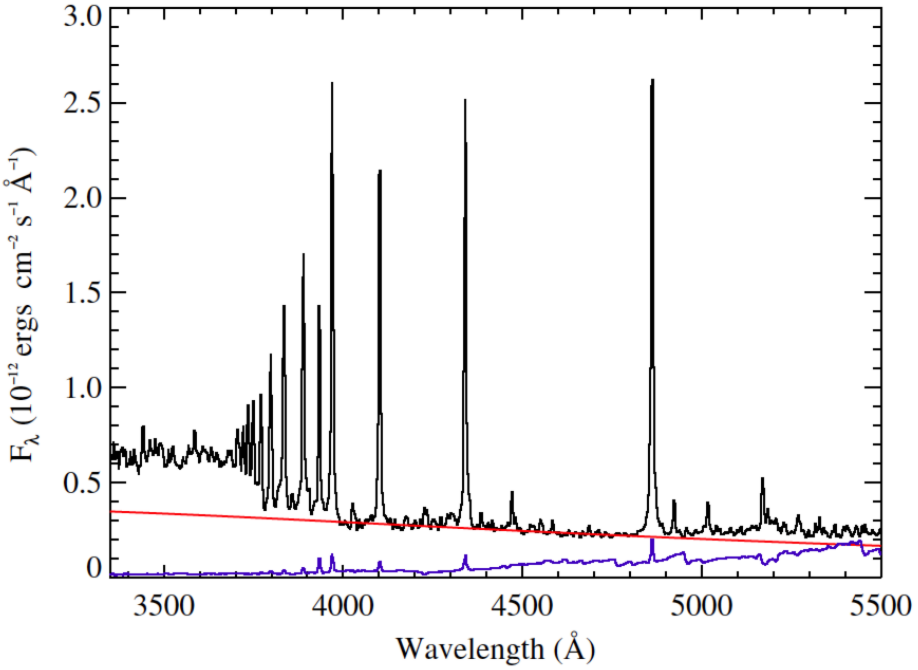

Figure 1.6: A flaring spectrum from 16 January 2009 megaflare on YZ CMi. The quiescent spectrum is plotted with purple colour and the red line marks the 10^5 K black-body fit. Reproduced from Kowalski et al. (2010).

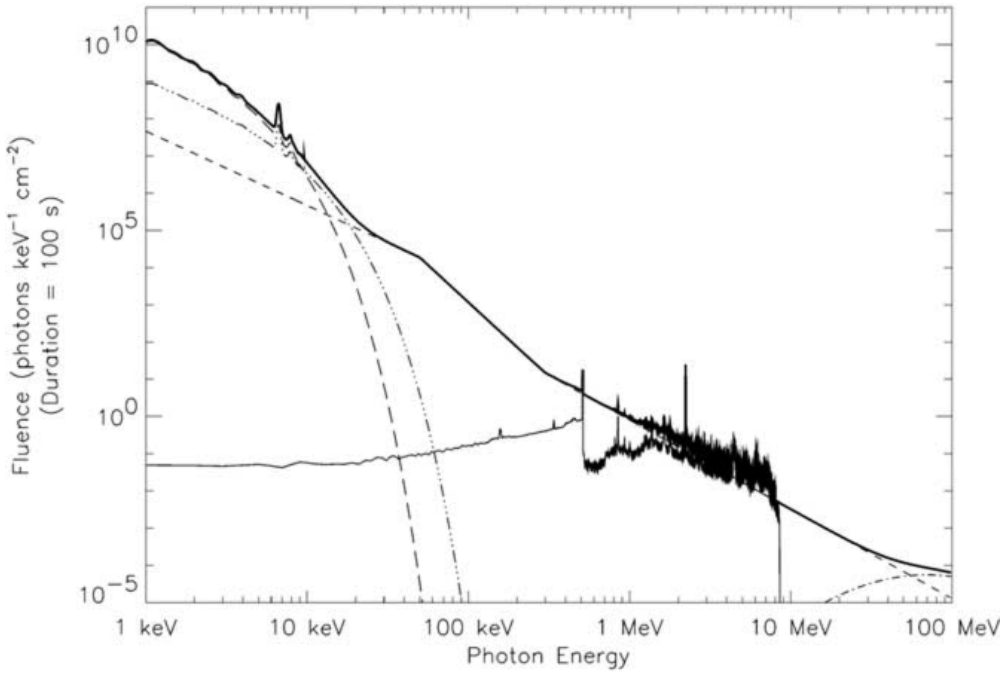

Figure 1.7: A typical X-ray and γ-ray spectrum of a large solar flare. At energies < 30 keV two thermal components dominate. The dashed straight line of different slopes at different energy bands represents bremsstrahlung from electrons. At energies of several MeV the de-excitation of nuclear lines dominate. At energies of several tens of MeV we can observe the decay of pions. Reproduced from Lin et al. (2002).

bremsstrahlung and serves as the main diagnostic tool for beam investigations.

To describe bremsstrahlung in the majority of solar flares, we commonly use the so-called "*collisional thick-target model*" (Brown 1971) under a condition of spatially indistinguishable target, in which an electron loses its supra-thermal energy (Peterson & Winckler 1958). Assuming that the observational integration time is longer than the time needed for energy losses to reduce all electron energies to less than E, the non-thermal electrons injected into the source region emit an HXR photon spectrum given by

$$I_{thick}(E) = \frac{1}{4\pi R^2} \int_E^\infty F_0(E_0) \nu(E, E_0) dE_0, \tag{1.5}$$

where $F_0(E_0)$ is the electron spectrum and $\nu(E, E_0)$ is the photon yield from a single electron of energy E_0 (Holman et al. 2011).

However, the electron spectrum can be well fitted with a single (or double) power-law model:

$$F_0(E_0) = A E_0^{-\delta}, \tag{1.6}$$

while the observed X-ray spectrum may be approximated as

$$I_{non-themral}(E) = I_0 E^{-\gamma}, \tag{1.7}$$

where A and δ are the parameters of the model.

In the thick target model the spectral indices are linked as

$$\gamma_{thick} = \delta - 1. \tag{1.8}$$

The following equation provides the power of non-thermal electrons

$$P_{non-thermal} = \kappa_E \int_{E_c}^{+\infty} E_0 F_0(E_0)\, dE_0 = \frac{\kappa_E A}{\delta - 2} E_c^{-\delta+2} \text{ erg s}^{-1}, \tag{1.9}$$

where $\kappa_E = 1.60 \times 10^{-9}$ is a constant, is valid for $\delta > 2$ and low energy cutoff $E_c > 0$.

The assumption for $\delta > 2$ complies with observations (Dennis 1985, Lin & Schwartz

1987, Winglee et al. 1991, Holman 2003).

Equation 1.9 shows that the determination of E_C is vital for the calculation of the power in the particle beams. We routinely assume a sharp low energy cutoff ($F_0(E_0) = 0$ for $E_0 < E_c$). According to Saint-Hilaire & Benz (2005) the shape of the electron distribution below E_C is not significant for the energetics of the flare (difference in P_{nth} between sharp cutoff and turnover model is less than ~20%), mainly due to much stronger contribution of a thermal component at lower energies. Currently there are no broadly accepted sharp constraints on E_C based on observations, since an analysis of RHESSI data can provide only a range of E_C values where the actual E_C lies (Ireland et al. 2013). Typically, the measured values of E_C in flares are in the interval from several keV up to ~100 keV. Warmuth & Mann (2016) studied 24 flares ranging from class C3.4 up to X17.2 and determined the median E_c to be 24.5 keV with only 7% of flares with E_C greater than 40 keV. However, an observation of a flare with $E_C > 100$keV during the later stages was recorded by Warmuth et al. (2009). Some authors use values even higher (500 keV) to model stellar megaflares (Kowalski et al. 2017).

At the magnetic reconnection site, the temperature can reach up to 40 million K due to the so-called *primary heating*. However, because of the low density plasma in the corona, we usually do not register SXR flux coming from this heated region. According to Aschwanden (2005), the typical coronal plasma temperature during a flare is in the range of $T_e \approx 10 - 30$ MK, which corresponds to energies $E = k_B T \approx 0.9 - 2.6$ keV. When the upper chromosphere becomes heated by precipitating particles, we observe the so-called *chromospheric evaporation* - a process in which hot and ionized chromospheric plasma fills the coronal magnetic loop that is based at the flaring footpoints. Since this process is triggered by particle beams being stopped in the denser layers, both HXR and SXR emissions are tied during the impulsive phase according to the Neupert effect (a derivative of HXR light curve approximately matches SXR light curve, Neupert 1968).

The total bremsstrahlung power radiated from a thermal plasma per unit volume, unit

frequency, and unit solid angle is defined as

$$\epsilon = n_\nu \frac{n_e}{4\pi} \int P_i(\mathrm{v}, \nu) f(v) \mathrm{dv}, \tag{1.10}$$

where $P_i(\mathrm{v}, \nu) = n_i \mathrm{v} Q_r(\mathrm{v}, \nu)$ is total bremsstrahlung power of a single electron colliding with n_i ions, $Q_r(\nu, \nu)$ is the radiation cross-section, v and n_e are the electron velocity and density, respectively, and n_ν is the refractive index on the medium (Aschwanden 2005).

When assuming a Maxwell-Boltzmann velocity distribution of the plasma with temperature T

$$f(\mathrm{v})\mathrm{dv} = \left(\frac{2}{\pi}\right)^{1/2} \left(\frac{m}{m_B T}\right)^{3/2} \mathrm{v}^2 \exp\left(-\frac{m\mathrm{v}^2}{2k_B T}\right) \mathrm{dv} \tag{1.11}$$

and inserting it into Equation 1.10, the total bremsstrahlung power can after the integration be written as

$$\epsilon_\nu \mathrm{dv} \approx 5.4 \times 10^{-39} Z^2 n_\nu \frac{n_i n_e}{T^{1/2}} g(\nu, T) \exp\left(-\frac{h\nu}{k_B T}\right) \mathrm{dv}, \tag{1.12}$$

where Z is the ion charge number, $g(\nu, T) = \frac{\sqrt{3}}{\pi} \ln \Lambda = \frac{\sqrt{3}}{\pi} \ln\left(\frac{b_{max}}{b_{min}}\right)$ is the Gaunt factor and b_{max} and b_{min} are maximal and minimal impact parameters. The classical bremsstrahlung treatment was used ($h\nu = \frac{1}{2} m \mathrm{v}^2$).

The observable flux at Earth can be derived from the total bremsstrahlung power as

$$\mathrm{d}F = \frac{\mathrm{d}\epsilon}{\mathrm{d}t\, \mathrm{d}A\, \mathrm{d}(h\nu)} = \frac{\mathrm{d}V}{R^2 h} \epsilon_\nu, \tag{1.13}$$

where R is the Earth - Sun distance.

After the integration over the source, the flux becomes

$$F \mathrm{d}\nu = \int \mathrm{d}V \frac{1}{R^2 h} \epsilon_\nu \mathrm{d}\nu, \tag{1.14}$$

that after simplification (coronal electron density = ion density, neglecting Gaunt factor

and ion charge number, that are both approximately equal to unity) becomes

$$F(\epsilon) = 8.1 \times 10^{-39} \int_V \frac{\exp(-\epsilon/k_B T)}{T^{1/2}} n^2 \mathrm{d}V \tag{1.15}$$

Note: The emission measure together with plasma temperature, is one of the parameters of the iso-thermal component used in SSW/OSPEX (Freeland & Handy 1998; Schwartz et al. 2002):

$$EM = \int n_e^2 dV \tag{1.16}$$

The following effects affect the resulting electron distribution and some can cause spectrum flattening at lower energies. They can influence the estimate of the E_C and must be taken into consideration during the fitting process.

- Pileup effect (Smith et al. 2002)

  In the case of RHESSI instrument the pileup effect (described in Section 2.5.1) has to be considered.

- Photospheric albedo (Compton backscattering)

  The X-ray source located in the chromosphere illuminates the photosphere that has a non-zero reflectivity. The reflected X-ray flux is then detected by the detector and constitutes an additional component in the spectral fit.

- Anisotropy of the electron beam (Gluckstern & Hull 1953; Massone et al. 2004)

  The electron-ion bremsstrahlung cross-section is a function of the photon energy, the electron energy and the angle between the pre-collision electron velocity vector and the direction of photon emission. As a result, the hard X-ray emission from a prescribed electron source vary with viewing direction.

- Non-uniform target ionization

  The decrease of ionization with depth in the solar atmosphere reduces long-range collisional energy losses, which enhances the HXR bremsstrahlung efficiency there. This effect may elevate the HXR spectrum at higher energies by up to a

factor of 2.8 yielding to a flattening of the HXR spectrum in between low and high energies.

- Return current (Knight & Sturrock 1977; Emslie 1980; Holman 2012)
  The self-induced electric field due to a rapid move of the charge, cause a break force that removes energy from the beam. The electric field triggers a current composing of ambient and scattered electrons, that has the opposite polarity with respect to the flare beam.

- Evolution of the electron distribution during the measurements

Figure 1.7 shows a high energy component consisting of various nuclear de-excitation lines in the energy range $\sim 1-8$ MeV that is produced through interactions of ions with the ambient plasma. The most prominent ones are at 6.129 MeV from ^{16}O, 4.438 MeV from ^{12}C, 1.779 MeV from ^{28}Si, 1.634 MeV from ^{20}Ne, 1.369 MeV from ^{24}Mg and 0.847 MeV from ^{56}Fe. We also observe the positron annihilation line at 511 keV and deuterium formation (neutron captured by hydrogen) line at 2.223 MeV. Many weaker lines merge and form a quasi continuum (Vilmer et al. 2011). These lines provide an analytical tool for proton investigations in flares.

Lines produced by the interaction of protons or α-particles with ambient ions heavier than He produce narrow lines but interaction with hydrogen or helium produces broad lines (Murphy et al. 2007). As an ion can be excited by a particle with a kinetic energy in a certain range, a cross-section becomes the principal parameter that sets constraints on the flare beam parameters. However, other beam parameters like a spectral index or α/proton ratio significantly affect the range of effective energies for the production of a given line. For the thick-target model particles can contribute to a given line production even if they have greater energy than the one for which the cross-section is significant as particles can lose energy within the target before interaction.

A couple of lines can be used to estimate the spectral index of the proton beam when comparing the lines ratio with a model (an example of 6.129 MeV and 1.634 MeV lines

is in Figure 1.8).

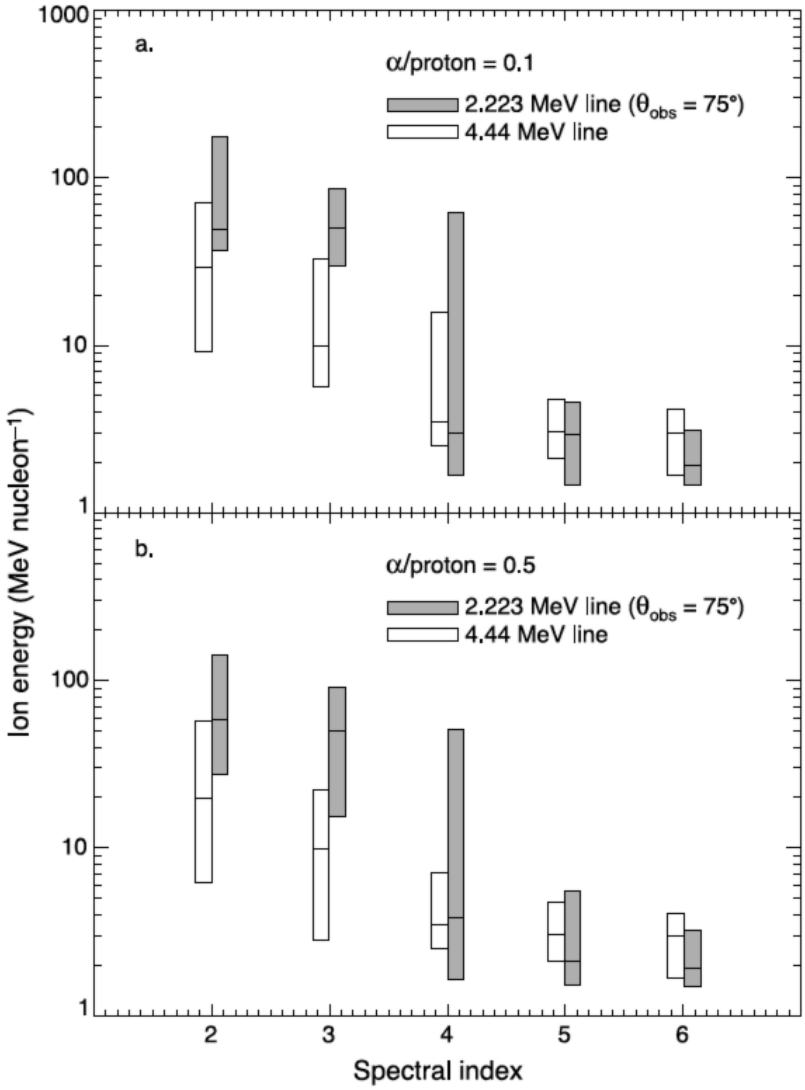

Figure 1.8: Effective ion energies for the 2.223 MeV neutron capture line and 4.44 MeV ^{12}C line production with respect to spectral index. The effective ion energy range is defined as a range where the yield fell to 50% of each side of the maximum. The horizontal line within each box marks the peak of the distribution. Reproduced from Murphy et al. (2007).

1.4.1 The role of protons in flares

The possibility that the HXR emission in solar flares is produced by accelerated protons was investigated by Emslie & Brown (1985). They found that in the case of protons ($\geq$ 20 MeV), the beam flux may be up to three times lower compared to electrons ($\geq$ 10

keV) in order to produce a similar HXR burst. Although there are less strict energetic constraints in the proton beam scenario, they concluded that a greater penetration depth of protons may not be compatible with the occultation of the HXR burst observed close to the limb.

Hurford et al. (2003) published the first γ-ray images of an X-class flare using the RHESSI instrument. They found a 2.223 MeV source displaced by 20"±6" from the weighted average of the 0.3-0.5 MeV and 0.7-1.4 MeV sources (Figure 1.9). It was also shown, that the emission at the 2.223 MeV line peaked about $\sim$ 2 minutes later than all the other broadband channels.

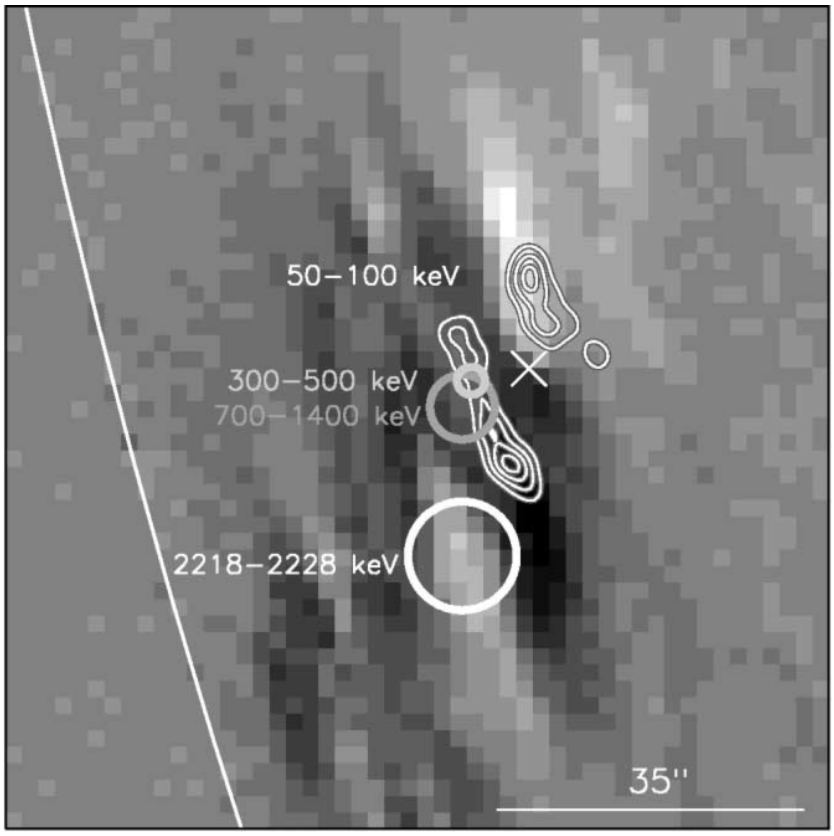

Figure 1.9: Locations of HXR and γ-ray sources in a X4.8 flare close to the limb. The background SOHO/MDI magnetogram was obtained 15 minutes before the flare. Reproduced from Hurford et al. (2003).

Miller & Roberts (1995) presented a model where protons are accelerated by Alfvén waves and found that turbulence can accelerate protons and the process can be more efficient if the length of the loop is large. Based on both the models and observations

mentioned above, Emslie et al. (2004) concluded that long acceleration sites are dominated by non-thermal protons, while we detect mostly electron bremsstrahlung from sites where short loops dominate. They claimed that where proton acceleration dominates, the following criterion

$$L_9 \gtrsim \frac{B_2^2}{15 Q_2^{2/3} n_{10}^{1/2}}, \tag{1.17}$$

where L_9, B_2, Q_2 and n_{10} denote to acceleration length in units of 10^9 cm, magnetic field in units of B/10^2 G, energy density injection rate of the turbulence in units of Q/10^2 ergs cm^{-3} s^{-1} and density in units of n/10^{10} cm^{-3}, respectively, is valid.

When considering accelerated protons, one has to bear in mind that before the particles deposit their energy into the deeper layers of the atmosphere, they can get trapped in a process of magnetic mirroring, as suggested by Struminsky & Gan (2015). Magnetic mirroring is based on the principle of conservation of the magnetic moment (Aschwanden 2005):

$$\mu = \frac{\frac{1}{2} m v_\perp^2(s)}{B(s)} = const., \tag{1.18}$$

where s is a coordinate along the loop.

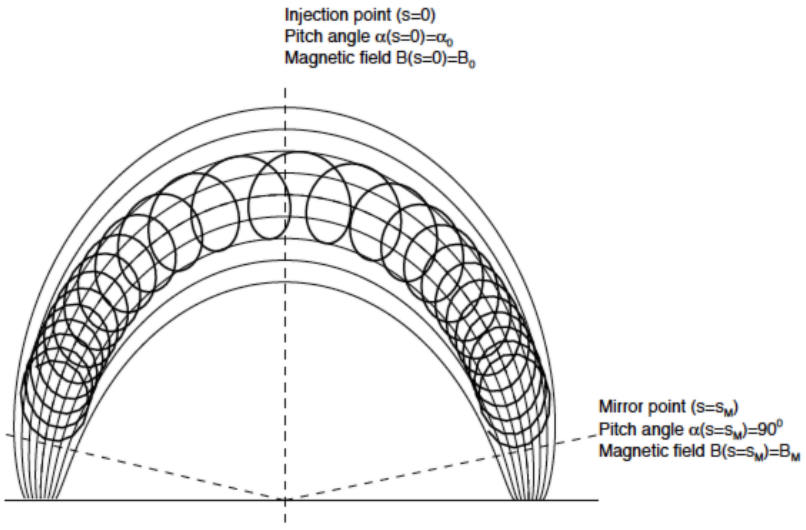

Figure 1.10: A schematic diagram of a magnetic loop with a charged particle moving parallel to the magnetic field and showing Larmor rotation. Reproduced from Aschwanden (2005).

Figure 1.10 shows that once the particle enters an area with stronger magnetic field (in the solar atmosphere this would be the chromosphere), it can get reflected. This is due to energy conservation (the sum of parallel and perpendicular components of kinetic energy remains constant) and Equation 1.18 tells us that in stronger fields the perpendicular component of kinetic energy has to be greater. If the field is sufficiently strong, the parallel component will drop to zero and the particle will bounce back.

Assuming a magnetic field B_M where the particle's parallel velocity equals to zero, Equation 1.18 defines the so-called *loss cone*:

$$\frac{B_0}{B_M} = \frac{v_{0\perp}^2}{v_{M\perp}^2} = \frac{v_{M\perp}^2}{v_M^2} = \sin^2 \alpha, \tag{1.19}$$

where α is an angle between the parallel and perpendicular components of v_0.
Particles inside the loss cone can go through, meanwhile particles outside the cone get reflected. The cone opening angle does not depend on the mass of the particles, but electrons originally outside the cone can be scattered due to Coulomb collisions and other mechanisms inside the cone much faster than protons.

The delay of γ-ray emission with respect to X-rays was analysed by Bespalov et al. (1988), who used a model of magnetic trap with a turbulent propagation under an assumption of a simultaneous acceleration of both electrons and protons. They concluded that flares that are powerful enough, can excite electromagnetic turbulence due to various instabilities (for example an anisotropy in a distribution function of particles). In the solar corona electrons can excite Langmuir waves or whistlers and protons can excite Alfvén waves that cause pitch angle diffusion. In their model the lifetime of electrons in the flare loops depends on their energies, since electrons with higher energies need more time to reach magnetic foot-points, but the lifetime of protons does not depend on their energies. If the acceleration process in the corona is powerful enough, a large level of disturbance from Alvén waves causes a significant scattering in pitch-angles for protons but this is less effective for electrons. However, the process also depends on the trap parameters and in some cases the pitch-angle scattering is not observed and

both electrons and protons may reach the loop foot-points simultaneously.

Magnetic mirroring can also explain the observations of Ackermann et al. (2017), who in some flares reported up to ~15 hours long fadeout of the γ-ray emission.

1.5 Outline

The main aim of this thesis is to address these essential questions:

1. What is the difference in the nature of type I and type II WLFs?
2. What type of particle beams can trigger WL emission while leaving the upper chromosphere undisturbed?
3. Where does the WL excess emission originate?
4. What is the emission mechanism of type II WLFs?

Chapter 2 provides a review of instrumentation currently used in solar flare research and highlights the limits imposed by instrumentation due to the specific nature of flares. The observational part (Chapter 3) presents unique spectra of WLFs together with a more common analysis of particle beams and supportive satellite data. The observations give us constraints on the particle beam parameters. Chapter 4 theoretically describes the radiative transfer in the solar atmosphere and the 1D radiative hydrodynamic code used in this work. Chapter 5 presents the model parameters, explores the effect of recent additions to the code used, and attempts to reproduce the spectral features detected in the studied event. The energy constraints are introduced into the models and the parameter space for particle beams is narrowed down and discussed in Chapter 6. The impact of the results onto the current knowledge of type II WLFs is discussed in Chapter 7.

Chapter 2

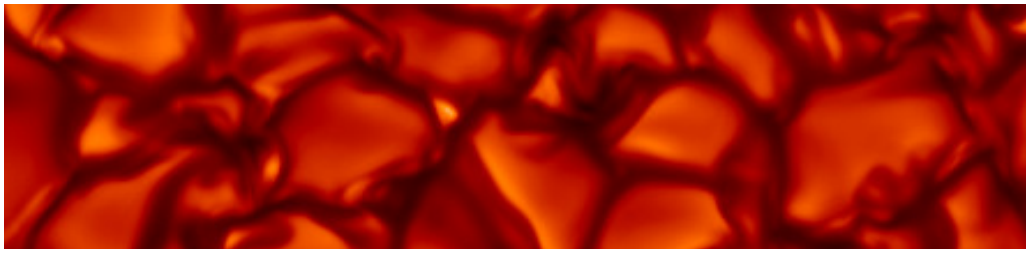

Instrumentation

“My life has no purpose, no direction, no aim,

no meaning, and yet I’m happy.

I can’t figure it out.

What am I doing wrong?”

- Charles M. Schulz

High resolution observations and the use of statistical samples have shown that WLFs are a lot more common than we originally thought (Matthews et al. 2003; Hudson et al. 2006). Spectroscopic observations of WLFs are scarce (Hudson et al. 2010). This is mainly due to their short duration and the lack of suitable instrumentation that would capture the flare kernel spectra with sufficient wavelength coverage, temporal, and spectral resolution. Therefore, a new observational approach was used to obtain spectra with broad wavelength coverage including the Balmer jump. The observational strategy requires a selection of an active region that has a high probability for producing a large flare, and a systematic observation of the region with a high-cadence instrument covering a broad range of wavelengths. The observation of a spatially limited part of the solar atmosphere helps to significantly suppress the background radiation.

2.1 Current ground-based instrumentation and solar flares

In the visible wavelength range the contrast of a flare is typically very low due to the strong solar background radiation. Therefore, in the visible range the solar flares cannot be successfully observed if the flux is integrated over the whole disc. Some spatial selection is therefore needed. The *Multi-channel Flare Spectrograph* (MFS, Kotrč 2009) was constructed for simultaneous observations in Hα, Hβ, He I D3, Ca II K&H and Ca II IR lines using a diffraction grating and 12-bit CCD cameras for each channel with spectral resolution in the range of 0.0016 - 0.0026 nm. However, traditional slit spectrographs have a very low chance that the slit would be placed on the moving, short lasting flare kernel. It is very difficult to predict where a flare will occur and even if such a spectrograph is working in scanning mode, it is unlikely that more than a few flare spectra will be captured during the whole event.

Most spectroscopic instruments (both spectrographs and imagers) working in the visible/near-UV/near-IR were designed for an investigation of a single or multiple spectral line(s) to study one or several layers of the solar atmosphere in detail. The *Interferometric BIdimensional Spectrometer* (IBIS, Cavallini 2006) is composed of a series of

two Fabry-Perot interferometers and a set of narrow-band interference filters designed to take monochromatic images of the solar surface with high spectral, spatial and temporal resolution. The *Rapid Oscillations in the Solar Atmosphere* (ROSA, Jess et al. 2010) is a high cadence six camera imager working with the maximum full-frame rate of 30 Hz. Its working waveband comprises of narrow channels Ca II K and Hα line cores, magnetogram centred at 630.25 nm and tuneable universal birefringent filter, 0.9 nm wide G-band, and 5.2 and 10.2 nm broad channels centred in blue/near-UV continuum. The imagers are suitable to observations of the flare morphology, and if the spatial and temporal resolutions are high enough, they can contribute to flare kernels localisation, which is especially useful if the flare is located close to the solar limb (Martínez Oliveros et al. 2012). However, their wavelength coverage is limited to several data points, so a reliable determination of the flare mechanism is not possible.

The advantages of both above described designs were combined in the *Multi-Channel Subtractive Double Pass* (MSDP, Mein 1977, Faurobert et al. 2012) spectrograph that uses an entrance window instead of the usual long slit. It images a selected region in several wavelengths, so the full line profile can be later calculated for every pixel in the image. This instrument usually has a higher success rate in flare observations (Radziszewski et al. 2007, 2011). However, the observed wavelengths typically cover only one selected spectral line, therefore it cannot provide information about the flux across a broad wavelength range.

2.2 White-light observations

The Solar Dynamics Observatory (SDO, Pesnell et al. 2012) has implemented state-of-art technology and is probably the most complete set of instruments for solar irradiance measurements and imaging.

The *Helioseismic and Magnetic Imager* (HMI, Scherrer et al. 2012; Schou et al. 2012) is an instrument on board SDO commonly used to monitor the evolution of active re-

gions and look for WLF signatures. It provides full-disk observations in Fe I line 617.3 nm with a cadence of 45 s and 90 s, respectively, and an angular resolution of 0.50 ± 0.01 arc-sec per pixel.

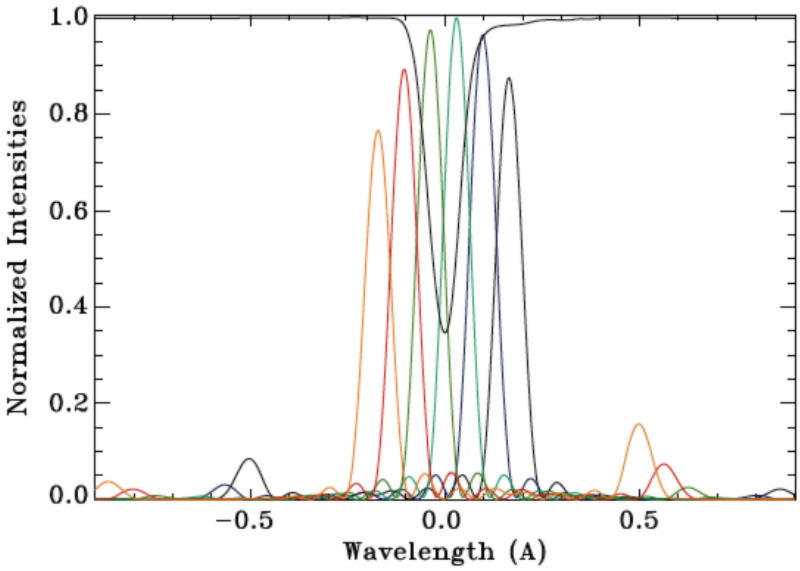

Figure 2.1: The spectral profile of Fe I 617.3 nm line (black) together with six tuning position profiles of the filer (colour) spanning the range ±0.01725 nm from the line center. FWHM = 0.0076 nm, spacing 0.0069 nm. Reproduced from Schou et al. (2012).

The instrument consists of a refracting telescope (diameter 140 mm), a polarization selector, an image stabilization system, a narrow band tunable filter and two front-illuminated 4096×4096 pixels CCD cameras (total focal length 4953 mm). The Lyot filter composes of 5 elements and is tuned by a rotating half-wave plate. The full width at half maximum (FWHM) is 0.0612 nm. The Lyot filter is followed by wide-band and narrow-band Michelson interferometers with vacuum and glass legs, split with a polarising beamsplitter.

The front sensor is dedicated to measurements of left and right circular polarisation (LCP, RCP) that allow the instrument to obtain Doppler maps and line-of-site magnetic field, and the side sensor is dedicated to measurements of the full Stokes vectors (I, Q, U, V; McMaster 1954) that allows us to obtain the full vector of the magnetic field (cadence 90 s). During its first 45 s the instrument records filtergrams at 6 different

spectral positions across the Fe I line profile (Figure 2.1) - two filtergrams per each sensor and wavelength. The front sensor keeps switching between LCP and RCP, while the side sensor switches between I and Q Stokes parameters. These measurements allow the line-of-sight magnetic field to be inferred. During the next 45 seconds the side CCD records the remaining Stokes parameters (U and V) to provide the missing information needed for a calculation of the full magnetic vector, while the front sensor starts its new sequence.

The continuum is reconstructed from the Stokes I far blue and red wings of the line. However, Švanda et al. (2018) showed that although the technique is suitable to reconstruct the continuum on the quiet Sun, during flares it may fail due an inadequate sampling of the magnetically broadened Fe I line.

2.3 Spectroscopic instrument in the visible wavelength range

The main challenges while observing flares have to do with their unpredictability, short duration, low contrast in white-light and small spatial characteristics. The conventional slit-based spectrographs are not suitable because they are not able to record the whole duration of the events as the footpoints (or the slit itself when in a scanning mode) move. On the other hand full-disc observations cannot be used for flares analysis in white-light due to their low contrast. Kotrč, Procházka, & Heinzel (2016) developed a spectrograph designed for WL flare observations. The instrument described here has been able to address most of the difficulties.

The *Image Selector* (IS, Figure 2.2) consists of a glass wedge, a set of circular apertures of sizes spanning from 4 to 18 mm and a focusing lens. Together with a spectrometer and an Hα context imaging system it records spatially unresolved spectra with high temporal resolution (technically with integration time $\geq$ 3.8 s) and images of the chromosphere in the vicinity of the observed region.

The glass wedge serves to reflect light into the context imager and is made to sup-

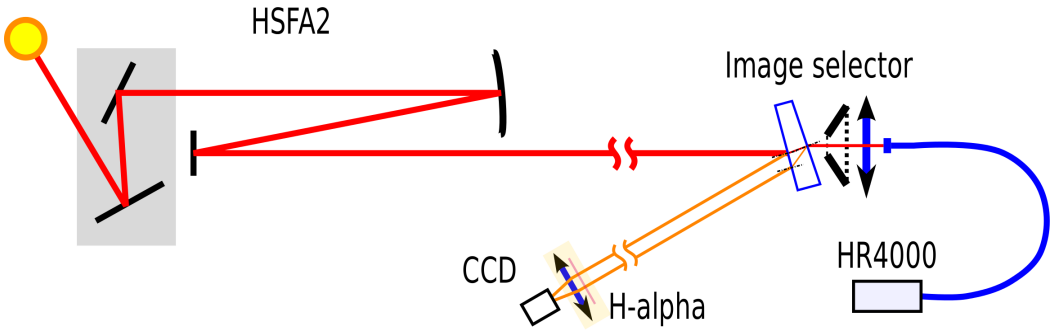

Figure 2.2: A schematic diagram of the Image Selector. The light reflects from mirrors of a coelostat first and then is focused by a parabolic mirror to create a sharp image in a distance where IS is placed (red). Light that goes through the delimiting diaphragm is focused into an optical fibre that feeds up the spectrometer (blue). A small fraction of light is reflected from the glass wedge into the context imager (orange). Reproduced from Kotrč et al. (2016).

press the interference at the wavelength of the Hα line. It has a coating that reflects wavelengths longer than $\sim$ 400 nm, which helps to 'flatten' the spectrum and allows shorter exposure times at the context imager. The diaphragms are black-painted in order to avoid unwanted reflections with an exception of a $\sim$ 1 mm rim around the hole that is polished and reflects light. Thanks to that the position of the measured area is marked with a bright circle overlying the image of the chromosphere and can be recorded by the context imager. Taking data only from the active region helps to increase the contrast of the flare significantly. The inclination of each of the apertures can be set using two screws accessible from the top of the instrument. This helps to adjust the intensity of the apertures' reflections visible on the context images. The apertures sit in a filter wheel commonly used as a part of deep-sky CCD cameras by Moravian Instruments Inc. The filter wheel can be controlled from a computer.

A socket for the glass wedge allows it to rotate and incline once the locking screws are loose (visible on the front side of the instrument - Figure 2.3). The adjustment is needed to reflect the image of chromosphere into the context imager. Photographs of the IS are given in Figure 2.3.

The HR4000 by Ocean Optics, Inc. is a very compact Czerny-Turner type spec-

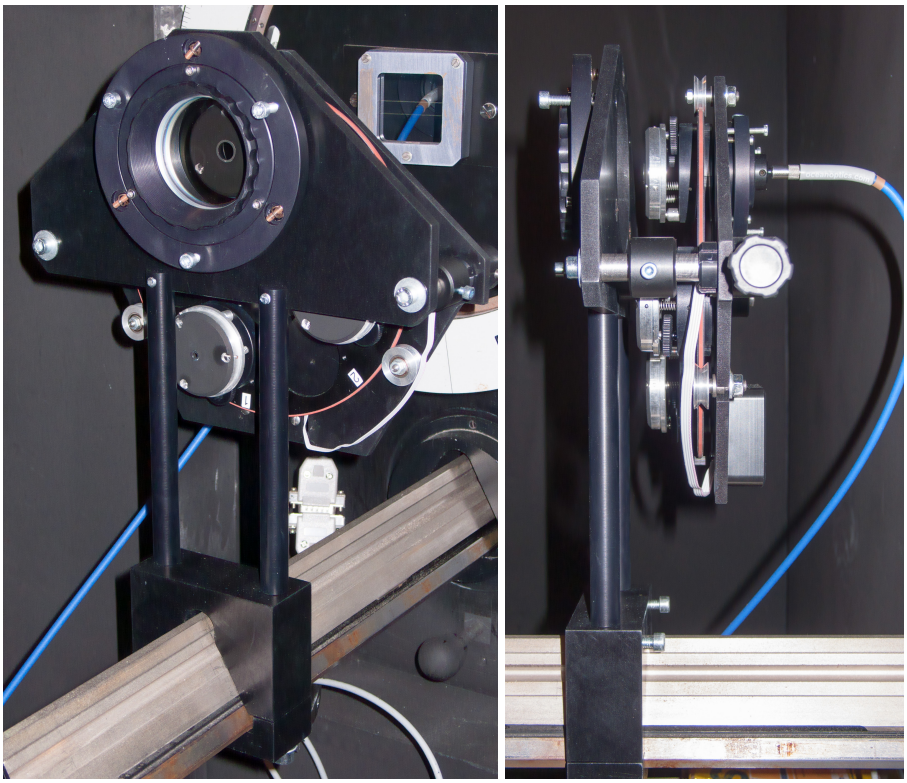

Figure 2.3: Front (left) and side (right) photographs of the IS.

trograph (Czerny & Turner 1930) equipped with an 1D 14-bit CCD. It has a working range of wavelengths 350 - 485 nm, but due to the very large gradient of the spectrum in this range, scientifically valuable data were taken in a range 350 to 440 or 420 nm only in order to get sufficiently high signal-to-noise ratio at shorter wavelengths. The longer wavelengths were then overexposed. The device has very low noise characteristics - the mean value of 50 dark frames with exposure time 30 ms is 668.18 ± 0.16 counts, with a standard deviation 9.89 ± 0.13 counts over the whole wavelength range. The low integration time allows us to study a spectrally resolved flare evolution on a smaller time scale than with any other spectrograph. A downside of the instrument is its limited spectral resolution (on average 33.8 pix per nm) but it is sufficient for the study of continua.

IS was first developed and tested in conjunction with the pre-focal part of the *Multichannel Flare Spectrograph* (MFS, Valníček et al. 1959) in the Astronomical Institute in Ondřejov. This part of MFS consists of a coelostat with mirrors of 360 and 280 mm

in diameter, spherical objective (230 mm in diameter and focal length of 1350 mm) and a secondary flat mirror. The setting provides an image of the Sun at a focal plane with a diameter of 125.6 mm. Due to the advanced age of the instrument and the lack of a pointing system, it was not possible to use it for scientific data acquisition.

IS was then mounted on the Horizontal Sonnen Forschungs Anlage 2 (HSFA2, Figure 2.4, Kotrč 2009) that is a Jensch-type coelostat (Jensch 1959). This type of coelostat has both mirrors in fixed distance that do not vary during the year, and the whole device rotates around the polar axis during the day. However, when the Sun is low in the horizon, the mirrors are configured horizontally, which is prone to seeing disturbance and may require more frequent calibrations. HSFA was designed by the company Carl Zeiss Jena and two such telescopes were manufactured for the Astronomical Institute in Ondřejov in 1980s. The original purpose of HSFA was spectroscopy with high spectral resolution. It was used in both the visible and near-infrared range (Heinzel et al. 1986). HSFA2 was rebuilt in 2009 to be used in a conjunction with a multichannel spectrograph and equipped with an electronic control system. The focal length is 34.85 m and the diameter of the primary mirror is 50 cm. This setup gives an image of the Sun in the focal plane with a diameter of 32.5 cm. The above mentioned physical aperture sizes correspond to a field-of-view of 23 to 103 arcsec. Using this telescope we can acquire spectra from a selected active region only, so a presumed flare would be measured with much higher contrast than in a case of the MFS.

As the context imager Coronado P.S.T. (Personal Solar Telescope) was used together with the fast Celestron Skyris 247M camera (1.25" nosepiece). Coronado P.S.T. is a portable telescope with a diameter of 40 mm and focal length of 400 mm. It has an inbuilt Hα filter with a bandwidth < 1Å. The 12 bit Celestron Skyris camera has monochrome Sony ICX274AL sensor with resolution 1600×1200 pixels and records at a rate up to 20 frames per second (FPS). The sensor's dimensions are 8.50 mm $\times$ 6.80 mm with 4.40 μm pixels.

Figure 2.4: HSFA2 telescope with covered mirrors. Light first hits the lower mirror that is fitted with a joint to allow declination adjustments. The upper mirror is sitting on a polar axis. Reproduced from Procházka (2014).

Procházka (2014) introduced a novel sensitive method to detect an increase of continua that exploits the benefits of the IS's high-cadence. Since the measurements suffer from strong seeing effects, and the level of measured continua also vary with the changing solar altitude, it is not possible to reliably calibrate the data. Instead he introduced a batch processing when comparing levels of two or multiple selected spectral bands with each other. He was especially interested in the changes of the Balmer continuum (its channel was defined as waveband range 351.10 – 363.03 nm) with respect to a small spectral window at 391 nm. This method can be very effective in distinguishing between variations of the overall continuum level and a relative change in the intensity we see in different parts of the spectrum that is expected in flares. Such signatures would be associated with changes of the levels of particular types of continua that are described in Section 1.3.1.

Figure 2.5 shows two examples of the technique described above applied on two datasets. Each data point in the figures represents a single spectral measurement. When the Sun is quiet, the data points lie roughly in line at the bottom of charts. Changes of the total flux move the measurement along that line. However, during a flare a brightening in Balmer continuum can occur, which translates into a shift along the Y axis in the plots. During the decay phase the ratio between both investigated spectral channels lower back to the pre-flare level. If the time of measurement of the whole batch is sufficiently long, the pre-flare and post-flare states create a significantly high concentration of data points at the bottom of the charts. It was shown that this method is able to detect an average increase along the Balmer continuum channel of $\sim 2\%$, which would not be detectable when evaluating the spectra on a one-to-one basis.

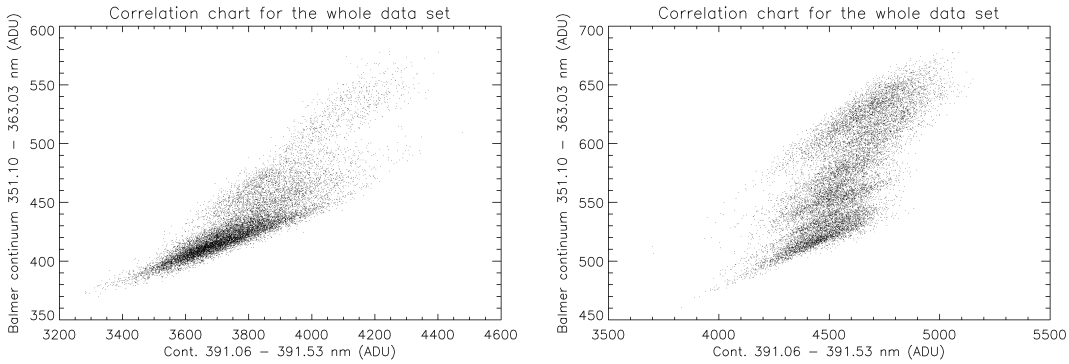

Figure 2.5: Correlation between Balmer continuum and Continuum 391 nm channels for two flares (X2.2 and X1.5 on 10 June 2014). Reproduced from Procházka (2014).

2.4 Ultra-violet wavelength range

2.4.1 SDO Extreme Ultraviolet Variability Experiment (EVE)

The *EUV Variability Experiment* (EVE, Woods et al. 2012; Hock et al. 2012) is an instrument on board SDO that consists of several detectors that measure the full disc signal in the UV range. Below the main characteristics of EVE instruments are described.

- *EUV SpectroPhotometer* (ESP)
  - A broadband spectrograph with a transmission grating (2500 lines per mm) that measures irradiance in the wavelength range 0.1 to 39 nm to provide calibration data
  - The slit is equipped with 150 nm aluminium foil filter to limit out-of-band light
  - Silicon photodiodes in the plus and minus first order are centered at 18.2, 25.7, 30.4 and 36.6 nm, a photodiode in the zeroth order is equipped with thin foil Ti (300 nm) / C (40 nm) filter to isolate waveband 0.1 to 7 nm
  - Cadence = 0.25 s
- *Solar Aspect Monitor* (SAM)
  - Pinhole camera to provide a pointing reference for EVE
- *Multiple EUV Grating Spectrographs* (MEGS)
  - Records spectra with a cadence 10 s and spectral resolution 0.1 nm
  - Uses 2048×1024 CCD designed by Westhoff et al. 2007 that is shielded by ~ 25 mm aluminium, gain ≈ 2 electrons per data number (DN)
  - MEGS-A
    - Off-Rowland-circle 80° grazing-incidence spectrograph designed by Crotser et al. (2007)
    - Working range 6 to 37 nm
    - Has two slits (20 μm wide and 2 mm high) and two separate primary filters to isolate different wavebands
    - A1 slit: λ = 6 to 18 nm
    - A2 slit: λ = 16 to 37 nm
    - Suffered a failure in the CCD electronics and does not provide data since 26th May 2014

  - MEGS-B
    * Two-grating, cross-dispersing spectrograph
    * Working range 36 to 106 nm
    * Due to an unexpected degradation it is exposed only 3 hours per day. The observations are triggered when ESP detects a flux equal or greater to an M-class flare in the 0.1 - 0.7 nm channel.

- *MEGS-Photometer* (MEGS-P)
  - A silicon photodiode placed in the minus first order of the MEGS-B grating
  - Equipped with an interference filter to measure irradiance in the Lyman α line (121.6 nm, bandwidth 10 nm)
  - A masked identical counterpart is used to provide calibration dark signal

Milligan & Chamberlin (2016) described an anomaly in the measurements of Lyman α by MEGS-P. During flares it showed a rise time of tens of minutes peaking around the peak of soft X-ray emission instead of the expected rapid rise and temporal behaviour similar to hard X-rays. It is believed that this is due to a contribution of some higher temperature line or continua in the measured waveband.

The data with the highest scientific potential are the Level 1 for ESP, MEGS-P and SAM and level 2 for MEGS 1 and 2. Level 1 MEGS-P and ESP are distributed in 24-hour packages, while larger MEGS-A and -B and SAM data are packed in one-hour duration files. The level 2 output contains a pair of files: merged (MEGS-A and -B) spectra with spectral resolution 0.02 nm and temporal profiles of lines and bands, both with a timespan of one hour. These lines and bands include many plasma temperatures between 20 000 K and 10 MK and partially overlap with the broadband imaging obtained by some of the *Atmospheric Imaging Assembly* (SDO/AIA) filters or *EUV Sensor* (GOES/EUVS).

2.4.2 GOES/Extreme Ultraviolet Sensor

The *Geostationary Orbiting Environmental Satellites* (GOES) are operated by the US *National Oceanic and Atmospheric Administration* (NOAA) and serve to monitor weather on the Earth and so-called *space weather* in its surroundings. The latter purpose comprises measurements of the solar wind, magnetic field and ultra-violet radiation from the Sun. The satellites orbit the Earth on a geostationary trajectory to maintain a fixed position close to the equator.

The *Extreme Ultraviolet Sensor* (EUVS, Viereck et al. 2007; Evans et al. 2010) on board GOES-13 (launched on 24 May 2006) is a spectrograph with three transmission gratings. Detectors A and B share a grating as do detectors C and D (Figure 3.18). The last detector E has a separate grating. The bandpass of channel E varies among the satellites (Table 2.1). The data are available to the public within seconds from acquisition.

Satellite	Bandpass of channel E
GOES-13	113.5 – 132.8 nm
GOES-14	113.7 – 135.9 nm
GOES-15	116.3 – 132.4 nm

Table 2.1: Bandpass of EUVS's channel E on board of GOES13-15.

One of the advantages of EUVS over EVE is that it is well calibrated with a 100% duty cycle and does not suffer from the anomaly described earlier. The E channel is processed since mid-2014 and scaled on a daily basis according to *Solar Radiation & Climate Experiment: Solar-Stellar Irradiance Comparison Experiment* (SORCE SOLSTICE, McClintock et al. 2005) Lyman α values due to a noticeable degradation.

2.5 X-ray observatories

X-ray observations provide the basic diagnostics of particle beams in flares. In recent years the most common instrument for the study of X-rays has been the *Reuven Ramaty*

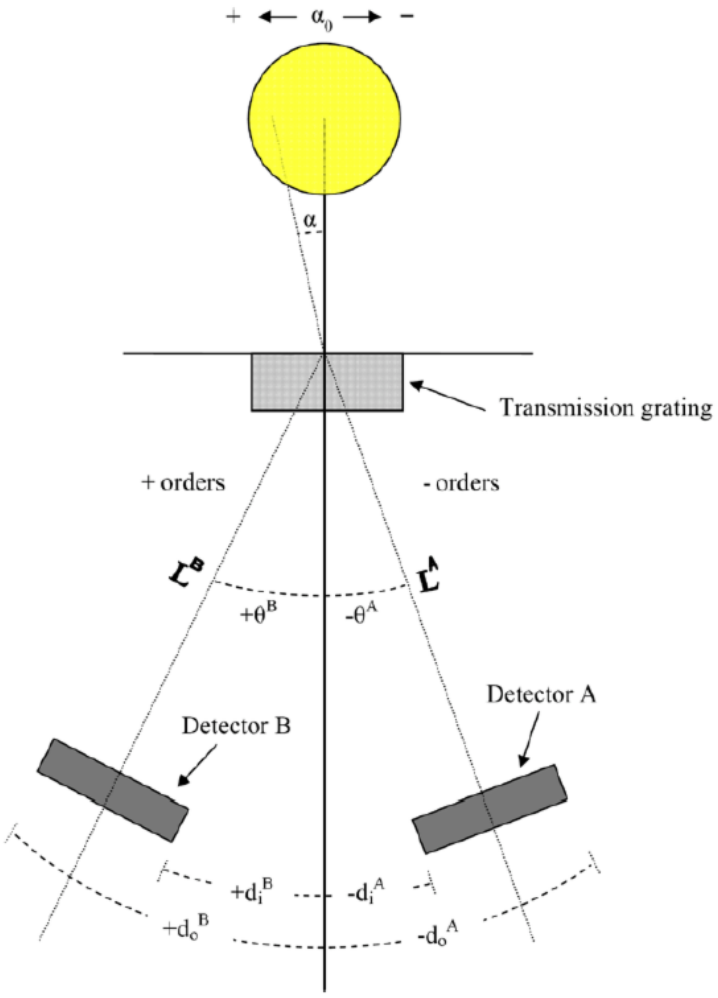

Figure 2.6: A schematic diagram of a part of EUVS. Detectors A and B are set on the opposite sides of the grating's optical axis. The same configuration is used for detectors C and D. Reproduced from Evans et al. 2010.

High-Energy Solar Spectroscopic Imager (RHESSI, Lin et al. 2002). A more modern *Gamma-ray Burst Monitor* (GBM) on board of *Fermi Gamma-ray Space Telescope* (Fermi, Meegan et al. 2009) was designed to work together with the *Large Area Telescope* (LAT), extend its energy range and locate sources of γ-ray bursts in deep space. However, it can be also used for solar flare observations and provide high energy range spectra. Although these instruments use different methods and technology, both can provide vital data that allow us to study critical features of solar flares. Table 2.2 shows some basic information for both instruments.

Parameter	RHESSI	Fermi/GBM
Launched	2002	2008
Orbit	600 km, inclination 38 deg	565 km, inclination 25.6 deg
Detector material	Germanium	Sodium-iodide (NaI) and Bismuth-germinate (BGO)
Energy range	3 keV to 17 MeV	NaI: 8 keV 1 MeV BGO: 200 keV to 40 MeV
Spectral resolution (FWHM)	1 – 5 keV	~ 10%
Maximal angular resolution	2.3 arc sec	None
Temporal resolution	2 s	1.024 s

Table 2.2: Comparison of RHESSI and Fermi observatories. The Fermi/GBM's temporal resolution is for CSPEC data type that provide high spectral resolution of 128 pseudo-logarithmically scaled energy channels (Yu et al. 2016).

2.5.1 The Reuven Ramaty High-Energy Solar Spectroscopic Imager

Despite its originally proposed 2 year lifetime, the Reuven Ramaty High-Energy Solar Spectroscopic Imager (RHESSI) still provides X-ray images and spectra of the Sun. Because X-rays cannot be focussed using mirrors, it uses Fourier-transform imaging (Makishima et al. 1977). This method is based on producing a modulated waveform due to the smooth rotation of the spacecraft (period ~ 4 s). The instrument has a cylindrical shape with a set of nine Rotating Modulation Collimators (RMCs, Figure 2.7) and segmented detectors. RMCs consist of pairs of the same grids. The grids are set on a tray attached to a graphite-epoxy tube and must be oriented parallel with a tolerance of 1 arc min. This material is expected to resist twists and other deformations, which prevents the grids from getting misaligned during the mission. Front and rear segments with grids are separated by $L = 1.55$ m. The angular resolution of the imager depends on grid pitch (p), that ranges from 34 μm to 2.75 mm with a step of $\sqrt{3}$, and is defined as

$$\Theta = \frac{p}{2L}. \tag{2.1}$$

Since the instrument rotates, the slats in a grid cause two occultations/de-occultaions of the source per rotation period.

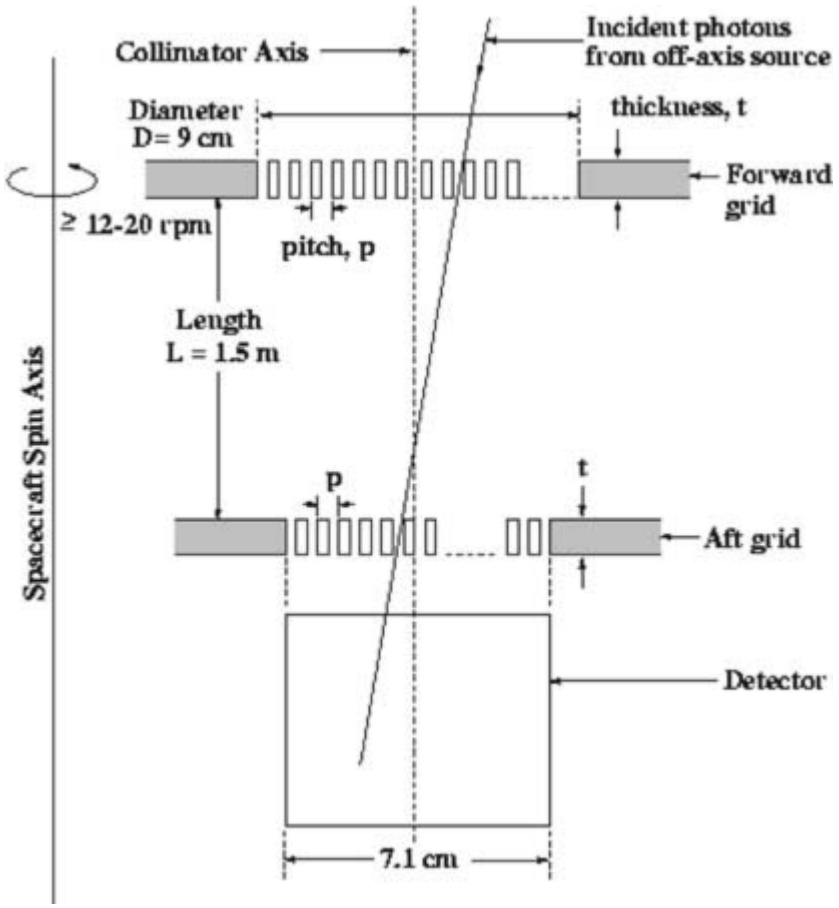

Figure 2.7: A schematic diagram of the Rotating Modulation Collimators. Reproduced from Lin et al. 2002.

The single crystal detectors are cryogenically cooled (< 75 K) to suppress background noise and allow sufficient sensitivity to observe narrow γ-ray lines. The detectors are made of ultra-pure, slightly n-type germanium working under a voltage 2000 – 4000 V, which allows all free charge carriers to be depleted from the crystal (Smith et al. 2002). Damage caused by cosmic rays and trapped protons results a drop in spectral resolution. Once the damage is severe, the spacecraft can anneal the detector for a few days at $\sim 100°$C. The detector is electrically divided into a 1 cm thick front and a 7 cm thick rear segments sensitive from 3 to $\sim$ 200 keV and up to 17 MeV, respectively.

The signals from the preamplifier are taken to a Detector Interface Board in the Instrument Data Processing Unit box. Each board contains both the analog and digital

signal processing circuitry for both segments of one detector. The signal from each event is split, going to a fast-shaping channel, which produces a triangular pulse 800 ns wide at the base. The pulse is used for pileup rejection: two events very close together in time, which would be analyzed as a single higher-energy event by the analog-to-digital converter (ADC), can instead be recognized, and both rejected. If the second event comes shortly after the slow-shaped pulse from the first has already been sampled at its peak and fed to the ADC, then only the second is rejected, since the first was read with its correct energy. The fast lower level discriminator is set at about 7 keV in the front segments (just above the noise) and about 20 keV in the rear segments. Photons below 7 keV in the front segments may pile up with other counts without triggering the pileup veto, so careful data analysis is necessary for high count rates of soft photons (Smith et al. 2002).

The RMCs described here allow the measurements of amplitudes and phases of ∼1100 Fourier components. If the source is sufficiently intense, the finer grids can be used to measure only about ten Fourier components and obtain crude images with a temporal resolution as short as 1.3 ms. Due to a limited dynamic range, the RMC is equipped with two aluminium attenuators (thin and thick) that automatically move in when the detector is saturated. The attenuators reduce the flux of photons with energy up to ∼ 100 keV, but do not affect the higher energetic one.

There are several image reconstruction techniques that can be used for RHESSI data:

- Back projection (Mertz et al. 1986)

  The basic method used by radio astronomers employs 2D Fourier inverse transformation. It is linear, so maps for different time intervals, pitches and harmonics can be summed up.

- Clean (Högbom 1974)

  A clean image is created in an iterative process where back projection is used to

create a so-called *dirty map*. The algorithm then tries to find a set of point sources that would produce the dirty map when convolved with the point spread function (PSF) of the instrument.

- Maximum entropy methods (Sato et al. 1999)

  This method tries to create an image with the most simple sources that still comply to the measured data.

- Forward fitting (Aschwanden 2002)

  Forward fitting tries to make a model of simple structures (circular, elliptical, or curved elliptical Gaussians) represented by as few parameters as possible and then fits the data on that model.

- Pixon (Puetter 1995; Metcalf et al. 1996; Alexander & Metcalf 1997)

  This is another method employing a fitting method. It is designed to avoid any spurious sources and produces the best images for photometry. Pixon is significantly slower than the other named methods and is usually used once there is a need for highly accurate imaging.

2.5.2 Fermi Gamma-ray Space Telescope

The Gamma-Ray Burst Monitor is one of two instruments on board Fermi designed to detect emissions at very short wavelengths, but its capabilities to analyse the signal are more limited compared to RHESSI. It has a lower spectral resolution and does not allow imaging. Unlike RHESSI, GBM was designed as an all-sky detector and does not have any preferred direction of observation. Four triplets of NaI detector units with 12.7 cm in diameter and 1.27 cm thick crystal are set in corners of the spacecraft (Figure 2.8) while each of the detector units of the triplet are oriented in a different location to allow to derive the position of a γ-ray or X-ray source from relative count rates. Each NaI detector unit is equipped with one Photomultiplier Tube (PMT) that transforms the scintillation light into electric signal. The two BGO detector units contain bismuth

germanite crystal of a cylindrical shape with both diameter and height of 12.7 cm and two PMTs on both sides of the crystal. The BGO detector units are placed on opposite sides of the spacecraft (Figure 2.8).

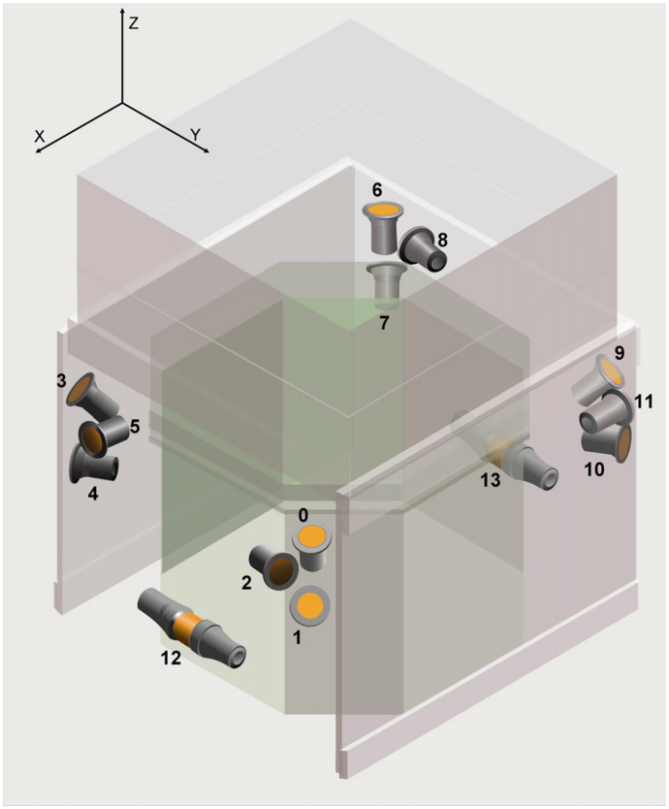

Figure 2.8: Positions of NaI (0 to 11) and BGO (12 and 13) detector units on board of Fermi. Reproduced from Meegan et al. (2009).

The detectors were calibrated at the Max Planck Institute for Extraterrestrial Physics using laboratory radioactive sources from 14 keV to 4.43 MeV and at the Physikalisch-Technische Bundesanstalt at the BESSY synchrotron radiation facility, Berlin, using X-ray radiometry (Bissaldi et al. 2009). The most prominent feature in the spectrum was iodine the K-edge (33.17 keV) that causes a significant dip in the response function towards the higher energies. Besides that there are visible irregularities in the response function around 67, 185 and 497 keV.

Chapter 3

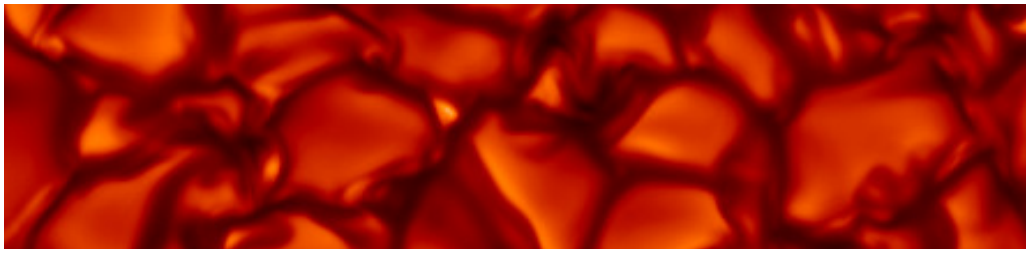

Data analysis

Those who forget their history

are convicted

to live it through

again.

This chapter contains observations of three X-class solar flares and one M-class flare. The most peculiar flare of GOES classification X1.0 was well documented by instruments working in X-rays, UV and visible wavelength range. The characteristic emission in the higher order Balmer lines was not detected, while the WL peak emission was co-temporal with the peak of hard X-rays. The analysis of X-rays and γ-rays did not provide a specific set of flare beam parameters, but provided evidence of proton beams. The analysis presented in this chapter was published in Procházka et al. (2017).

3.1 The Balmer series of the 10 and 11 June 2014 X-class flares

On 10 June 2014 active region (AR) 12087 emerged over the eastern limb and produced three X-class flares and one M-class flare over a period of 24 hours. Sample IS spectra of the first two flares (X2.2 and X1.5) in Figures 3.1 and 3.2 showed strong emission in the Balmer lines that is the clear signature of type I WLFs. The Ca II lines were stronger than the Balmer lines in the X2.2 event, but weaker in the following X1.5 event. The third flare (M3.0, Figure 3.3 and 3.4) showed weak emission in both Balmer and Ca II lines, but because of a lack of observations of flares with similar GOES classification, it is not possible to say if this is common or not. The fourth flare (X1.0, GOES peak 9:06 UT) did not show any clear emission in the higher order Balmer lines (Hγ and higher, Figure 3.3), while the flare produced at least three Hα kernels (Figure 3.4). In the pre-flare phase all three kernels looked equally important, but the north-western one became dominant in the later stage of the event. However, it was not as bright as the brightest kernel of the preceding M3.0 event peaking at 8:07 UT. The flaring kernels in Hα of both M3.0 and X1.0 events were identical.

Unlike the other events, the X1.0 flare was observed using IS from its pre-flare phase until the early gradual phase, and so represents a unique event to study. When the flare progressed, a weak emission in the cores of Ca II K&H lines was detected. The long lasting bump at shorter wavelengths ($<$ 400 nm, rows 3 to 6 in lower panel of

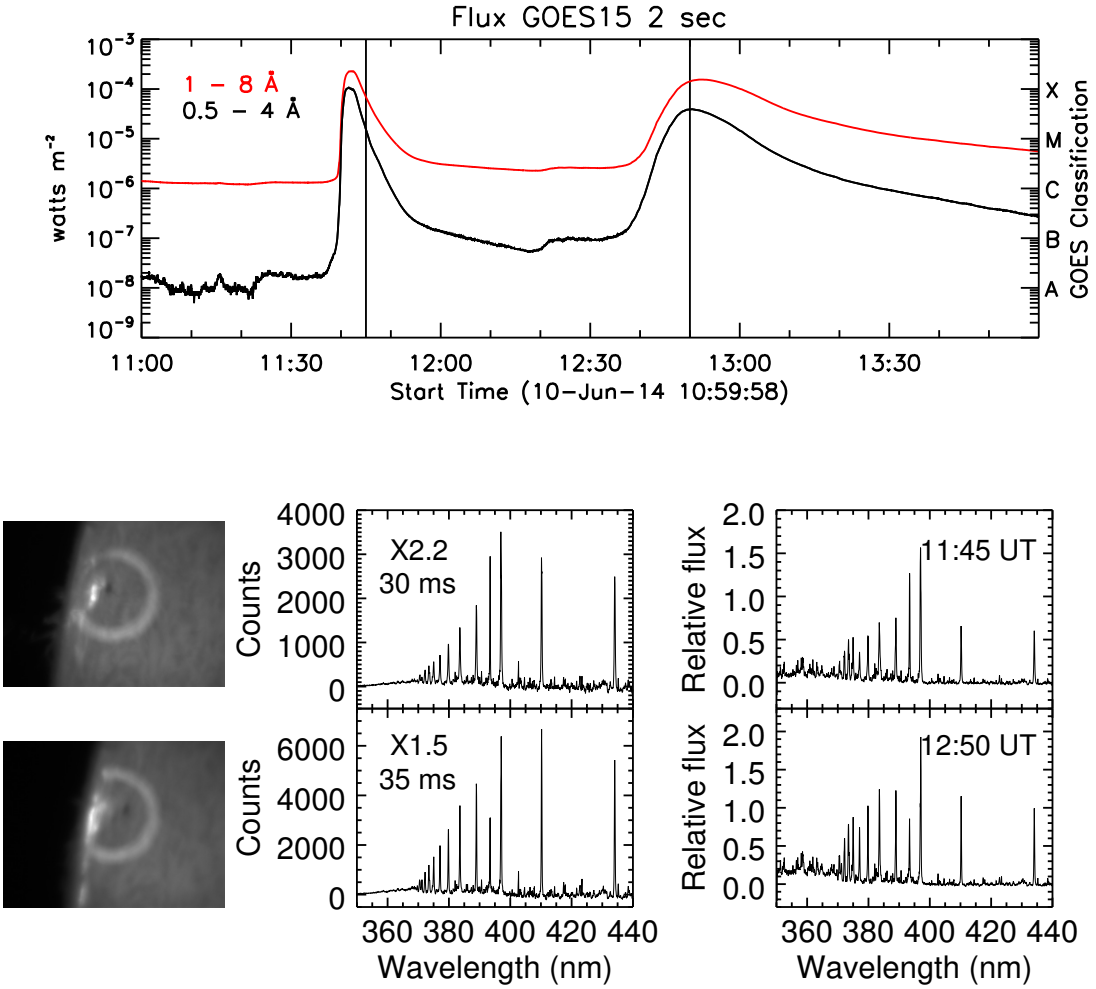

Figure 3.1: Observations of type I WLFs on 10 June 2014. Upper panel: Light curves of hard (black) and soft (red) X-rays from GOES. The vertical lines mark the times when the spectra and the images in the bottom panel were recorded. Bottom panel: The left column shows a context Hα filtergram, the second column shows the flare excess and the third column shows the excess related to a reference spectra taken at the end of observations, as recorded by the IS. The spectrum is integrated from the area within the bright circle.

Figure 3.3) is a consequence of a pre-flare brightening in the studied AR. It appeared suddenly at 8:48 UT (marked as B2 in Figure 3.5), which was few minutes earlier than a similar emission observed at the low energy X-ray channels.

Two sets of spectra were obtained for the two events in the studied active region. The first set commenced at 8:07 UT prior to the peak of the M3.0 event (8:09 UT) and was terminated at 8:39 UT for calibration purposes. The spectra were recorded with

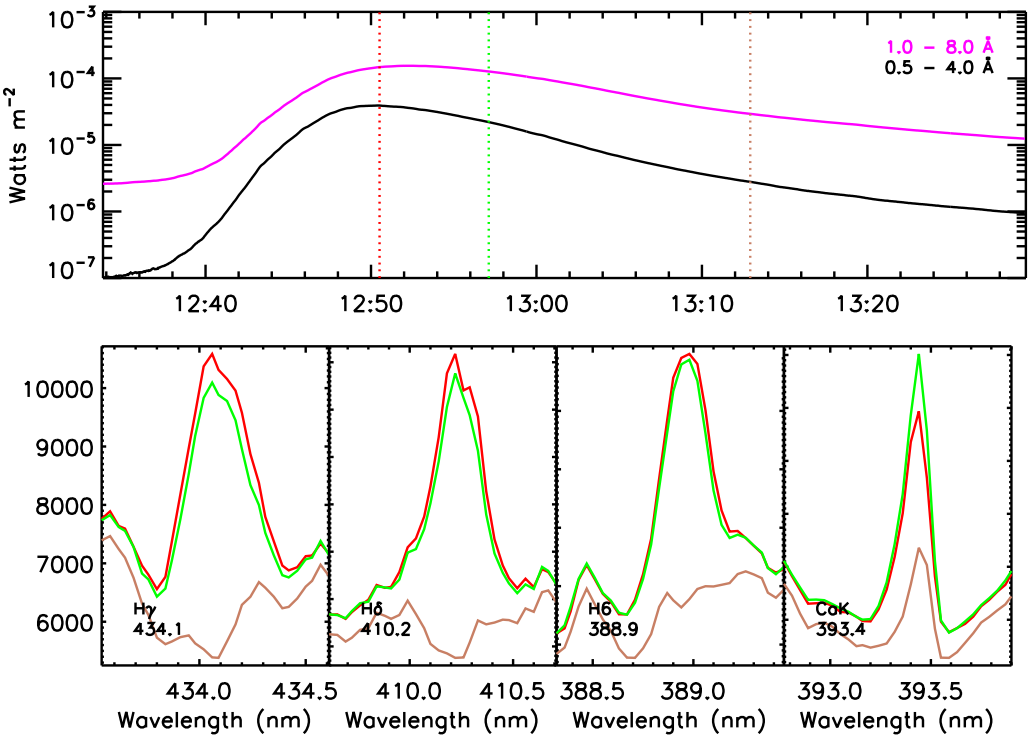

Figure 3.2: Spectral profiles of Hγ, Hδ, H6 and Ca II K lines during the X1.5 flare peak. The vertical lines in the upper panel mark the colour coded times of spectra recording. The vertical axis on the lower panel is in relative units.

a cadence of 0.09 s and an integration time of 40 ms. Once the calibration data were acquired at 8:44 UT, the data acquisition recommenced with an integration time of 30 ms to prevent saturation of the detector. The error of spectral measurements varied between 0.5% for wavelengths $\sim$ 440 nm and 2% for wavelengths $\sim$ 360 nm and the Ca II K&H lines. The error was determined as the standard deviation over a set of 50 reference spectra recorded with an integration time of 30 ms.

The spectra of the X1.0 event did not show any obvious emission in the higher order Balmer lines (detail in Figure 3.6) at any stage of the flare, unlike all the other flares presented. On the other hand, the filtergrams in Hα clearly showed the flare, but the light curves in Figure 3.5 show that the emission was not as strong as expected for an X-class flare when compared with the antecedent M3.0 event.

The data acquisition included Hα context images with a cadence of 0.2 and 1 s,

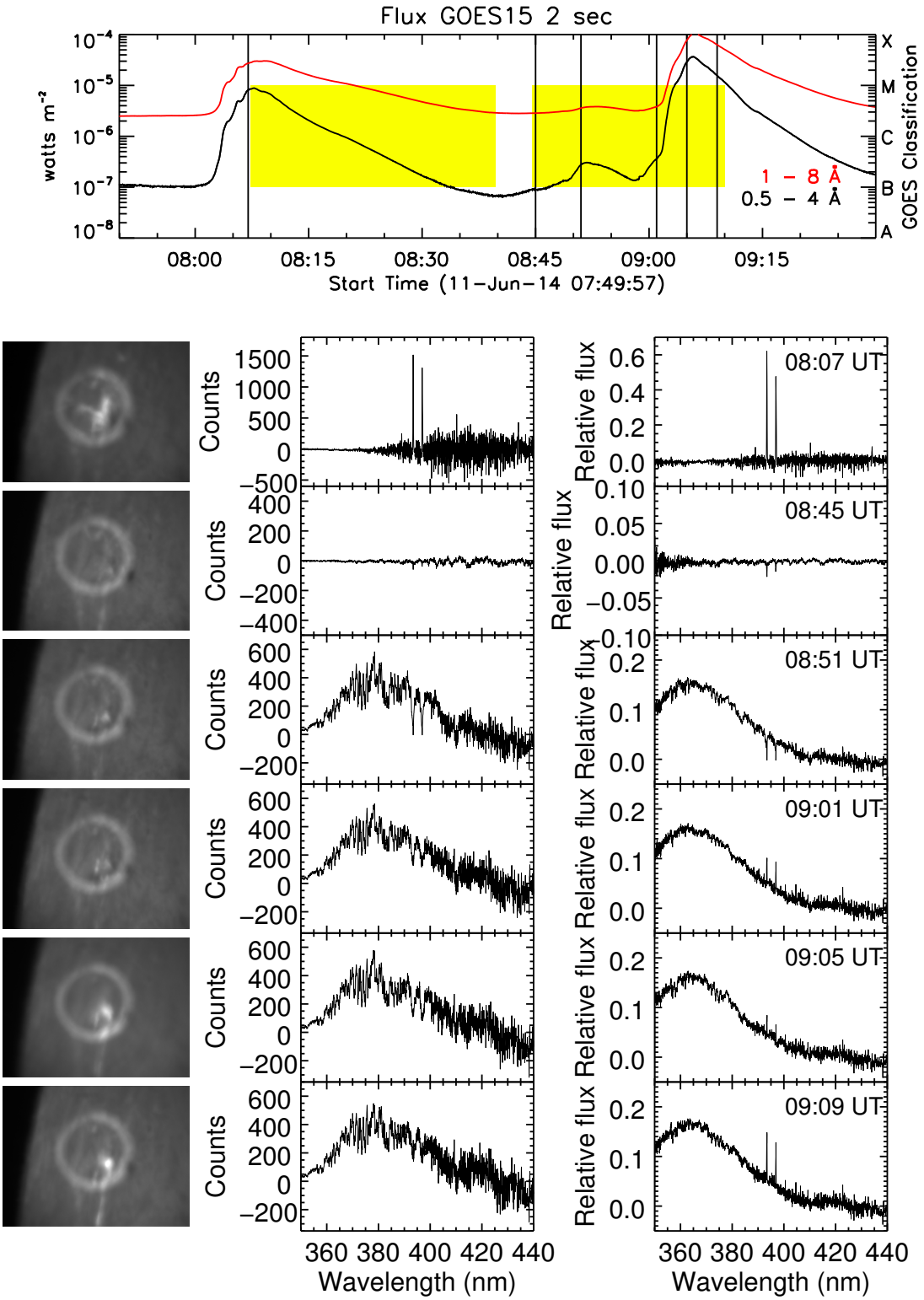

Figure 3.3: Observations of a type II WLF on 11 June 2014. For a description see a label of Figure 3.1. For all the snapshots a reference spectrum captured at 8:44 UT was used. The yellow bars mark the availability of UV/visible spectroscopic data.

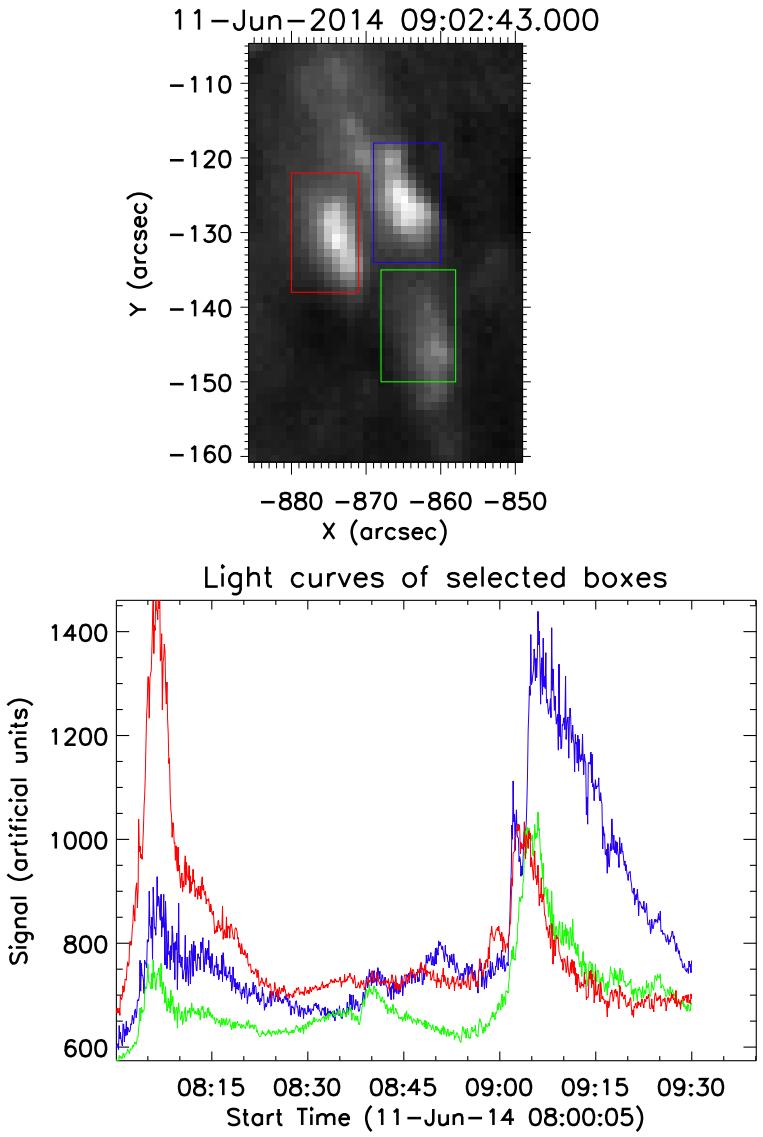

Figure 3.4: Upper panel: Hα filtergram recorded at Kanzelhöhe Observatory, Austria, lower panel: colour coded light curves integrated over the Hα flare kernels.

respectively. The diaphragm's size was 10 mm, which corresponds to 57 arcsec. An area affected by the flare with respect to the whole measured area (denoted as *filling factor* ff) was evolving during the flare, as shown in the left column of Figure 3.3. The analysis of Hα images resulted in an estimate of the ff. This was 7.3% during the flare peak and gradually decreased to 3.9% at 9:09:30 UT. Flaring pixels were identified as those that had a value that was twice the median of the signal across the Hα image. Due to strong seeing effects the ff has an error of around 10%. For the analysis only

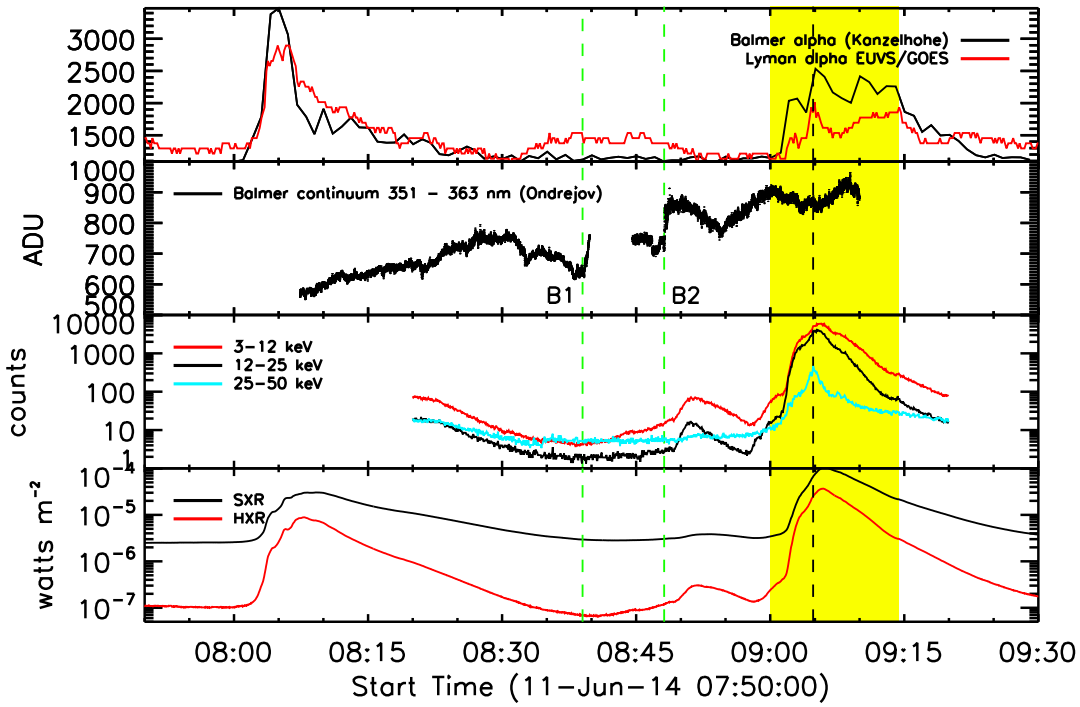

Figure 3.5: Light curves of hydrogen emission (first and second panels) and the X-ray emission (third-RHESSI and fourth-GOES panels) of M3.0 and X1.0 events. Data in first, second and third panels are in relative units. The dashed green lines mark sudden brightenings (B1 and B2) in the Balmer continuum. The yellow bar highlights the type II WLF.

images taken at times with the best seeing were used.

The spectra obtained with IS, integrated over the peak of the flare (9:04:45-9:05:15 UT), in Figure 3.7 do not show an obvious emission in the Balmer lines, but it would be premature to claim that there was no emission, since it could have been weaker than noise. In order to estimate the maximal emission in the Balmer lines, the noise had to be quantified. It has to be mentioned that the measured signal naturally fluctuated significantly, which explains the shift of the continuum in Figure 3.7 towards to positive values. The second panel of Figure 3.5 shows that these fluctuations do not have any obvious connection with the flare.

The seeing effect and temporal variations in the studied active region do not allow us to calibrate the observations, and so for quantifying purposes we have compared the Ca

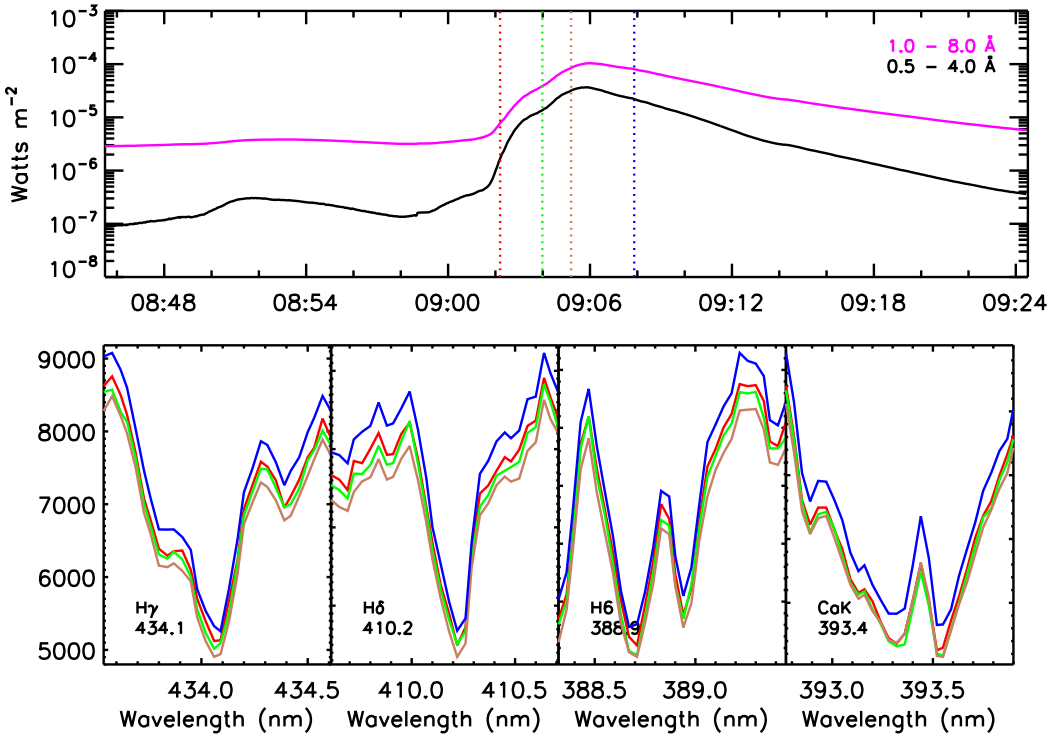

Figure 3.6: Observations of the X1.0 event. Description as in Figure 3.2.

II K line to the Hγ. The Hγ was chosen as a representative of the higher order Balmer series, since IS had a signal at 434 nm strong enough and there is no reason to assume that it would show qualitatively different behaviour from other higher order Balmer lines. The magnitude of fluctuations at the wavelength of the Hγ line was estimated and compared with the height of the Ca II K line (blacked dashed lines in Figure 3.7). The maximum Hγ vs. Ca II K line ratio (ratio between the two blue arrows in Figure 3.7) is then 0.15. A higher value would imply that the emission in the Hγ line would be visible in the spectra.

3.2 Lyman series of the 10 and 11 June 2014 X-class flares

For the measurements of the Lyman continuum the *RANdom Sample Consensus* (Fischler & Bowles 1981) method was applied on the Version 5 MEGS-B data (Milligan et al. 2014). To obtain the Lyman α irradiance the channel E of the EUV Sensor on board of the GOES satellites was used.

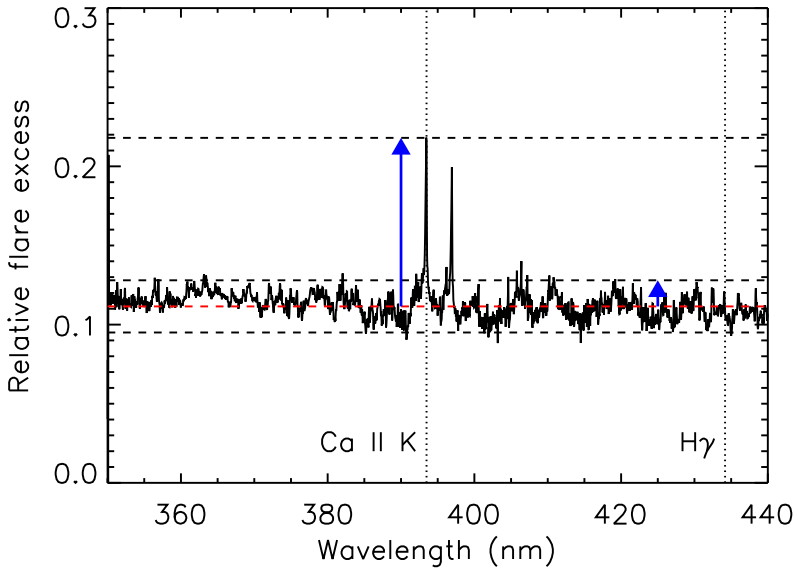

Figure 3.7: The relative flare excess recorded during the flare peak (averaged over 9 : 04 : 45 – 9 : 05 : 15 UT). The reference spectrum was taken at 8 : 54 : 45 – 8 : 55 : 15 UT. The blue arrows mark heights of Ca II K line and half of the width of a fluctuation band, respectively. The red line marks the estimated level of continuum.

For the X2.2 and X1.5 class flares on 10 June no EVE/MEGS spectra were acquired, but GOES/EUVS detected a significant difference between both events (Figure 3.8). The light curve of Lyman α shows a short lasting sharp rise during the first event, but a significantly weaker and more gradual longer lasting increase during the subsequent event.

Figure 3.9 shows that during the 11 June 2014 flares all light curves of Lyman lines and Lyman continuum correlate well, and peak together, but the X1.0 (peak 9 : 05 UT) event showed a significantly suppressed Lyman emission in comparison with the M3.0 event (peak 8 : 07 UT). A weak emission in Lyman α was observed, but the higher order lines and Lyman continuum only showed an emission at the level of noise. These observational characteristics of the Lyman lines match the behaviour of the Balmer series.

The EVE spectra in Figure 3.10 also show only a weak emission in Lyman lines

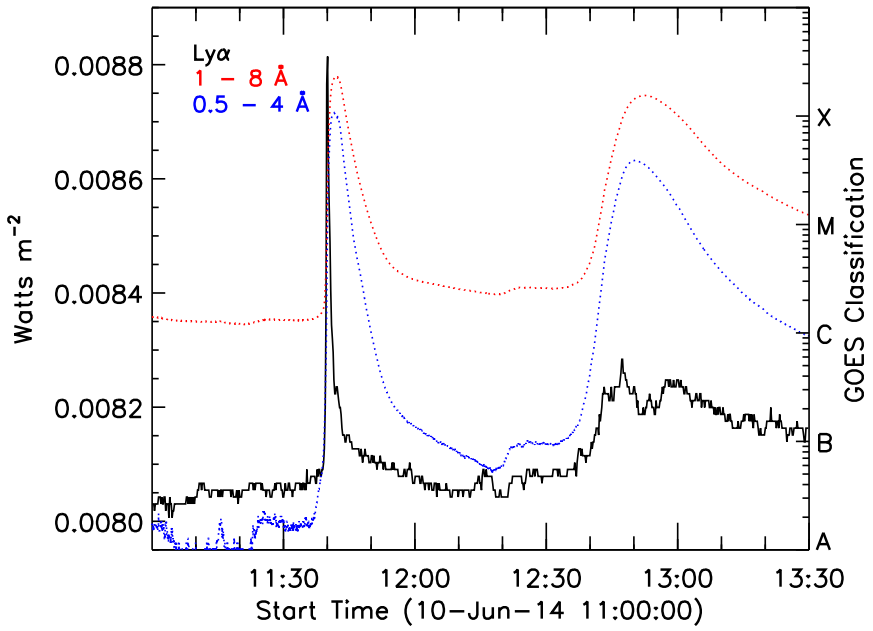

Figure 3.8: Light curves of GOES/EUVS Lyman α together with GOES X-ray data overplotted.

and a negligible increase of the Lyman continuum, when compared to another flares of the same GOES classification.

3.3 The HMI 617 nm continuum

All the observed X-class flares showed WL signatures detected by HMI at 617 nm. The WL emission in the X2.2 class flare on 10 June had two clearly distinguishable high-contrast kernels (Figure 3.11) with fainter tails that formed ribbons in the later stage of the event. The following X1.5 event showed two longer ribbons with three weak kernels located closer to the limb out of the associated active region (Figure 3.12).

An analysis of the HMI continuum in the 11 June X1.0 event showed two rather weak ribbons (localised using difference imaging) peaking simultaneously with all previously described light curves. The temporal match between the WL continuum and RHESSI higher-energy channel in Figure 3.13 is particularly significant. The differ-

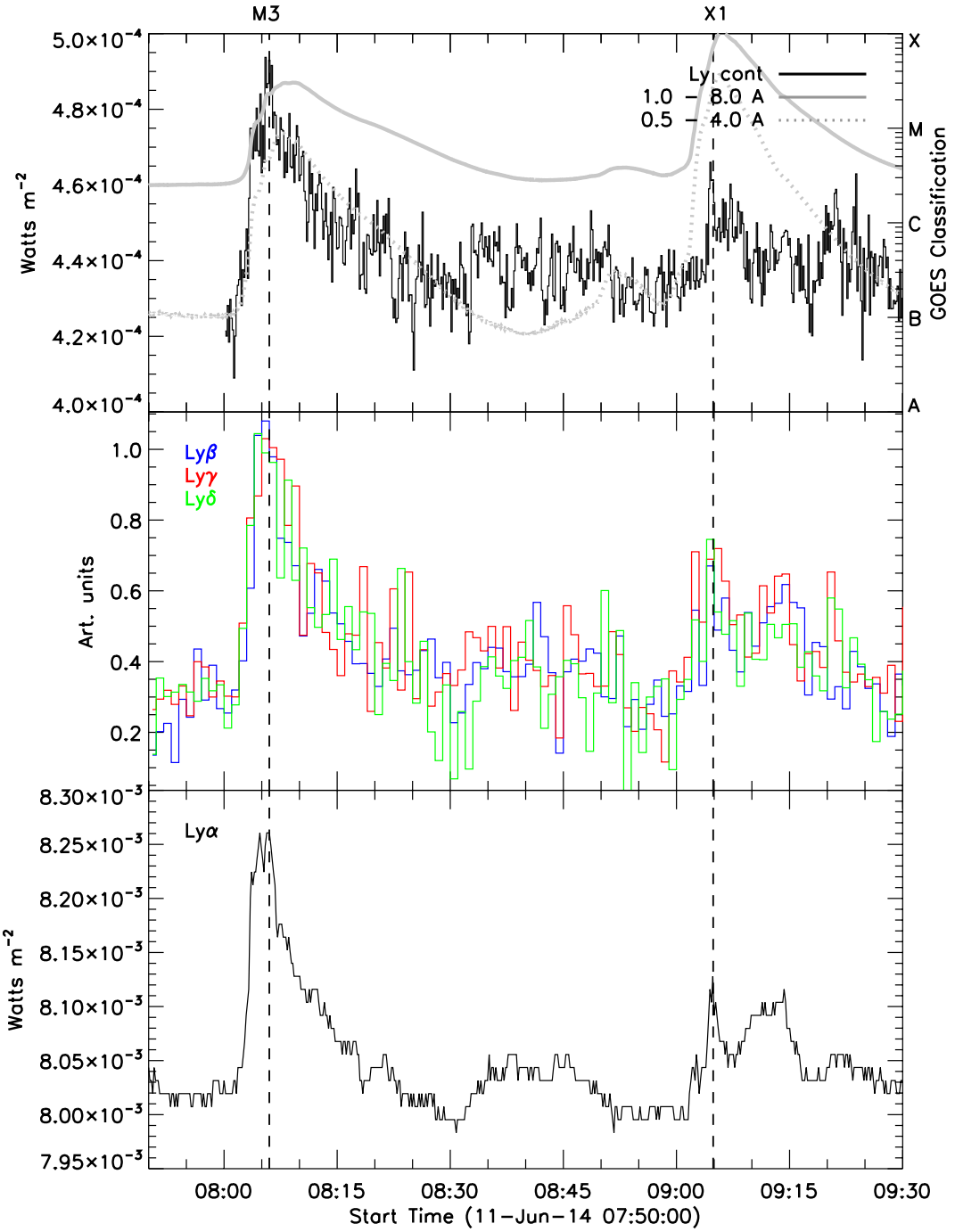

Figure 3.9: Spectral measurements in the EUV range during the studied event. The top panel shows the Lyman continuum and GOES HXR and SXR channels. The middle panel shows the flux in Lyman β, γ and δ lines as recorded by SDO/EVE. The lower panel shows the flux in Lyman α line as recorded by GOES. The vertical dashed lines show the flare peaks.

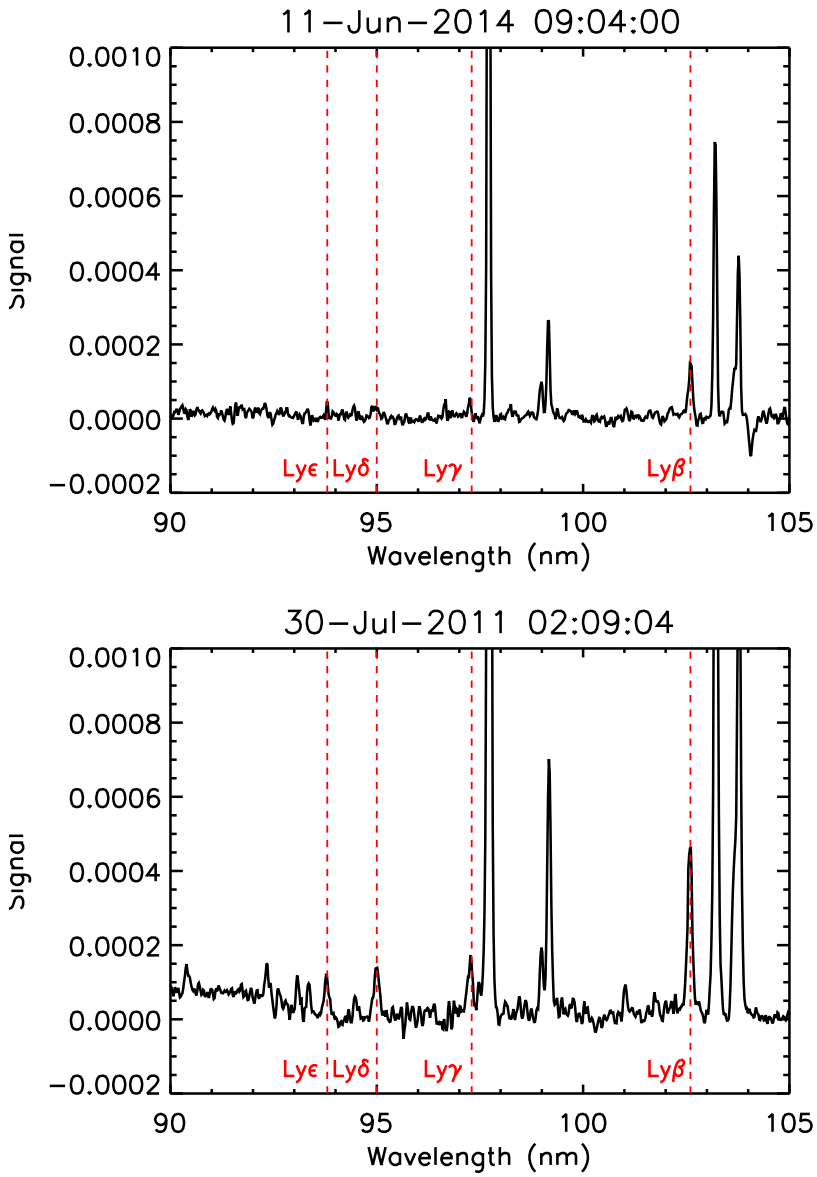

Figure 3.10: EVE spectra of X1-class flares. The upper panel shows a weak flare excess during the studied event, the lower panel shows another solar flare excess for comparison. The upper panel shows that the flare excess in all spectral lines is weaker compared to a 'typical' flare. The higher order Lyman lines and Lyman jump are hardly visible.

ence between the pre-flare and after-flare continuum levels and great spatial variations made it ambiguous to determine the quiet level and consequently only a lower limit of the WL contrast could be determined. For the northern and southern kernels (red and blue, respectively) it was found to be 1.07 and 1.05, respectively.

The HMI data were used to estimate the flaring area. Two thresholds, that most

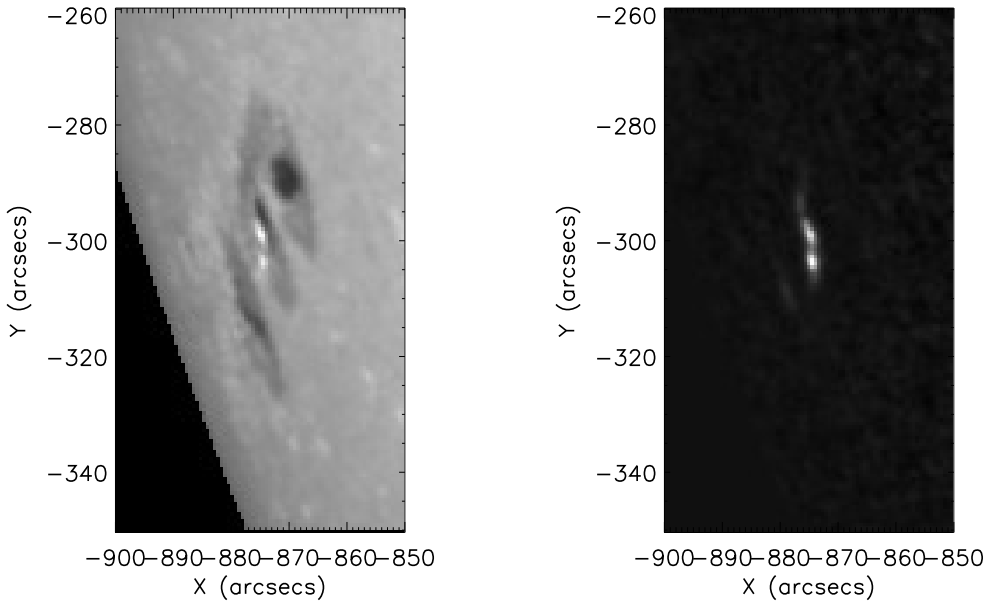

Figure 3.11: HMI image of the 10 June 2014 X2.2 event. The left panel shows an image of the solar photosphere taken at 11 : 39 : 40 UT. The right panel shows a difference image with the reference image taken at 11 : 38 : 10 UT.

suitably represented upper and lower area estimates, were set on the excess emission. The upper threshold yielded contours around only the bright kernels, meanwhile the lower threshold yielded contours around the whole ribbons including their fainter parts (Figure 3.14). Hence, the apparent flaring area was in the range $4.5\times10^{16} - 1.3\times10^{17}$ cm^2. However, when considering geometric distortions, since the active region was relatively close to the limb, it was actually about 2.5 times larger ($1.1\times10^{17} - 3.3\times10^{17}$ cm^2).

3.4 X-ray spectroscopy

No RHESSI data are available from the 10 June X-class flares. X-ray spectra for the studied 11 June X1.0 event were available from both the RHESSI and Fermi/GBM instruments. After the background subtraction, the standard fitting technique was ap-

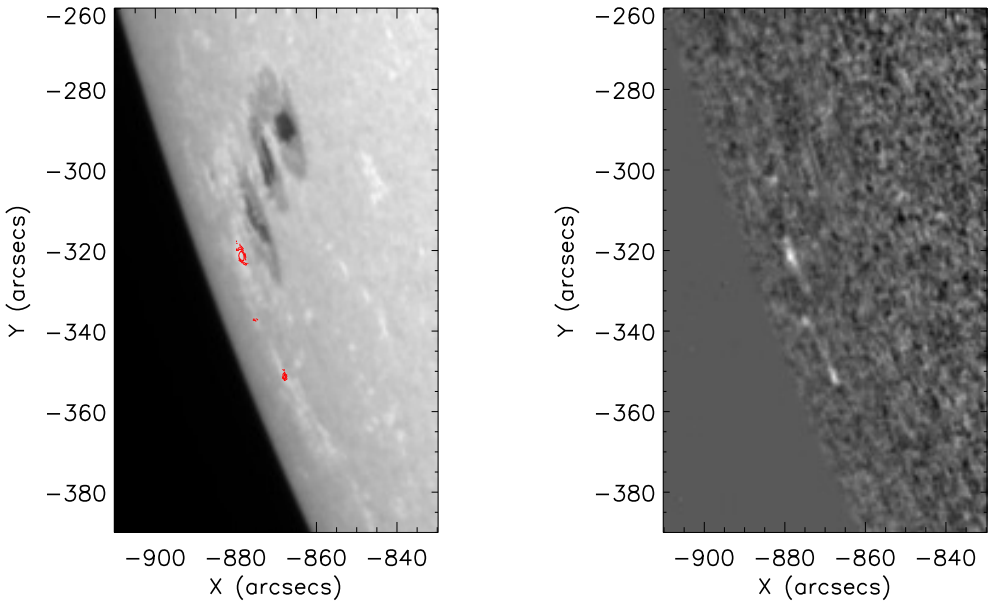

Figure 3.12: HMI image of the 10 June 2014 X1.5 event. The left panel shows an image of the solar photosphere taken at 12 : 47 : 10 UT with red contours marking the WL kernels. The right panel shows a difference image with the reference image taken at 12 : 45 : 40 UT.

plied. The fit included a gaussian for the thermal component, a power-law for the non-thermal component and corrections like pulse pile-up, albedo, and response matrix (Figure 3.15), for details of the fitted components see Section 1.4. The data were fitted with a time step of 20 s. The method applied to RHESSI spectra did not lead to conclusive results. The spectral index was approximately equal to 3, which indicates an exceptionally hard spectrum. In such a case the slopes on both sides of E_C of non-thermal distribution are similar, therefore the value of E_C is very difficult to find.

Indeed, the alternative approach with fitting only the flare peak spectra divided into ten time intervals with E_C fixed at 20, 40, 60, 80, 100, and 120 keV (based on references in Chapter 1.4, 20 – 120 keV is a range in which E_C is usually found) proved that the quality of the fit represented with χ^2 in Figure 3.16 turned to be independent of E_C. Therefore, it was impossible to determine the E_C of the electron distribution in this

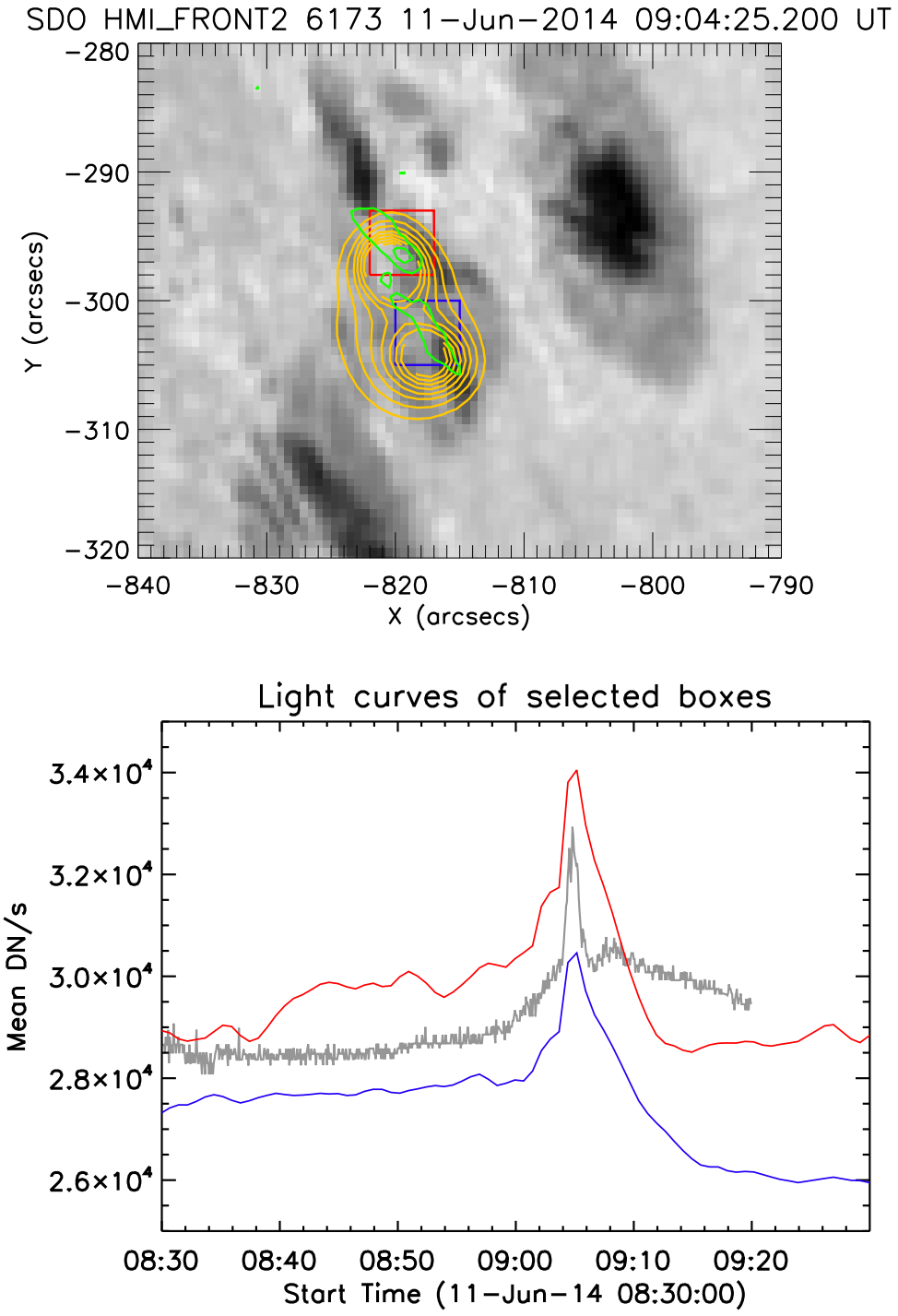

Figure 3.13: Emission in white-light from HMI. The upper filtergram shows the WL ribbons (green contours) with a location of the 40 – 70 keV HXR sources observed by RHESSI in time interval 9 : 04 : 14 – 9 : 04 : 40 UT (yellow contours). The lower panel shows light curves from the two WL ribbons (colour coded) and corrected count rate of the RHESSI 50 – 100 keV channel (grey).

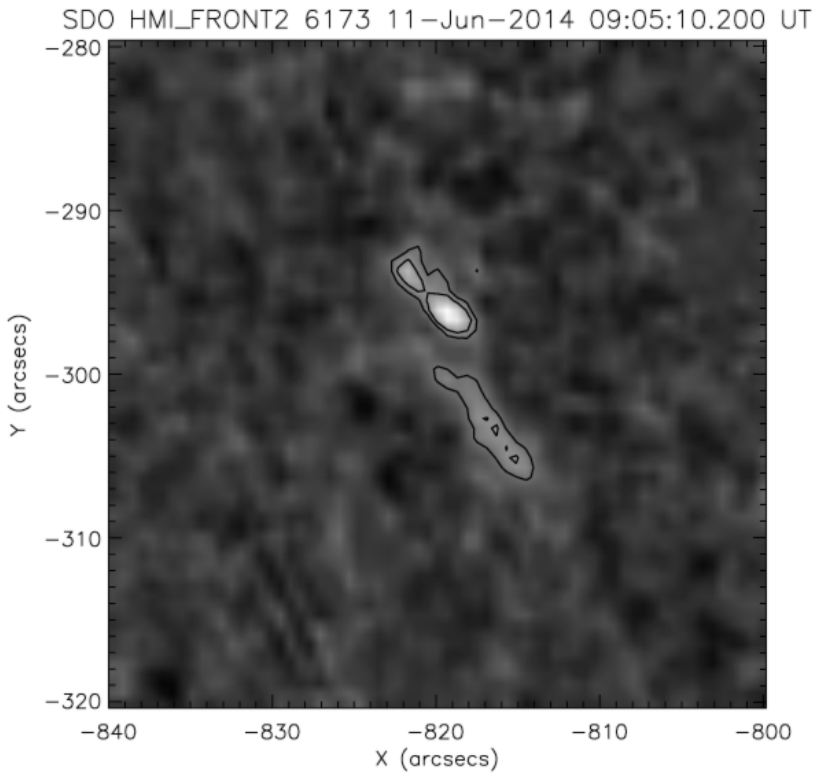

Figure 3.14: HMI difference image with contours used to calculate the flaring area.

E_C (keV)	Power (erg s^{-1})	Maximum flux (erg cm^{-2} s^{-1})
20	15.9×10^{26}	$4.85 - 14.5 \times 10^9$
40	7.6×10^{26}	$2.30 - 6.91 \times 10^9$
60	5.1×10^{26}	$1.55 - 4.64 \times 10^9$
80	4.3×10^{26}	$1.30 - 3.90 \times 10^9$
100	3.8×10^{26}	$1.15 - 3.45 \times 10^9$
120	3.2×10^{26}	$0.97 - 2.91 \times 10^9$

Table 3.1: Estimates of the power of non-thermal electrons in the impulsive phase of the flare and the derived maximum flux for given values of the low energy cutoff with respect to the HMI flaring area.

event, and consequently the same is true for the power in the non-thermal electrons.

Since RHESSI does not allow us to determine a single value of E_C, the power in non-thermal electrons had to be calculated for the whole range of plausible E_C. When considering the flaring area estimates based on HMI images, the energy flux estimated during the peak of the flare is mentioned in Table 3.1.

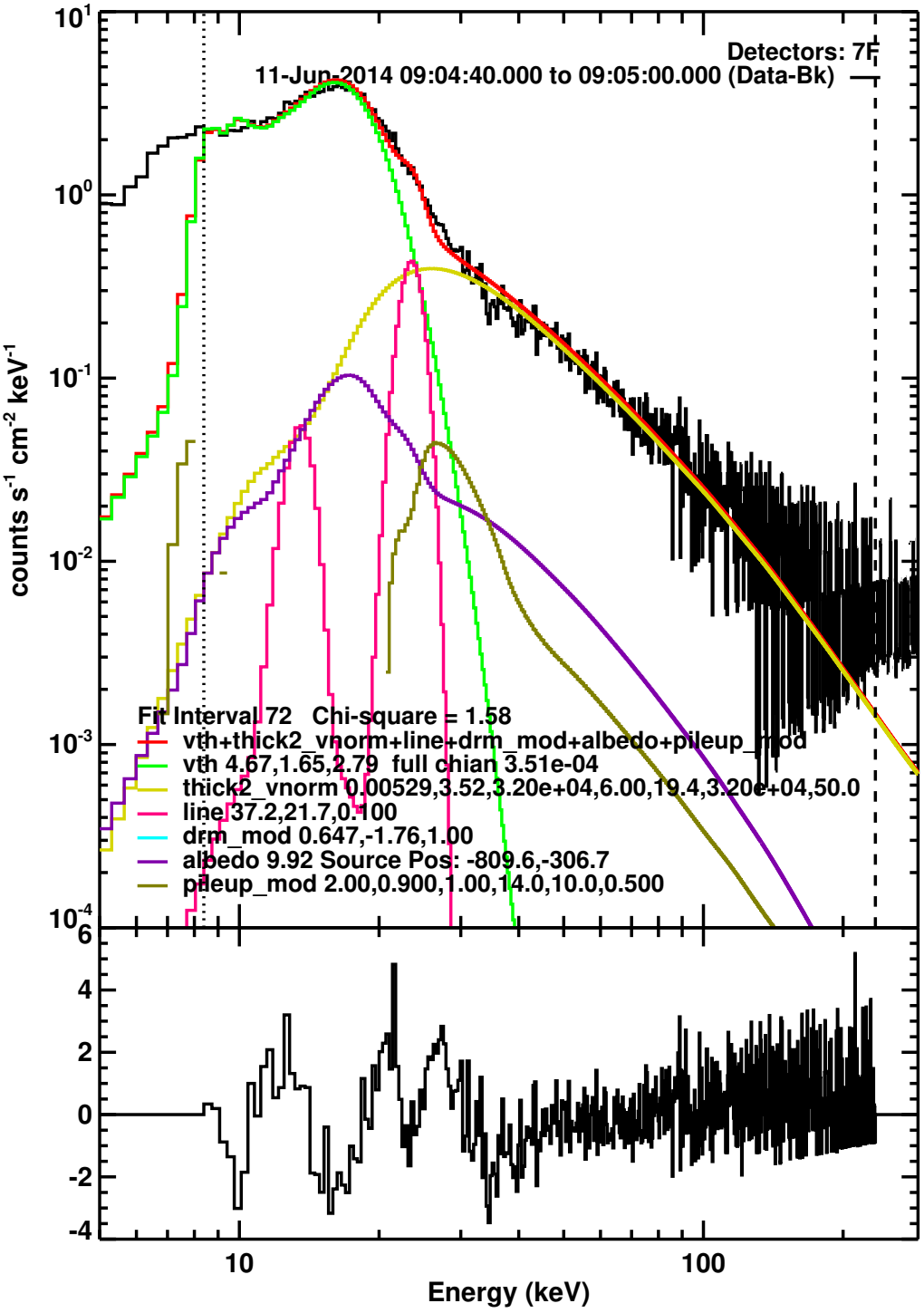

Figure 3.15: RHESSI spectrum of the flare peak. The detector #7 was the least affected from the instrument degradation during this phase of the mission. In the upper panel the vertical lines show the energy interval within which the spectrum was fitted using the OSPEX software. The black line represents the data with the background subtracted and the red line represents the final fit. The green, yellow, pink, blue, purple and beige lines represents the fitted components - the thermal component, the non-thermal component, the Gaussian line, the pseudo function for fine-tuning RHESSI, the albedo and the pileup, respectively. The lower panel shows the fit normalised residua.

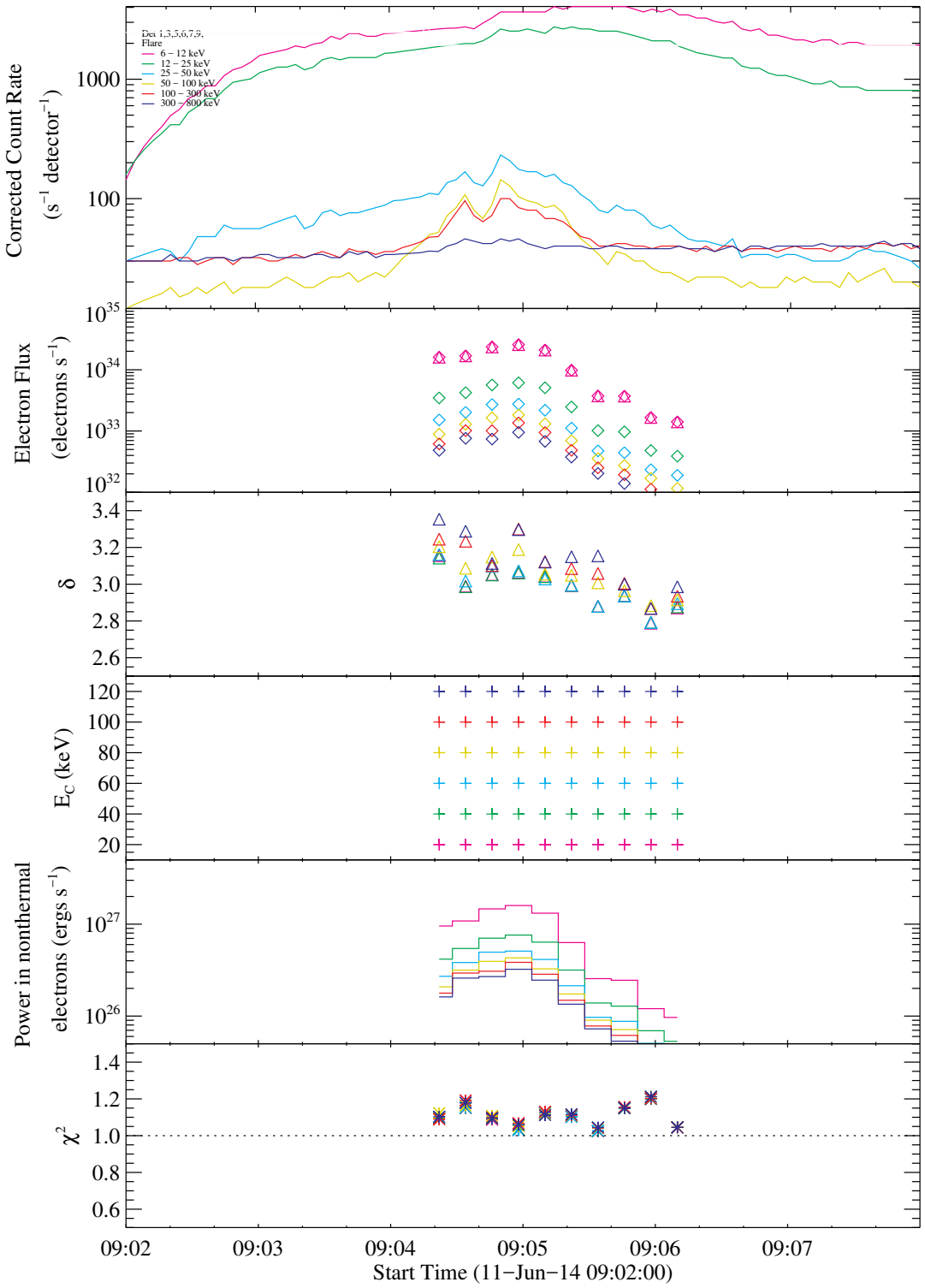

Figure 3.16: Graphical output of RHESSI fitting process with E_C fixed. The top panel shows light curves of the standard RHESSI energy channels, the following panels show results of the fitting process. The fits with different values of E_C are colour coded.

RHESSI data provided enough counts to reconstruct the X-ray images using the Pixon method. Figure 3.17 shows a single thermal source in the energy range 12 - 25 keV and two non-thermal sources in the energy range 30 - 60 keV. The thermal source is interpreted as the flaring loop top located in the corona and the two non-thermal sources are interpreted as the foot-points, where the electron beams hit the chromosphere.

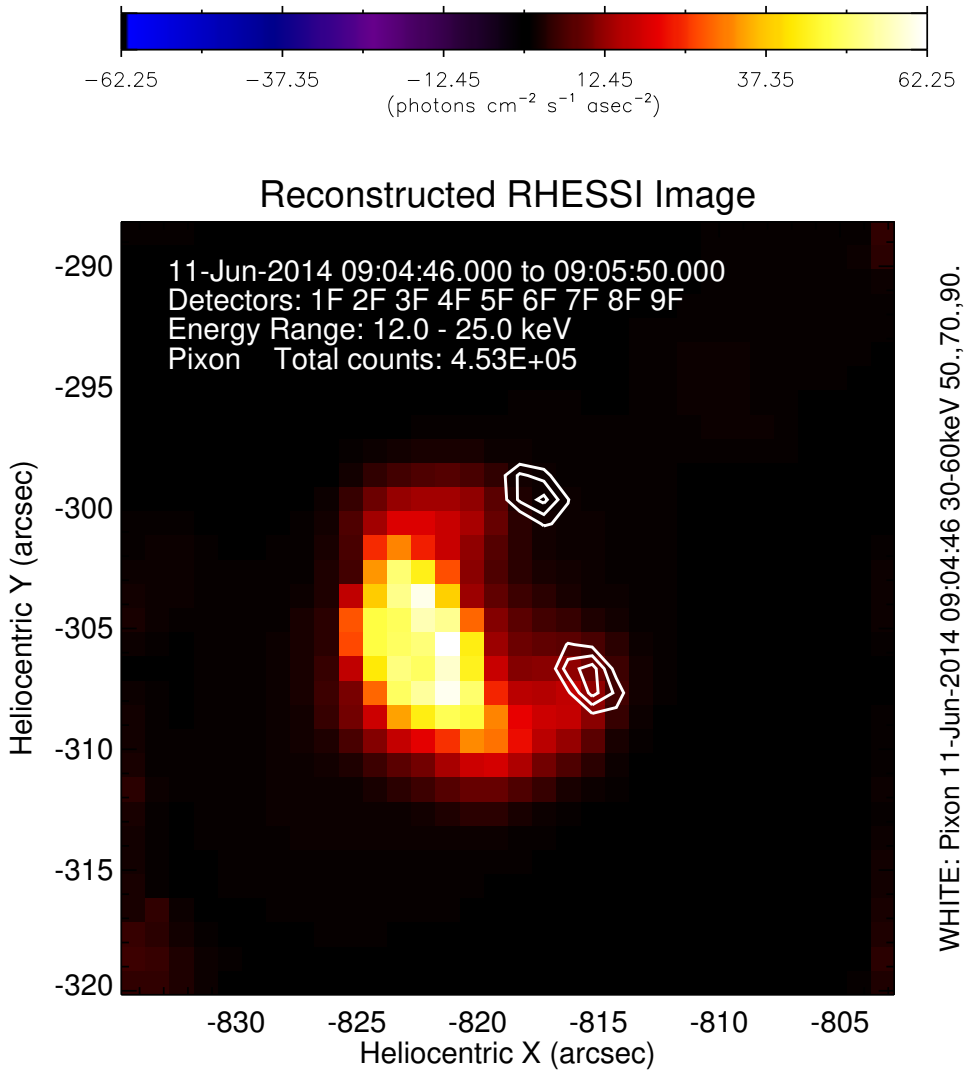

Figure 3.17: RHESSI 12 – 25 keV X-ray image of the 11 June X1.0 WLF peak (9 : 04 : 46 – 9 : 05 : 50 UT). The 30 – 60 keV white contours representing 0.5, 0.7 and 0.9 of the maximum signal are overlaid. An arc representing the flaring loop with the footpoints (contours) is clearly resolved.

Data from Fermi/GBM provided evidence for proton beams in the flare. The

spectra integrated over two time intervals during the peak of the flare were analysed (9 : 04 : 13 – 9 : 05 : 35 UT and 9 : 04 : 29 – 9 : 04 : 50 UT). The background was determined by using a linear fit on a spectrum recorded before the flare in the time interval 8 : 56 : 08 – 9 : 01 : 20 UT and after the flare in the time interval 9 : 08 : 39 – 9 : 21 : 47 UT. Four components were used when fitting the flare spectra: power-law for electron bremsstrahlung, Gaussians for the 0.511 MeV and 2.22 MeV lines and a template for the de-excitation of nuclear lines included in OSPEX (Schwartz et al. 2002). The template assumes a flare at heliocentric angle of 60°, downward isotropic distribution of ions, α/proton ratio equal to 0.22 and a power-law energy distribution with $\delta = 4$. The template is normalised as:

$$1\,\text{photon}\; s^{-1}\, cm^{-2}\, keV^{-1} \sim 8.5946 \times 10^{29}\,\text{protons}_{>30MeV}\; s^{-1}, \tag{3.1}$$

where $\text{protons}_{>30MeV}$ are protons with energies greater than 30 MeV (Trottet et al. 2015). The broader time range was used to provide guiding values of the model parameters for a secondary fit of the flare peak.

Table 3.2 shows that the number of high energy ions detected in the broader time range is only about 6.5% greater than the number of ions detected in the HXR peak of the flare (9 : 04 : 29 – 9 : 04 : 50 UT). This clearly shows that high energy ions were co-temporal with high energy electrons, within the temporal resolution of the fits.

Integration interval	$I_{E_p>30MeV}$	N_{30}
9 : 04 : 13 – 9 : 05 : 35 UT	$1.2 \pm 0.2 \times 10^{29}$ ions s^{-1}	$9.8 \pm 1.6 \times 10^{30}$ ions
9 : 04 : 29 – 9 : 04 : 50 UT	$4.4 \pm 0.8 \times 10^{29}$ ions s^{-1}	$9.2 \pm 1.7 \times 10^{30}$ ions

Table 3.2: Fermi/BGO fitting results. $I_{E_p>30MeV}$ is a count rate of > 30 MeV ions averaged over the selected time interval. N_{30} is the total number of > 30 MeV ions detected.

Since the proton/ion beam flare scenario is understudied, it is not known what the typical proton/ion beam parameters are. However, Švestka (1970) presented an analysis where he claimed that 20 MeV protons can penetrate deep enough to trigger

a short-lived increase of the UV/visible continuum. If it is assumed that proton/ion beams have the same power-law distribution with sharp E_C (where there are no protons/ions with energies lower than E_C in the beam) as electron beams, then it is reasonable to adopt the 20 MeV as the upper limit for E_C. In order to calculate the power in non-thermal protons/ions, the Fermi/GBM spectral fit and HMI flaring area were used with E_C equal to 2, 4, 8 and 16 MeV (Table 3.3).

E_C (MeV)	Power (erg s^{-1})	Maximum flux (erg cm^{-2} s^{-1})
2	7.06×10^{27}	$21.4 - 64.2 \times 10^{9}$
4	8.82×10^{26}	$2.67 - 8.02 \times 10^{9}$
8	1.10×10^{26}	$0.33 - 1.00 \times 10^{9}$
16	1.38×10^{25}	$0.04 - 0.13 \times 10^{9}$

Table 3.3: Estimates of power in non-thermal protons during the impulsive phase of the flare and the derived maximum flux for given values of the low energy cutoff with respect to the HMI flaring area.

3.5 Summary

The multi-instrument analysis of the X1.0 WLF yielded a finding that this flare showed extraordinary spectral signatures in all wavebands. The absence of Balmer lines was not a consequence of a technical error during the observations, since the two other X-class flares observed with the same instrument showed clear emission during their impulsive and gradual phases. The suppressed Lyman lines point at extraordinary conditions in the flaring atmosphere. Indeed, the X-ray and γ-ray observations show an extremely hard electron spectrum and the presence of a significant proton population in the beam.

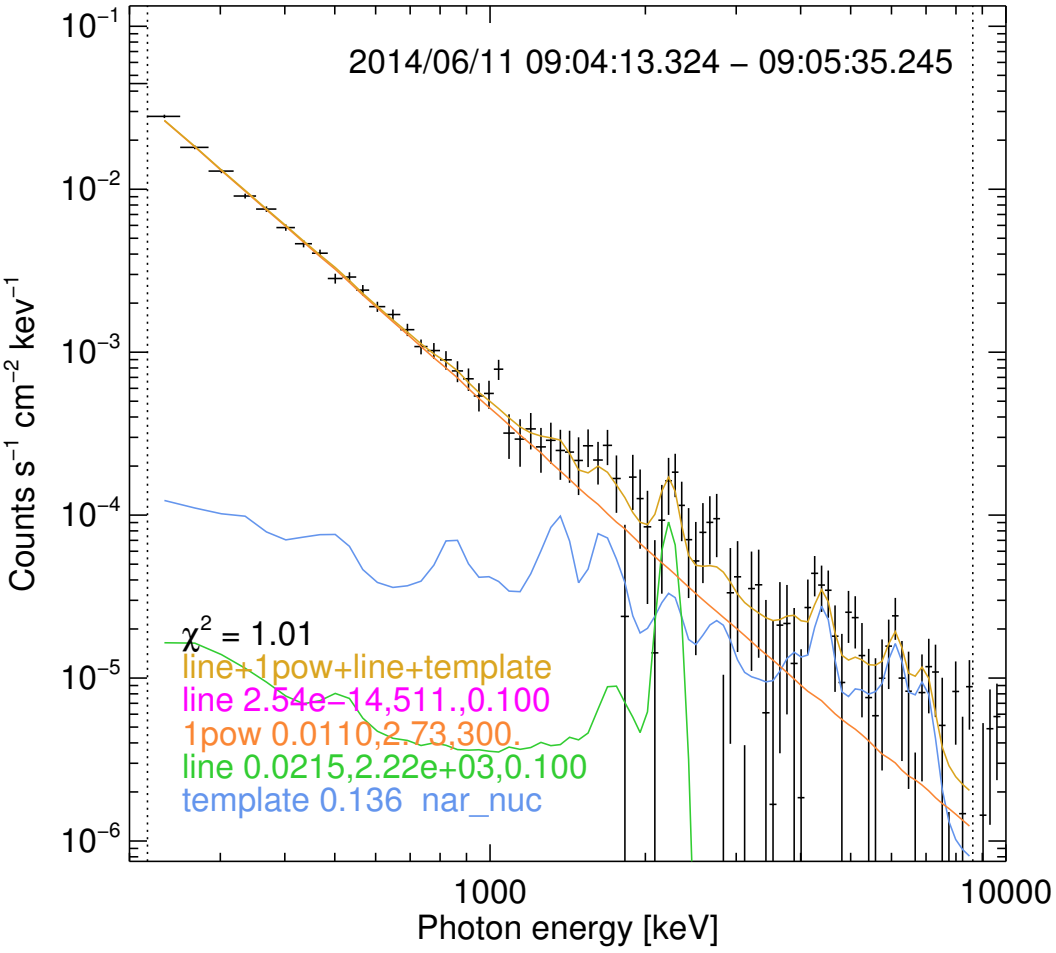

Figure 3.18: The fitted Fermi/GBM spectrum in a time range 9 : 04 : 13 – 9 : 05 : 35 UT. The dotted lines mark an energy range used for the fitting process. The yellow line represents the sum of the fitted components that are the Gaussians for the 2.22 MeV (green) and the 511 keV (purple) lines, the power-law for the electron bremsstrahlung (purple), and the template for the de-excitation of nuclear lines (blue).

Chapter 4

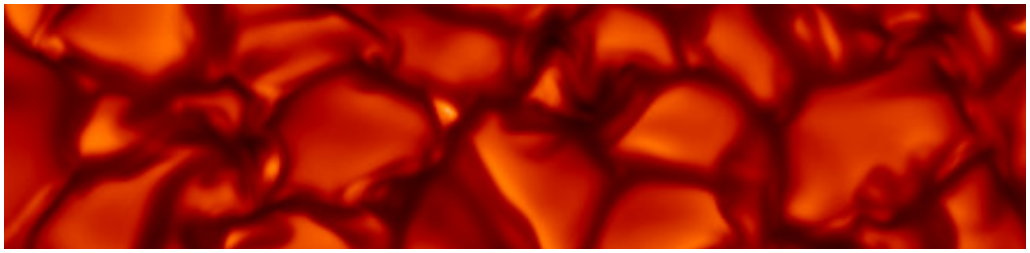

Radiative hydrodynamic modelling

You have achieved success
in your field when you
don't know whether
what you're doing
is work or play.

This chapter describes atmospheric models that were used to explain the extraordinary spectral features of the X1 event from 11 June 2014. The RADYN code (Carlsson & Stein 1992, 1994, 1995; Allred et al. 2015) is a radiative hydrodynamic code, which uses the E_C and beam flux as input parameters to generate flare model atmospheres. It allows us to study changes of all atmospheric parameters during the interaction of the beam with the solar atmosphere, as well as the influence of the beam on the output spectra. After producing a set of RADYN models, their outputs can be assessed and the model(s) with the best match is/are likely to have input parameters close to those responsible for the observed spectral features. The RH code (Uitenbroek 2001) builds on the RADYN output when using partial redistribution in order to reliably calculate the strong resonance lines. This is particularly important when reproducing the Lyman lines or Ca II K&H lines.

4.1 Radiative transfer equation

The radiation field in the vicinity of a radiating surface with area dA can be described by the *specific intensity* I_ν defined as

$$I_\nu = \frac{\mathrm{d}E_\nu}{\cos\theta \mathrm{d}A \mathrm{d}\omega \mathrm{d}t \mathrm{d}\nu}, \tag{4.1}$$

where dE_ν is energy spreading through solid angle dω during time dt in frequency interval dν. θ is an angle between a normal of the radiating surface and the direction from which the surface is observed (Gray 2005).

When light passes through a medium, its intensity may be affected, both weakened or strengthened. The change of the specific intensity dI_ν along path length s is defined as

$$\mathrm{d}I_\nu = -\kappa_\nu \rho I_\nu \mathrm{d}s + j_\nu \rho \mathrm{d}s, \tag{4.2}$$

where κ, ρ and j_ν are the mass absorption coefficient (in units of $\mathrm{m}^2\ \mathrm{kg}^{-1}$), density of the medium, and emission coefficient (in units of $\mathrm{J\ s^{-1}\ rad^{-2}\ Hz\ kg}$), respectively.

The radiative transfer equation (RTE) can be obtained by a simple division of Equation 4.2 with $\kappa_\nu \rho \mathrm{d}s = \mathrm{d}\tau_\nu$ and be written as

$$\frac{\mathrm{d}I_\nu}{\mathrm{d}\tau_\nu} = -I_\nu + \frac{j_\nu}{\kappa_\nu}, \tag{4.3}$$

where $\tau_\nu = \int_0^L \kappa_\nu \rho \mathrm{d}s$ is the dimensionless optical path and L is the geometrical path. The term $j_\nu/\kappa_\nu = S_\nu$ is usually called the *source function* and represents the specific intensity emitted in a hot gas.

The so-called *total absorption coefficient* or *opacity* χ_ν, which comprises both 'real' absorption κ_ν and scattering σ_ν, is defined as:

$$\chi_\nu = \kappa_\nu + \sigma_\nu. \tag{4.4}$$

For a solution of the RTE in a form of

$$I_\nu(\tau_\nu) = f e^{b\tau_\nu}, \tag{4.5}$$

where f is a function that will be determined later, the Equation 4.3 gives

$$bI_\nu + e^{b\tau_\nu}\frac{\mathrm{d}f}{\mathrm{d}\tau_\nu} = -I_\nu + S_\nu. \tag{4.6}$$

The first terms on both sides of Equation 4.6 are equal for $b = -1$, which after integration yields to

$$f = \int_0^{\tau_\nu} S_\nu e^{t_\nu} \mathrm{d}t_\nu + c_0, \tag{4.7}$$

where t_ν is a dummy variable and c_0 is a integration constant equal to $I_\nu(0)$.

The solution of Equation 4.3 is then

$$I_\nu(\tau_\nu) = \int_0^{\tau_\nu} S_\nu(t_\nu) e^{-(\tau_\nu - t_\nu)} \mathrm{d}t_\nu + I_\nu(0) e^{-\tau_\nu}. \tag{4.8}$$

Since geometry can play an important role in the study of the radiative transfer in solar

atmospheres, especially if the observed phenomena occurs closer to the limb, when using spherical geometry the ds in Equation 4.2 can be reformulated as dz, which is the direction towards to the observer. The term dI_ν/dz in spherical coordinates is defined as

$$\frac{\partial I_\nu}{\partial r}\frac{\mathrm{d}r}{\mathrm{d}z} + \frac{\partial I_\nu}{\partial \theta}\frac{\mathrm{d}\theta}{\mathrm{d}z}. \tag{4.9}$$

In the spherical geometry the following converting relations are valid:

$$\mathrm{d}r = \cos\theta \mathrm{d}z \tag{4.10}$$

$$r\mathrm{d}\theta = -\sin\theta \mathrm{d}z. \tag{4.11}$$

Using spherical coordinates Equation 4.3 can then be rewritten in a form of

$$\frac{\partial I_\nu}{\partial r}\frac{\cos\theta}{\kappa_\nu \rho} - \frac{\partial I_\nu}{\partial \theta}\frac{\sin\theta}{\kappa_\nu \rho r} = -I_\nu + S_\nu, \tag{4.12}$$

and further simplified when using the plane-parallel approximation that is suitable for most of the stellar atmospheres

$$\cos\theta \frac{\mathrm{d}I_\nu}{\mathrm{d}\tau_\nu} = I_\nu - S_\nu. \tag{4.13}$$

In this geometry a new variable *geometrical depth* d$x = -$dr is commonly used.

Thus, the solution of the RTE (Equation 4.8) can be written:

$$I_\nu(\tau_\nu) = -\int_c^{\tau_\nu} S_\nu(t_\nu) e^{-(t_\nu - \tau_\nu)\sec\theta} \sec\theta \, \mathrm{d}t_\nu \tag{4.14}$$

due to different boundary conditions.

4.1.1 Thermodynamic equilibrium

A system is in thermodynamic equilibrium (TE) if the quantities that characterise it are not functions of time or coordinates. In such a case the intensity depends solely on the

temperature and frequency, so the first term in the RTE (Equation 4.3) is equal to zero. In this case the intensity in RTE is usually labeled as

$$B_\nu(T) = I_\nu = \frac{j_\nu}{\kappa_\nu}, \tag{4.15}$$

where $B_\nu(T)$ is the Planck function that was defined in Equation 1.1. Equation 4.15 is then denoted as Kirchhoff's law.

Since the assumption of TE applied to the whole solar atmosphere is unrealistic, as radiation escapes from the atmosphere and can be detected, a concept of *local thermodynamic equilibrium* (LTE) may be applied in certain cases. In LTE it is assumed that Kirchhoff's law is valid locally, with different temperatures in different locations across the whole atmosphere (Mihalas 1978).

In the real atmosphere the level populations of the energy levels (required to calculate quantities like gas pressure, density, opacity, etc.) in all species depend on the radiation field, which may be very different from the Planck function. As the radiation field, in turn, depends on the level populations, their determination requires a self-consistent simultaneous solution of both. However, LTE is typically valid for the calculation of continuum, if the velocity distribution $f(\boldsymbol{v})$ of the recombining particles is Maxwellian:

$$f(\boldsymbol{v})\, dv_x\, dv_y\, dv_z = \left(\frac{m}{2\pi k_B T}\right)^{\frac{3}{2}} \exp[-m(v_x^2 - v_y^2 + v_z^2)/2k_B T]\, dv_x\, dv_y\, dv_z. \tag{4.16}$$

LTE can be a suitable approach when studying dense layers of the atmosphere where collisions dominate and the optical depth is large. In LTE the number of electron transitions from level m to l is equal to a number of transitions from level l to m (*detailed balance*, Hubeny 1997). The atomic levels n are populated according to the Boltzmann equation:

$$\left(\frac{n_{mjk}}{n_{ljk}}\right)^* = \left(\frac{g_{mjk}}{g_{ljk}}\right) \exp\left(-\frac{\chi_{mjk} - \chi_{ljk}}{kT}\right), \tag{4.17}$$

where * marks LTE, χ_{mjk} is an energy of level m of an element k in an ionisation state

j and g_{mjk} denotes its statistical weight.

Equation 4.17 can be generalised for free states, which yields the Saha ionisation equation:

$$n^*_{00k} = n^*_{01k} n^*_e \frac{1}{2} \left(\frac{h^2}{2\pi m k_B T} \right)^{3/2} \left(\frac{g_{00k}}{g_{01k}} \right) \exp\left(\frac{\chi_{I0k}}{k_B T} \right), \tag{4.18}$$

where n_e is a density of free electrons and χ_I is the ionisation potential.

4.1.2 Non-Local Thermodynamic Equilibrium

On a microscopic level in the non-LTE regime a milder condition is required: the number of all transitions to level i is equal to a number of all departures from level i. This condition is denoted as *statistical equilibrium* and can be mathematically written as

$$n_i \sum_{j \neq i} P_{ij} - \sum_{j \neq i} n_j P_{ji} = 0 \tag{4.19}$$

where P_{ij} is total rate of transitions from level i to level j.

Since it is needed to distinguish between several types of transitions, for transitions between two bound states (depicted in Figure 4.1), the Equation 4.19 shall be rewritten as

$$n_j (A_{ji} + B_{ji} \bar{J}_{ij}) - n_i B_{ij} \bar{J}_{ij} = n_j A_{ji} Z_{ji}, \tag{4.20}$$

where A_{ji}, B_{ji} and B_{ij} are spontaneous emission rate, stimulated emission rate and absorption rate, respectively, Z is the so-called *net radiative bracket* or *escape coefficient* and $\bar{J}$ is the mean intensity (intensity I integrated over all solid angles and divided by 4π). A and B are also known as *Einstein coefficients*.

In LTE the detailed balance yields the equation

$$n_i B_{ij} \bar{J} = n_j A_{ji} + n_j B_{ji} \bar{J}, \tag{4.21}$$

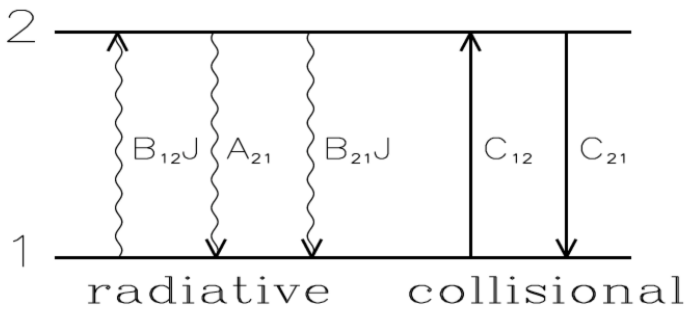

Figure 4.1: Notation for radiative and collisional transition rates between two energy levels in an atom. Reproduced from Hubeny (1997).

where $\bar{J}$ can be expressed as

$$\bar{J} = \frac{A_{ji}/B_{ji}}{(n_i/n_j)(B_{ij}/B_{ji})}. \tag{4.22}$$

When using the Boltzmann equation (4.17) and replacing the difference of the considered energy levels with an energy of an absorbed/radiated photon during a transition, the following expression can be obtained (Rybicki & Lightman 1986):

$$\bar{J} = \frac{A_{ji}/B_{ji}}{(g_i B_{ij}/g_j B_{ji})\exp(h\nu_0/k_B T) - 1}. \tag{4.23}$$

Using the Planck function (Equation 1.1) instead of $\bar{J}$ yields to

$$g_i B_{ij} = g_j B_{ji} \tag{4.24}$$

$$A_{ji} = \frac{2h\nu^3}{c^2} B_{ji}, \tag{4.25}$$

that are general expressions, since they are functions of the physical properties of the atoms and constants only.

According to Hubeny & Mihalas (2014), the relations between absorption and emis-

sion coefficients, respectively, and Einstein coefficients are given by

$$\kappa_{\nu_0} = \frac{h\nu_0}{4\pi}(n_i B_{ij} - n_j B_{ji})\varphi(\nu) \tag{4.26}$$

$$j_{\nu_0} = \frac{h\nu_0}{4\pi} n_j A_{ji}\varphi(\nu), \tag{4.27}$$

where ν_0 is a line centre frequency and $\varphi(\nu)$ is an absorption line profile.

The absorption profile is usually prescribed as a convolution of a Doppler profile given by the thermal motion of the radiators, and a Lorentz profile given by the intrinsic line broadening (for example Stark broadening). The convolved profile $\varphi(x) = H(a,x)/\sqrt{\pi}$ is better expressed using a dimensionless frequency $x = (\nu - \nu_0)/\Delta\nu_D$, where the Doppler width is defined as

$$\Delta\nu_D = \frac{\nu_0}{c} v_{th}, \tag{4.28}$$

and the Voigt function as

$$H(a,x) = \frac{a}{\pi}\int_{-\infty}^{\infty} \frac{\mathrm{e}^{-y^2}}{(x-y)^2 + a^2}\,\mathrm{d}y. \tag{4.29}$$

$v_{th} = \sqrt{2kT/m}$ in Equation 4.28 denotes thermal velocity, $a = \Gamma/(4\pi\Delta\nu_D)$ in Equation 4.29 denotes the damping parameter and Γ is the atomic damping parameter.

From a general definition of source function, Equations 4.26 and 4.27 and relations between Einstein coefficients (Equations 4.24 and 4.25), the source function in the line can be obtained, if absorption and emission profiles $\varphi(\nu)$ are identical:

$$S^L = \frac{j_\nu}{\kappa_\nu} = \frac{n_j A_{ji}}{n_i B_{ij} - n_j B_{ij}} = \frac{2h\nu^3}{c^2}\left(\frac{g_j n_i}{g_i n_j} - 1\right). \tag{4.30}$$

Such a condition is fulfilled under the assumption of *complete redistribution* (CRD), which means that photons absorbed by atoms in processes of stimulated emission and absorption are uncorrelated in frequency with photons (re)emitted by the same atoms

in processes of both stimulated and spontaneous emissions.

However, in the process of stimulated emission the produced photon is identical with the incident photon, so if stimulated emission plays a role in line formation, such a line cannot be calculated with CRD and *partial redistribution* (PRD) has to be considered. PRD is typically needed to reproduce wings of strong resonance lines like Lyman α or Ca II K&H (Mihalas 1978; Hubeny 1985).

In PRD the emission coefficient (Equation 4.27) contains its own emission profile $\psi(\nu)$ that differs from the absorption profile used in CRD (Hubeny 1985):

$$\psi(\nu, n) = \varphi_\nu + \frac{n_i B_{ij}}{n_j P_j} \varphi_\nu [\bar{\mathcal{R}}(\nu, n) - \bar{J}] \tag{4.31}$$

where

$$\bar{\mathcal{R}}(\nu, n) = \frac{1}{4\pi\varphi_\nu} \iint R(\nu', n, \nu, n) I(\nu', n) \, \mathrm{d}\nu' \, \mathrm{d}\Omega, \tag{4.32}$$

R is a velocity-averaged redistribution function for the transition chain $i \rightarrow j \rightarrow i$ and P_j is a sum of all departure rates from j level, both radiative and collisional.

4.1.3 Continuum absorption coefficient

The observed continuum is a combination of several radiative processes. Some of them have already been mentioned in Section 1.3.1. Since hydrogen is the most abundant element in solar atmosphere, it plays the most important role in continuum formation.

The atomic absorption coefficient for bound-free transitions in neutral hydrogen is defined by the Kramers' formula (Kramers 1923; Gaunt 1930):

$$\alpha_{\mathrm{bf}}(H) = \frac{32}{3^{3/2}} \frac{\pi^2 e^6}{h^3} \frac{R}{n^5 \nu^3} g_{bf}, \tag{4.33}$$

where $R = 1.0968 \times 10^7 \ \mathrm{m}^{-1}$ is Rydberg constant for hydrogen (Gray 2005), e is the electron charge, n is the energy level of electron and g_{bf} is the Gaunt's correction

derived from quantum theory. For the first five levels the relation between $\alpha_{\mathrm{bf}}(H)$ and wavelength is shown in Figure 4.2.

The total absorption κ due to bound-free transitions is then a sum over all transitions:

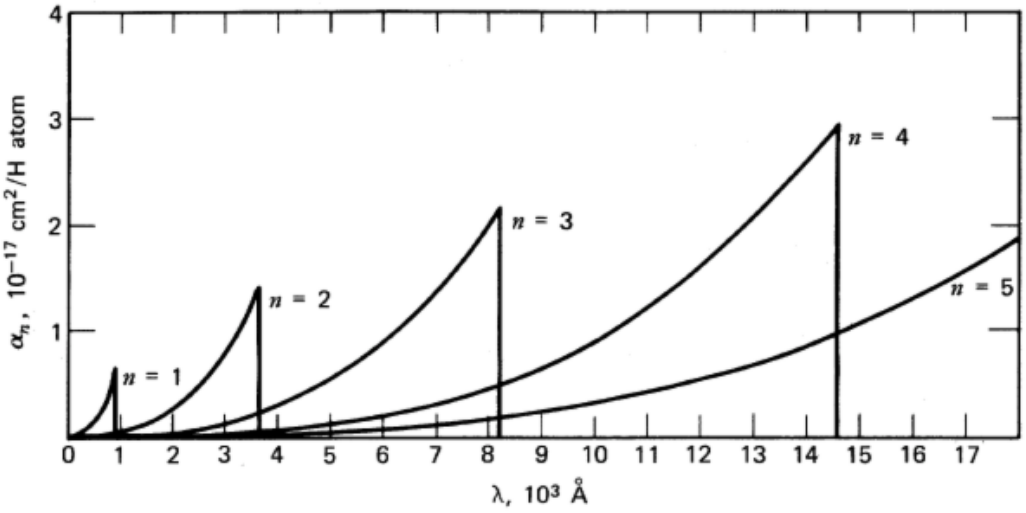

Figure 4.2: Absorption coefficient for bound-free transitions in neutral hydrogen atom. Reproduced from Rutten (2003).

$$\kappa(H_{\mathrm{bf}}) = \sum_{n=1}^{\infty} \frac{\alpha_{\mathrm{bf}}(H) N_n}{N} = \sum_{n=1}^{\infty} \frac{32}{3^{3/2}} \frac{\pi^2 e^6}{h^3} \frac{R}{n^5 \nu^3} g_{\mathrm{bf}} \frac{N_n}{N}, \tag{4.34}$$

where

$$\frac{N_n}{N} = \frac{g_n}{u_0(T)} \exp(-\chi / k_B T) \tag{4.35}$$

is a fraction of hydrogen atoms excited to level n, $g_n = 2n^2$ is the statistical weight and $u_0(T) = 2$ is the partition function. After simplification and substitution the absorption can be written as

$$\kappa(H_{\mathrm{bf}}) = \alpha_0 \sum_{n=1}^{\infty} \frac{c^3}{n^3 \nu^3} g_{\mathrm{bf}} \exp(-\chi / k_B T), \tag{4.36}$$

where α_0 represents constants.

Free-free absorption depends on the velocity of the incident electron. When assuming the Maxwell-Boltzmann velocity distribution of electrons, the atomic absorption

coefficient is

$$\alpha_{\rm ff}(H) = \frac{2h^2e^2R}{3^{3/2}\pi m^3\nu^3}\int_0^\infty \sqrt{\frac{2m^3}{\pi k_B^3 T^3}}\nu e^{-\frac{m\nu^2}{k_B T}}\,{\rm d}\nu = \frac{2h^2e^2R}{3^{3/2}\pi m^3\nu^3}\sqrt{\frac{2m}{\pi k_B T}}. \tag{4.37}$$

The absorption coefficient will be

$$\kappa(H_{\rm ff}) = \frac{\alpha_{\rm ff}(H) g_{\rm ff} N_i N_e}{N_0}, \tag{4.38}$$

where N_i, N_e and N_0 are number densities of protons, electrons and neutral hydrogen atoms, respectively.

The negative hydrogen ion is created when a free electron (usually from ionized metals) is captured by neutral hydrogen. The bound energy of the extra electron is weak compared to the bound energy in neutral hydrogen (0.755 eV vs. 13.6 eV) and contributes significantly to absorption at temperatures close to those in the solar photosphere. The bound-free absorption coefficient reaches a maximum near 850 nm and can be well approximated using a sixth-order polynomial (Figure 4.3).

Free-free transitions of H^- become important at the infrared part of the spectrum, and are not so relevant to this work.

4.2 The RADYN code

The RADYN code uses a 1D model of the solar/stellar atmosphere where the dimension, along which the computation is performed, is the height above the photosphere or, when modelling a flare, a coordinate along a magnetic half-loop between the reconnection point and the base of the photosphere. RADYN is based on the MULTI package (Scharmer 1981; Scharmer & Carlsson 1985; Carlsson 1986, 1998), which includes RTE in non-LTE. The code employs an adaptive grid (Dorfi & Drury 1987) to be able to simulate shocks and steep gradients of the atmospheric quantities.

Hydrogen is simplified to a six-level atom, helium to a nine-level atom, Ca II to

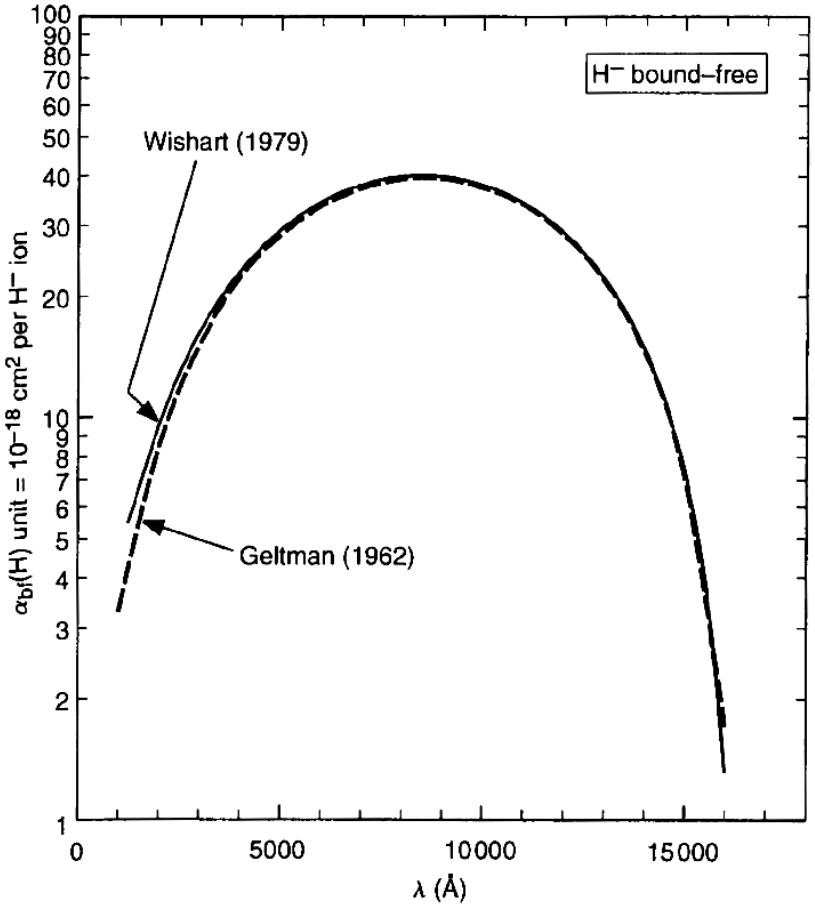

Figure 4.3: Absorption coefficient of bound-free transition in negative hydrogen ion. Reproduced from Gray (2005).

a six-level ion and Mg II to a four-level ion, all with continua. In total 24 bound-bound and 22 bound-free transitions are included. Other transitions are included in LTE background opacity.

The hydrodynamic part of the code comprises the equation of motion

$$\frac{\partial \rho v}{\partial t} + \frac{\partial \rho v^2}{\partial z} + \frac{\partial}{\partial z}(p + q_v) + \rho g - A_{beam} = 0, \tag{4.39}$$

continuity equation

$$\frac{\partial \rho}{\partial t} + \frac{\partial \rho v}{\partial z} = 0 \tag{4.40}$$

and equation of internal energy conservation

$$\frac{\partial \rho e}{\partial t} + \frac{\partial \rho v e}{\partial z} + (p + q_v)\frac{\partial v}{\partial z} + \frac{\partial (F_c + F_r)}{\partial z} - Q_{cor} - Q_{beam} - Q_{rc} = 0, \tag{4.41}$$

where z, ρ, t, p, v, e and g denote height, density, time, pressure, velocity, internal energy per unit mass and gravity acceleration, respectively (Allred et al. 2015). Q_{cor}, Q_{beam}, Q_{rc} and A_{beam} represent the heating sources required to sustain the hot corona against the radiative losses, non-thermal electron beam heating due to collisions and return current, and momentum deposition, respectively. q_v is a viscous stress to improve the numerical stability of the calculations. Equations of mass, momentum, charge and population conservation are also included. The equations are solved with the Newton-Raphson method (Ben-Israel 1966).

The code has been improved several times since it was first introduced in order to employ all processes that affect line profiles and continua levels. As described by Allred (2005), the radiative hydrodynamics code includes the calculation of photoionisation heating resulting from high temperatures, soft X-ray emitting regions, as well as the calculation of optically-thin cooling due to thermal bremsstrahlung and collisionally excited metal transitions. An adjustment in the calculation of the conductive flux has also been taken into account in order to avoid unphysically large values in the transition region - where temperature gradients are large. Hydrodynamic effects due to gravity, thermal conduction, and compressional viscosity are included (Abbett & Hawley 1999b).

The version of RADYN introduced by Allred et al. (2015) was adapted to study processes most important to flare dynamics in general stellar atmospheres. Since the model allows the study of the propagation of single-type particles (usually electrons or protons), return current needs to be considered because it changes the particle spectrum and heats the surrounding plasma (van den Oord 1990; Zharkova & Gordovskyy 2006; Holman 2012). A distribution function of the beam is determined by a solution of the Fokker-Planck equation (McTiernan & Petrosian 1990) that includes relativistic

effects, Coulomb collisions, synchrotron emission, pitch angle scattering and magnetic field gradients.

XEUV backwarming plays an important role in the heating of the chromosphere. Unlike previous versions of RADYN, Allred et al. (2015) added photoionizations as a consequence of backwarming, which significantly affects the profiles of lines formed in the chromosphere.

4.3 The RH code

When calculating the strong lines of H, He and Ca in the non-LTE regime and lines of other elements in LTE, RADYN uses CRD to simplify the computation. However, that approach can significantly overestimate the radiative losses in strong resonance lines, as shown in the case of Mg II k or Ca II H&K (Ulmschneider et al. 1987; Uitenbroek 2002) and lead to the incorrect temperature structure of the atmosphere.

The RH code provides an efficient tool to incorporate PRD effects in the flaring atmosphere. It is based on a *multilevel accelerated lambda iteration* method (MALI) introduced by Rybicki & Hummer (1991, 1992). RH allows the calculation of accurate line profiles with PRD even when various transitions (both bound-bound and bound-free) overlap in wavelength. The code requires pre-conditioning of the occupation numbers that can be obtained from RADYN.

A unified theory of electric pressure broadening (Vidal et al. 1970, 1971, 1973) was introduced into the RH hydrogen atom model by Kowalski et al. (2017) which allowed them to accurately reproduce the flare Balmer line widths as well as the spectrum of Vega (spectral class A0). The theory describes perturbations from slowly moving protons and fast moving electrons and makes use of line profile as a function of temperature and electron density for transitions among 22 levels in the hydrogen atom (Tremblay & Bergeron 2009).

4.4 Contribution function

One of the key questions of this work is: Where does the WL excess emission originate? In order to help answer this question the models are able to calculate the so-called *contribution function* defined by Carlsson & Stein (1997) as

$$I_\nu = \int_{z_0}^{z_1} S_\nu \mathrm{e}^{-\tau_\nu} \chi_\nu \mathrm{d}z = \int_{z_0}^{z_1} S_\nu \, \tau_\nu \mathrm{e}^{-\tau_\nu} \frac{\chi_\nu}{\tau_\nu} \, \mathrm{d}z, \tag{4.42}$$

that is convenient to break into three components, especially when studying line formation:

- Source function $S = \eta/\chi$ (bottom left panel in Figure 4.4), that for a given transition does not depend on wavelength in CRD
- $\tau_\nu \mathrm{e}^{-\tau_\nu}$ (upper right panel in Figure 4.4), that is high at the optical unity
- $\chi_\nu/\tau_\nu = \sum_i n_i \sigma_{\nu i}/\tau_\nu$ (upper left panel in Figure 4.4), that is high where there are many emitting particles at small optical depth

In PRD the contribution function can be calculated for continuum (Figure 6.5).

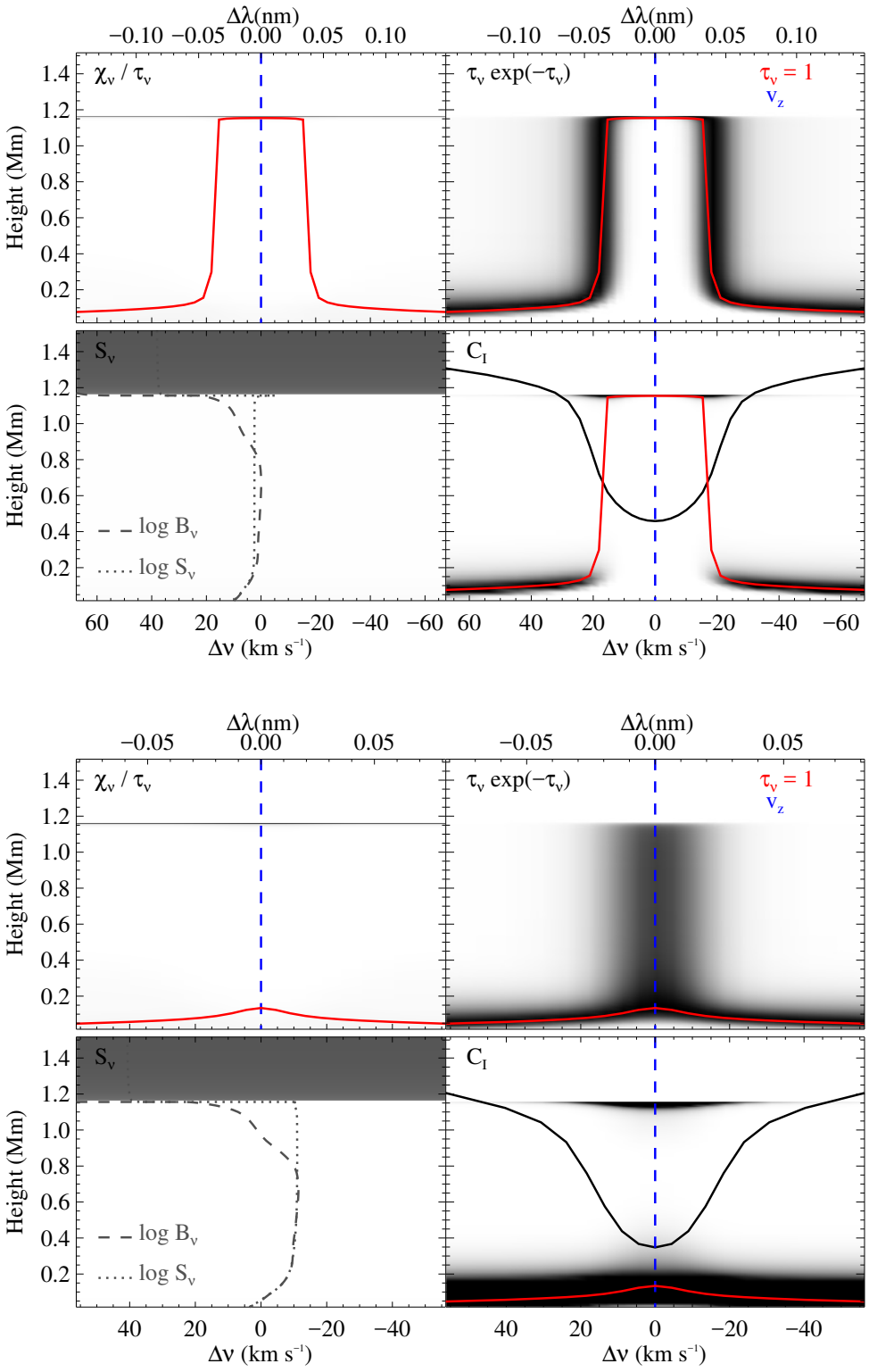

Figure 4.4: Contribution functions (marked as shadows) of Hα (upper panel) and Hγ (lower panel) lines in the quiet atmosphere. Darker shades represent areas with a higher contribution. The red lines marking the surface of optical unity show that the Hα core originates purely in the top chromosphere, meanwhile the Hγ core is formed through a broad range of heights with the major contribution from the photosphere. The total contribution function in the lower right window of both panels composes of the components in the other three windows, as described in Equation 4.42.

Chapter 5

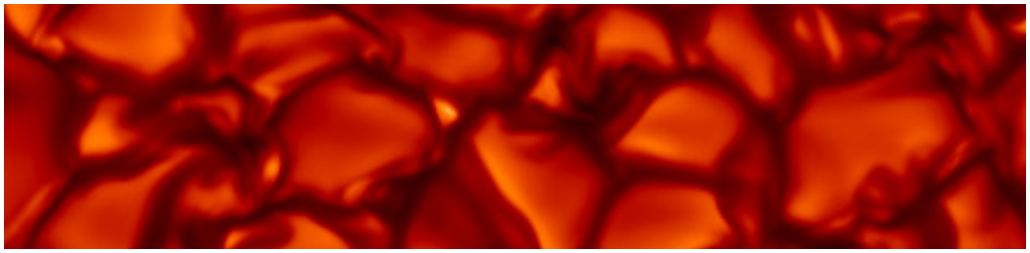

RADYN model atmospheres

Life will only change

when you become

more committed

to your dreams

than your comfort zone.

This chapter explains the selection of the initial atmosphere and the type of the particle beam (where applicable) used in the electron and proton beams models. It also shows the effect of the return current and describes the attempts to explore a broader parameter space without the RHESSI/Fermi constraints in order to reproduce some of the observed spectral characteristics. Since the absence of Balmer emission in WLFs is not commonly observed, it was first necessary to find out how the WL signatures can be reproduced simultaneously with the suppressed emission in the higher order Balmer lines.

Along with the theories mentioned in Section 1.3.2, the deep heating scenario was explored. A heating rate between 1000 and 8000 erg cm^{-3} s^{-1} was applied at heights from 300 to 933 km above the photospheric floor, and the response in the Hγ line was studied. This scenario showed a better agreement with the observed continuum and line profiles than for a typical flare electron beams. The same spectral signatures were reproduced with both the electron and proton beams of a flux that is typically detected in X1-class flares. However, the required E_C had to be unrealistically high.

5.1 Initial atmosphere

The starting point for the modelling work is the selection of the initial atmosphere. The atmosphere that describes well the conditions on the quiet Sun (denoted QS.SL.LT in Allred et al. 2015) has the transition region placed $\sim$ 1600 km above the photospheric floor, and the chromosphere stretches down to a height of $\sim$ 1000 km. The top of the corona reaches temperature of 1 MK and the electron density of 6×10^8 cm^{-3} (Figure 5.1). However, this is not the best atmosphere that describes the conditions in an active region.

Instead an atmosphere with a transition region shifted towards a higher column mass and with a hotter corona was used in this work, as it better describes the atmospheric conditions in an active region (denoted QS.SL.HT in Allred et al. 2015). The transition region is placed at a height of $\sim$ 1300 km above the photosphere, the temperature at

$\tau_{500nm} = 1$ and in corona equals to 5800 K and 3 MK, respectively. The atmospheric temperature and density profiles are marked with the dashed line in Figure 5.1.

The flaring loop had a half-length of 10 Mm, a constant cross-sectional area and an apex density of 10^{10} cm^{-3}. The pitch angle distribution of the injected electrons was Gaussian centred around the loop axis and with half width half max of 23.5 degree. The magnetic field strength decreased exponentially from 1000 G in the footpoints to 100 G at the loop top. This allowed the inclusion of the effect of magnetic mirroring and synchrotron emission from the non-thermal particles.

5.2 Description of the particle beams

The classical theory of collisional interaction of a beam with a hydrogen target can be used to model the interaction of electrons and protons with the solar atmosphere during flares (Emslie 1978). The energy losses of the descending beam consisting of particles with mass m due to the Coulomb collisions with both the charged and neutral targets can be expressed as:

$$\frac{\mathrm{d}E}{\mathrm{d}t} = \left(\frac{\mathrm{d}E}{\mathrm{d}t}\right)_i + \left(\frac{\mathrm{d}E}{\mathrm{d}t}\right)_n = -\frac{2\pi e^4}{E}\left[x\Lambda\left(\frac{m}{m_p} + \frac{m}{m_e}\right) + (1-x)\Lambda'\frac{m}{m_e}\right]nv, \tag{5.1}$$

where x is the degree of ionization, Λ is the Coulomb logarithm, Λ' is the effective Coulomb logarithm, and i, n, e and p are indices representing ions, neutral atoms, electrons and protons, respectively.

Then the energy losses must be convolved with the injected energy spectrum of the beam:

$$I_B(N,t) = Kn\gamma \int_{E_0} \frac{F_0(E_0,t)\mathrm{d}E_0}{E_0[1-(2+\beta/2)(\gamma KM/\mu_0 E_0^2)]^{(2+\beta)/(4+\beta)}}, \tag{5.2}$$

where N is the column density of the target, F_0 is the beam flux, $K = 2\pi e^4$ is a constant,

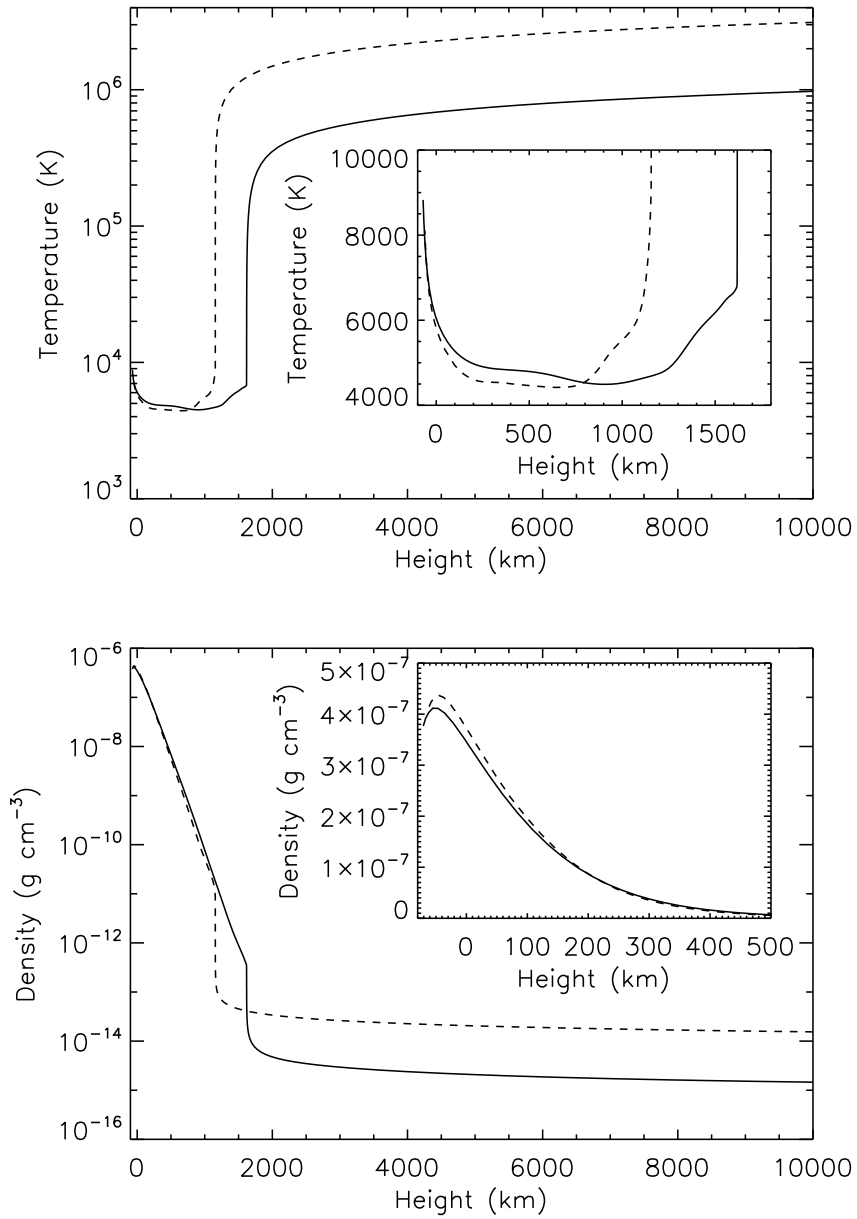

Figure 5.1: Temperature (upper panel) and density (lower panel) profiles of the VAL-C atmosphere (solid line) and the active region-like atmosphere (QS.SL.LT and QS.SL.HT, respectively, from Allred et al. 2015, dashed line).

n is the target particle number density, β and γ are constants depending of the target and beam types, and μ_0 is the velocity direction cosine (pitch angle).

The more advanced solution of energy losses of the particle beam is based on the solution of the kinetic equation for the electron or proton distribution (Fokker-Planck equation, McTiernan & Petrosian 1990):

$$\mu\frac{\partial\Phi}{\partial s}-\frac{\mathrm{d}\ln B}{2\mathrm{d}s}\frac{\partial}{\partial\mu}[(1-\mu^2)\Phi]= \\ \frac{1}{\beta^2}\frac{\partial}{\partial E}\{[C+S\beta^3\gamma^2(1-\mu^2)]\Phi\}-\frac{S}{\beta\gamma}\frac{\partial}{\partial\mu}[\mu(1-\mu^2)\Phi] \\ +\frac{C\xi}{\beta^4\gamma^2}\frac{\partial}{\partial\mu}\left[(1-\mu^2)\frac{\partial\Phi}{\partial\mu}\right]+\frac{\Sigma}{c\beta^2}, \tag{5.3}$$

where $\Phi = F_0/\beta$, $\gamma = E + 1$ is the total energy, $\beta c = c(1 - 1/\gamma^2)^{1/2}$ is the relativistic electron velocity, B is the magnetic field strength, Σ is a source term for the injected electrons, C and S are the collision and synchrotron coefficients, respectively, and $C\xi$ measures the pitch angle diffusion from collisions.

Figure 5.2 compares the atmospheric temperature profiles altered by both types of electron beams. The comparison demonstrates that the divergence between both types of beam becomes more pronounced with increasing the amount of energy carried by the beams. All three examples show that the beam introduced by McTiernan & Petrosian (1990) delivers its energy earlier and in greater extent, which is especially obvious in the chromosphere. This result is expected, since this beam incorporates more energy loss mechanisms than the Emslie beam which includes only the Coulomb collisions. Figure 5.2 also shows a discontinuity in the temperature derivation for some of the atmospheric temperature profiles that may not be realistic. For all the above mentioned reasons the McTiernan beam profile is used hereafter.

5.3 The effect of a return current

Return current is a well studied effect that breaks the particle beam down when propagating through the atmosphere. It is induced when the charge motion due to the particles acceleration is not compensated by the acceleration of particles of the opposite charge. This is especially significant in models with beams composing of a single type of particles.

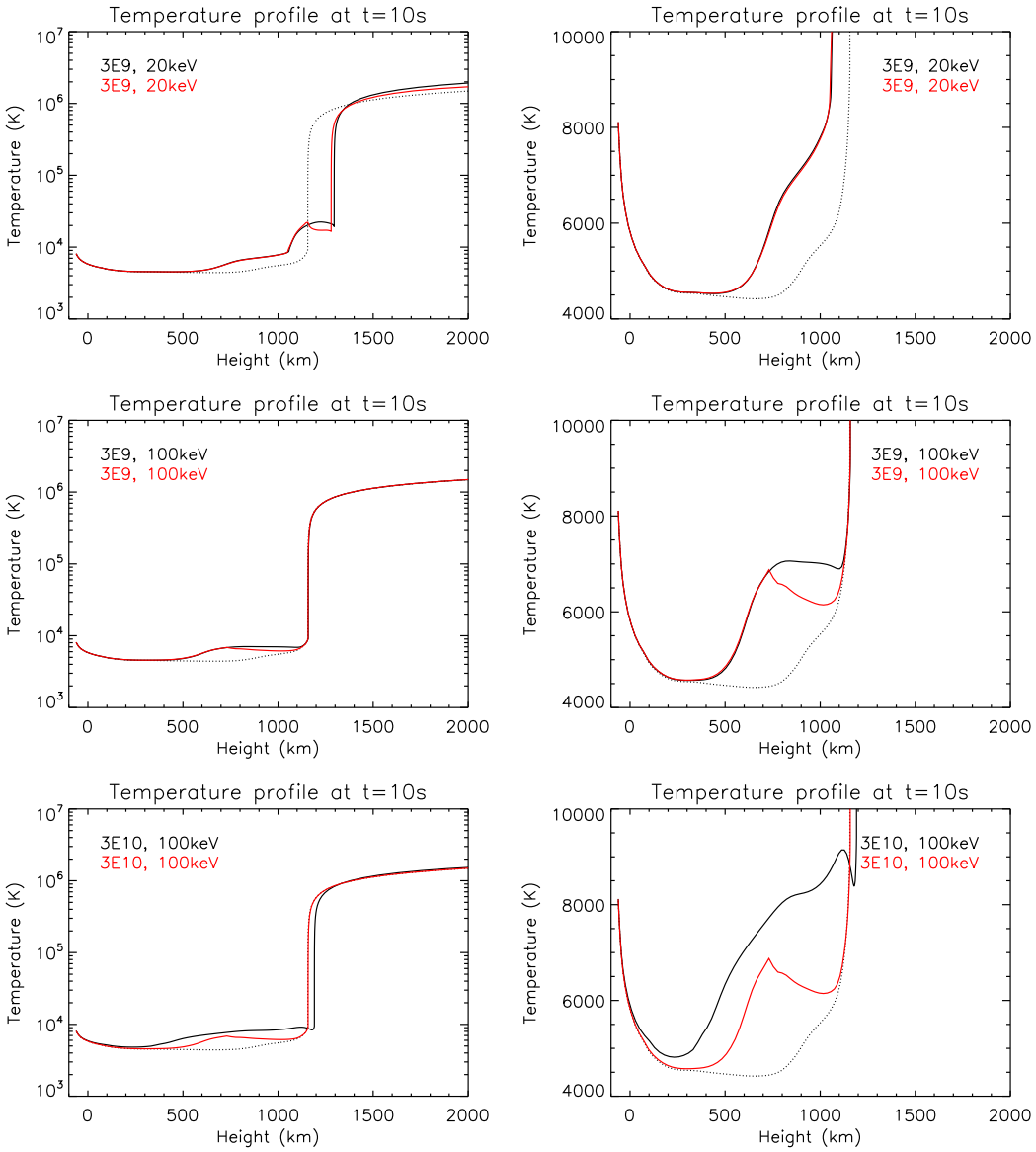

Figure 5.2: A comparison of the temperature profiles after the application of electron beams defined by McTiernan & Petrosian (1990) (black) and Emslie (1978) (red). The legend shows the beam flux in units of erg cm^{-2} s^{-1} and the E_C. The dotted line marks the initial temperature profile.

The return current causes additional heating in corona. The volumetric heating term Q_{rc} in Equation 4.41 due to the return current induced by the electron beam with the power-law distribution is described by Holman (2012) as:

$$Q_{rc} = \begin{cases} \eta e^2 F_e^2 & x < x_{rc} \\ \eta e^2 F_e^2 \left(\delta \frac{E_{therm}}{E_C} + \frac{V(x)}{E_C}\right)\left(\frac{E_{therm}}{E_C} + \frac{V(x)}{E_C}\right)^{1-2\delta} & x \geq x_{rc} \end{cases} \tag{5.4}$$

where F_e, δ and E_C are the initial beam parameters (beam flux, power-law index and low energy cutoff, respectively), η is the classical Spitzer resistivity, and $V(x)$ is the electric potential energy. The electrons are thermalised and removed from the beam when their energy is E_{therm} = 2.5 k_BT. The x coordinate is the distance from the loop top and x_{rc} is the distance where the lowest energy electrons are thermalized.

The effect of the return current on the spectral output was investigated. Figure 5.3 shows that the return current is significant only for the electron beams and becomes more important for beams with higher energy flux. The line core is usually the most affected, but if the beam flux is high enough to elevate the continuum level, this is also reduced. Figure 5.4 shows that in the electron beam-driven models with the return current, the temperature across the whole atmosphere is lower compared to the models without the return current. It is not surprising, since the return current removes some of the electrons from the beam, as it propagates through the atmosphere, and consequently its energy deposited into the atmosphere is lower. The proton beam-driven models do not show any significant influence of the return current. In order to obtain the most realistic synthetic spectra, the return current was incorporated in all the beam-driven models hereafter.

5.4 Attempts to reproduce the flare spectral signatures

This section describes the attempts to reproduce the WL excess together with the suppression of the higher order Balmer lines. Along with the theory described in Section 1.3.2, the deep heating scenario was investigated together with attempts to deliver the necessary energy into the deep layers with the particle beams. In this section the energy constraints yielding from the analysis of X-ray observations are not considered.

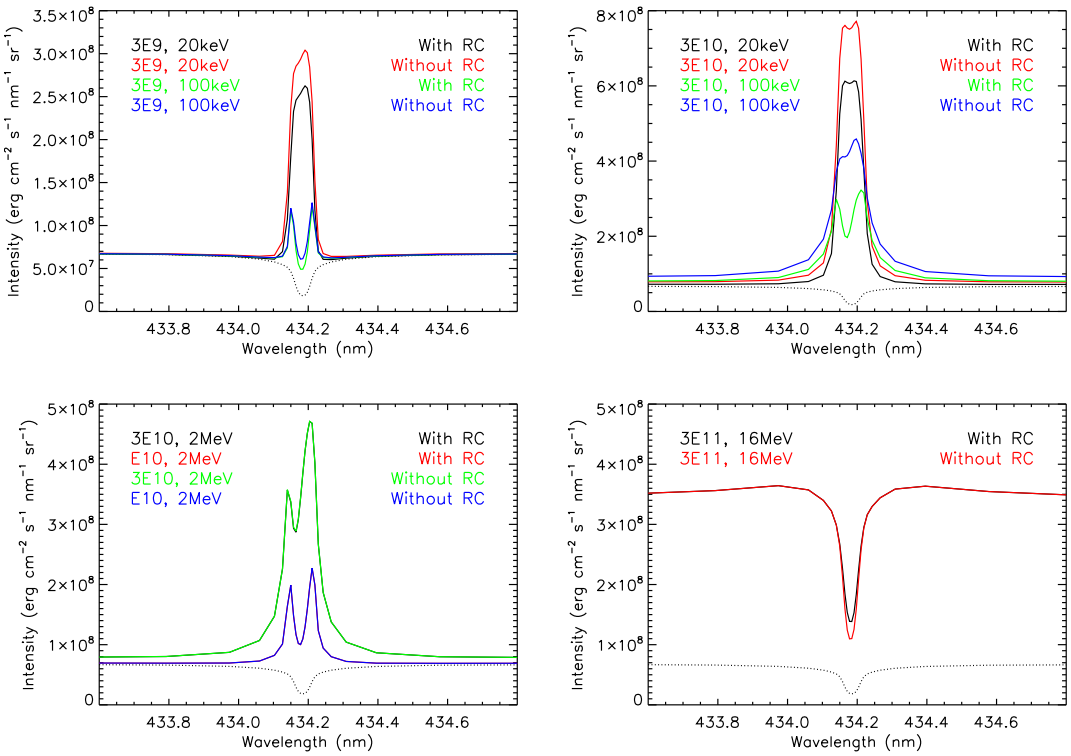

Figure 5.3: The effect of the return current (RC) on the Hγ line profiles. The upper and lower figures show the output of the electron and proton beam-driven models, respectively. The legend shows the beam flux in the units of erg cm^{-2} s^{-1} and E_C. The dotted line marks the initial line profile.

5.4.1 Beam heating versus direct energy deposition

In the first experiment the same energy was deposited into the atmosphere (i) using a standard electron beam and (ii) by deposition directly into the TMR. The electron beam had the following parameters:

- Constant flux of 3.5×10^{11} erg cm^{-2} s^{-1}
- $E_C = 20$ keV
- $\delta = 3$
- Duration = 10 s

The hard electron spectrum was chosen based on initial RHESSI X-ray estimates, the other parameters meet the expected values for an X-class flare (Kennedy et al. 2015;

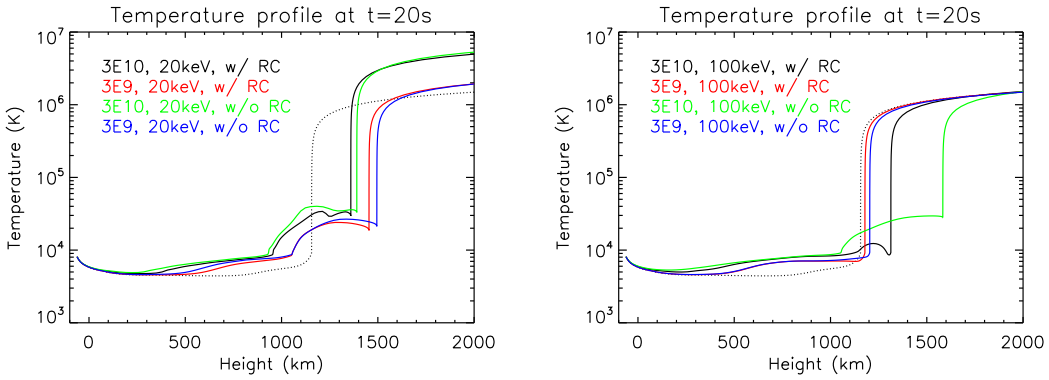

Figure 5.4: The effect of the return current (RC) on the atmospheric temperature profiles in the electron beam-driven simulations. The legend shows the beam flux in the units of erg cm^{-2} s^{-1} and E_C. The dotted line marks the initial temperature profile.

Rubio da Costa et al. 2016).

The synthetic spectra in Figure 5.5 show that an electron beam with standard flare parameters triggers strong emission in the Balmer lines and Ca II H&K lines. In contrast, the energy applied to the TMR (< 600 km above photospheric floor) triggers an emission in the line wings only with a deep central reversal. In this scenario, significant energy is emitted in the continuum. However, the emission in the Balmer free-bound continuum is at the same level in both cases.

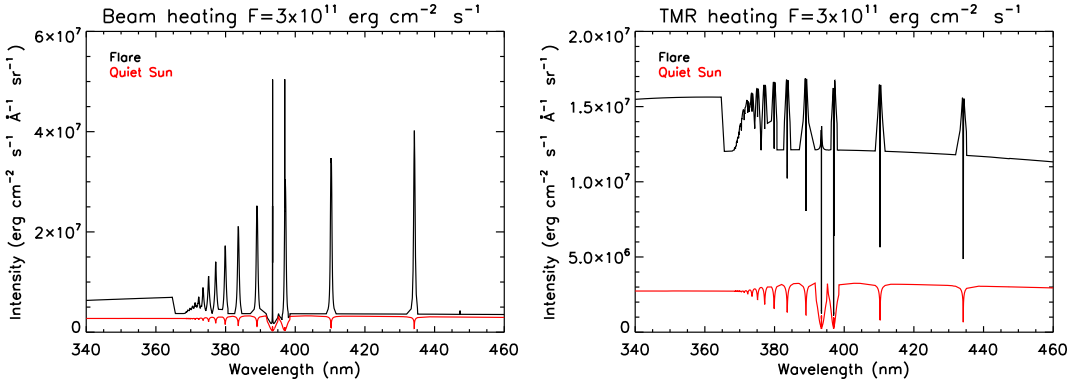

Figure 5.5: Synthetic spectra showing the difference between the standard electron beam heating and direct heating in the TMR.

In order to compare the synthetic spectra with the observations, the filling factor has to be considered since the flaring kernels were small compared to the size of the IS's aperture. Therefore most of the flux detected by the IS came from the non-flaring

(quiet) atmosphere. To emulate the observed spectra, both the flaring and quiet synthetic spectra must be combined as:

$$F_{synthetic} = \frac{F_{flare} * ff + F_{non-flare} * (1 - ff) - F_{non-flare}}{F_{non-flare}}. \tag{5.5}$$

where ff is the filling factor. $F_{non-flare}$ stands for spectrum taken at the beginning of the simulation.

The IS emulated spectra in Figure 5.6 show that in both scenarios the lines were clearly distinguishable, but if the upper chromosphere was bypassed and the energy delivered directly into the TMR, the Balmer lines would be significantly suppressed. Instead the continuum would be increased by $\sim$ 10 and 20% for filling factors 0.04 and 0.07, respectively. On top of that, the Balmer free-bound continuum would add up to 10% in the flare excess in both scenarios. Ca II H&K line cores would show at least a 200% increase.

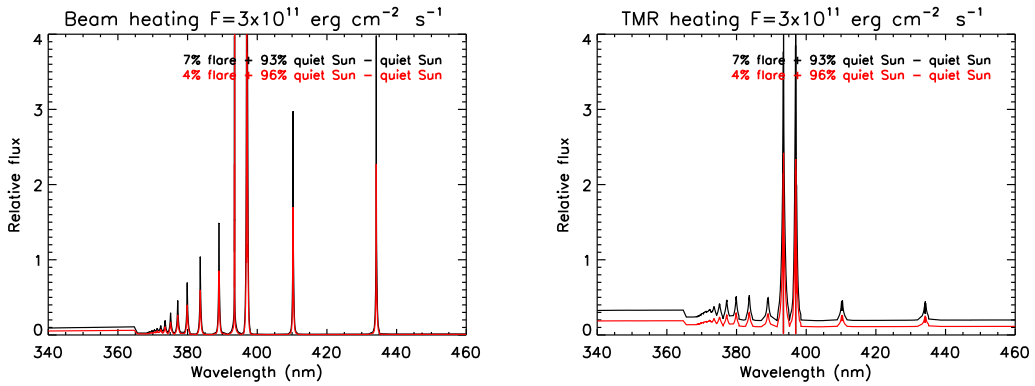

Figure 5.6: Relative flare excess consisting of quiet and flaring contribution for beam heating and TMR direct heating. For filling factor see legend.

The difference between the atmospheric structure in both models is demonstrated in Figure 5.7 showing that the standard electron beam delivers its energy at the top of the chromosphere, moves the transition region to lower geometrical heights and leads to a temperature increase in the corona of over 10 MK. In contrast, the deep heating model leaves the upper chromosphere and corona undisturbed and shows an increase of

temperature in heights where the heating has been applied. This finding suggests that the massive increase of continua (right panel of Figure 5.5) on both sides of the Balmer jump must be associated with the increase of temperature in the (upper) photosphere or/and the lower chromosphere.

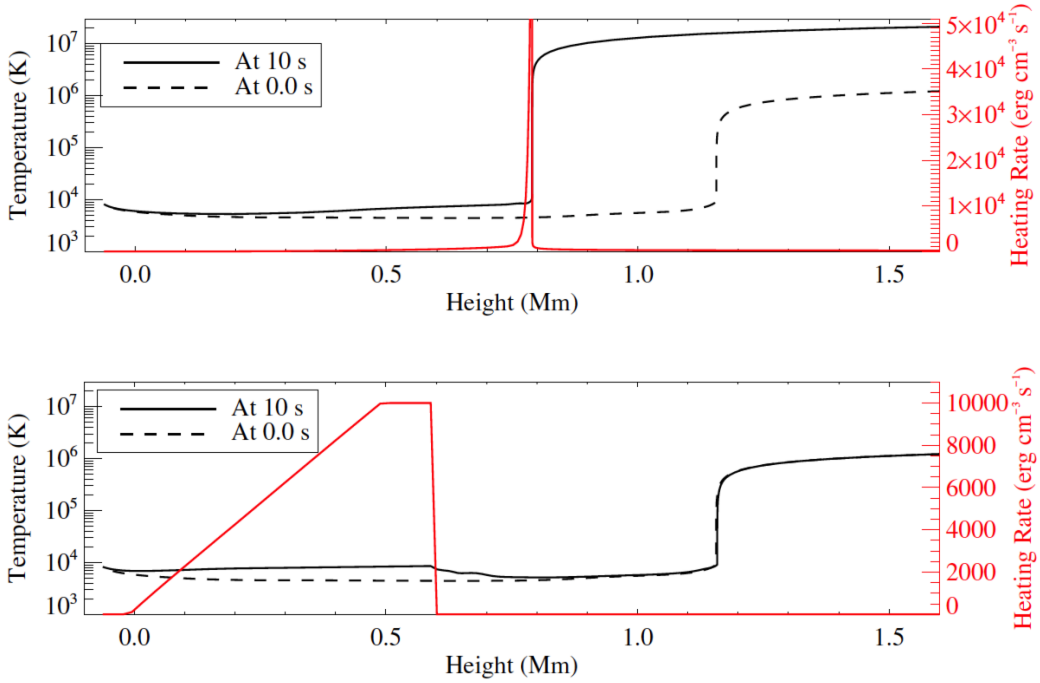

Figure 5.7: Temperature profile of the atmosphere 10 s into the simulation for a model with F = 3.5×10^{11} erg cm^{-2} s^{-1}, E_C = 20 keV, δ = 3 electron beam (upper plot) and direct heating (lower plot).

Since it is clear that the model with the deep heating is qualitatively more similar to the observations described in Section 3.3, a broader parameter space was explored in order to find similarities with the observed line profiles. Simulations of energy deposition at various heights around the TMR were performed. They should mimic the effect of a particle beam that leaves the upper chromosphere undisturbed. The sample heating function is plotted in Figure 5.8. In the models the lower boundary of heating was at 600, 500, 400 and 300 km above the photospheric floor and the peak heating rate was 1000, 2000, 4000 and 8000 erg cm^{-3} s^{-1}. The heating function then linearly dropped to zero at 933 km above the photospheric floor. Table 5.1 summarises all models with

the direct heating and presents the equivalent flux of particle beams.

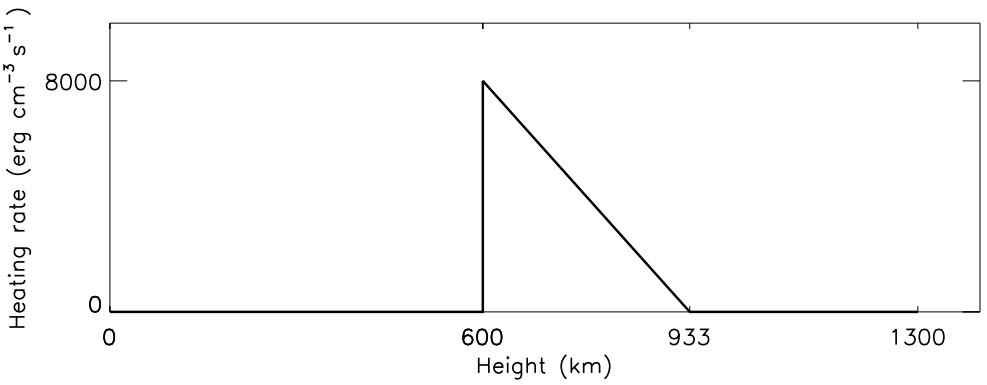

Figure 5.8: Sample heating function with a lower boundary of heating at 600 km and peak of heating function of 8000 erg cm^{-3} s^{-1} that emulates a beam with a flux of 1.3×10^{11} erg cm^{-2} s^{-1}.

Lower boundary of heating (km)	Peak heating rate (erg cm^{-3} s^{-1})	Equivalent beam flux (erg cm^{-2} s^{-1})
600	1000	1.67×10^{10}
600	2000	3.33×10^{10}
600	4000	6.66×10^{10}
*600	8000	1.33×10^{11}
500	1000	2.17×10^{10}
500	2000	4.33×10^{10}
500	4000	8.66×10^{10}
500	8000	1.73×10^{11}
400	1000	2.67×10^{10}
400	2000	5.33×10^{10}
400	4000	1.07×10^{11}
400	8000	2.13×10^{11}
300	1000	3.33×10^{10}
300	2000	6.66×10^{10}
300	4000	1.33×10^{11}
300	8000	2.66×10^{11}

Table 5.1: List of models with direct heating of TMR and lower chromosphere. A heating function used in the model marked with * is plotted in Figure 5.8.

Synthetic spectra of the above described models were assessed in order to find features similar to the observed ones. The profiles of the Hγ line in Figure 5.9 show a massive rise in the wings that stretches into the continuum when the heating rate was equivalent to a particle beam flux of $\sim 10^{11}$ erg cm^{-2} s^{-1} or higher. The line profiles

also show a correlation between the heating rate and a rise in the continuum. Broad-band spectra consisting of both quiescent and 'flare' spectra are presented in Figure 5.10, where the filling factor is equal to 0.04 (the lower estimate presented in Section 3.1).

The 'flaring' profiles in this experiment were taken at t = 10 s of the simulations that had a duration of 20 s.

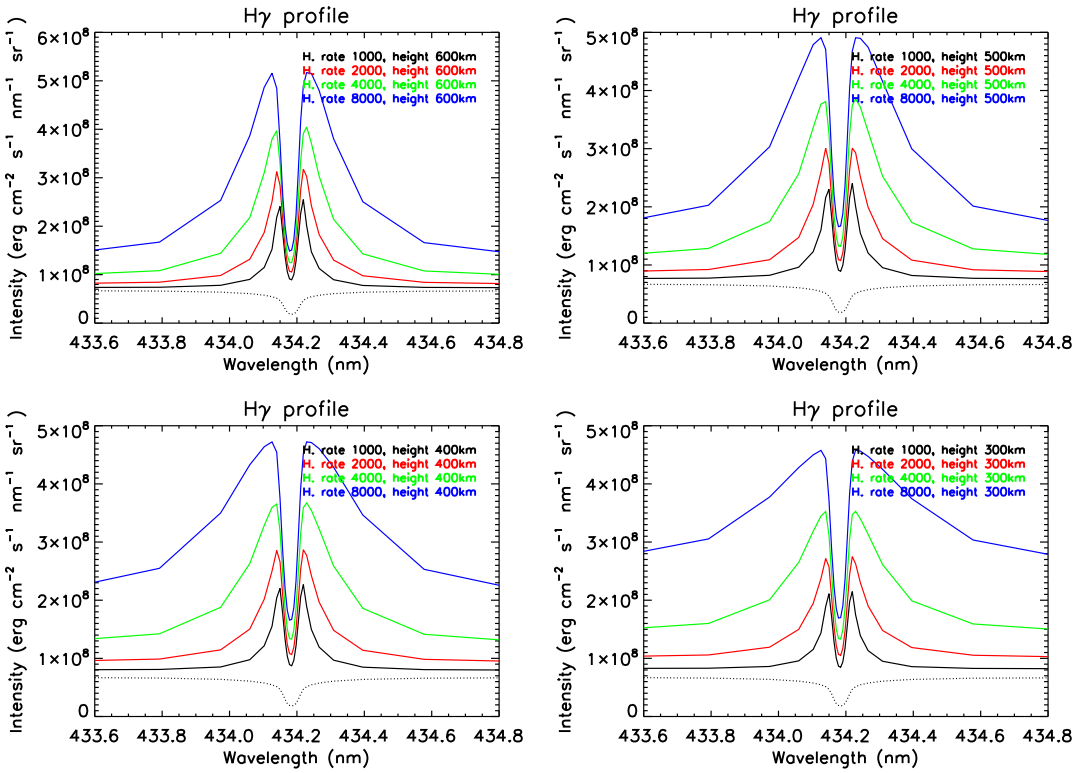

Figure 5.9: Profiles of the Hγ line in models of direct heating, as described in Table 5.1. The dotted line marks the quiescent profile.

5.4.2 Beams with high low energy cutoff

For a fixed particle beam flux, the power input into the atmosphere decreases with increasing E_C. However, the previous experiment clearly shows that a high energy deposited into sufficiently deep layers of the atmosphere can reproduce both the WL excess and avoid the emission in the higher order hydrogen Balmer lines. Therefore,

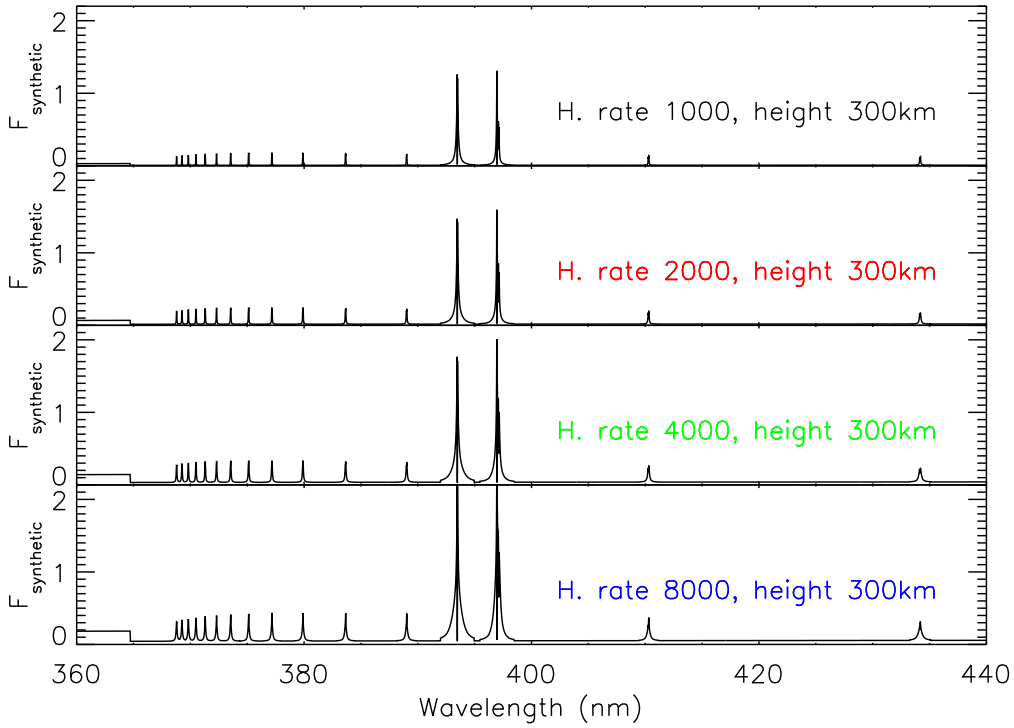

Figure 5.10: Synthetic spectra from models of direct heating with a lower boundary of energy deposition at 300 km above photospheric floor. Filling factor = 0.04.

we investigated whether it is possible to reproduce the WL excess together with the absence of the higher order Balmer lines when using an electron beam with a flux typical in an X1-class flare (10^{11} erg cm^{-2} s^{-1}, Kennedy et al. 2015).

The spectra in Figure 5.11 show that the beams with high E_C can reproduce spectra similar to those in Figure 5.9. It suggests that such beams can deliver a substantial energy into the TMR or the upper photosphere. Figure 5.12 shows that the electron beams caused a significantly greater temperature increase in the chromosphere compared to the proton beams. This temperature increase translates into the stronger emission in the Hγ line wings. The continuum level in both the electron beam-driven models is on the same level, which indicates that for the continuum level the temperature at an atmospheric height of $\sim$ 500 km is the most important.

The synthetic spectra in Figure 5.13 are emulating the observations with the filling

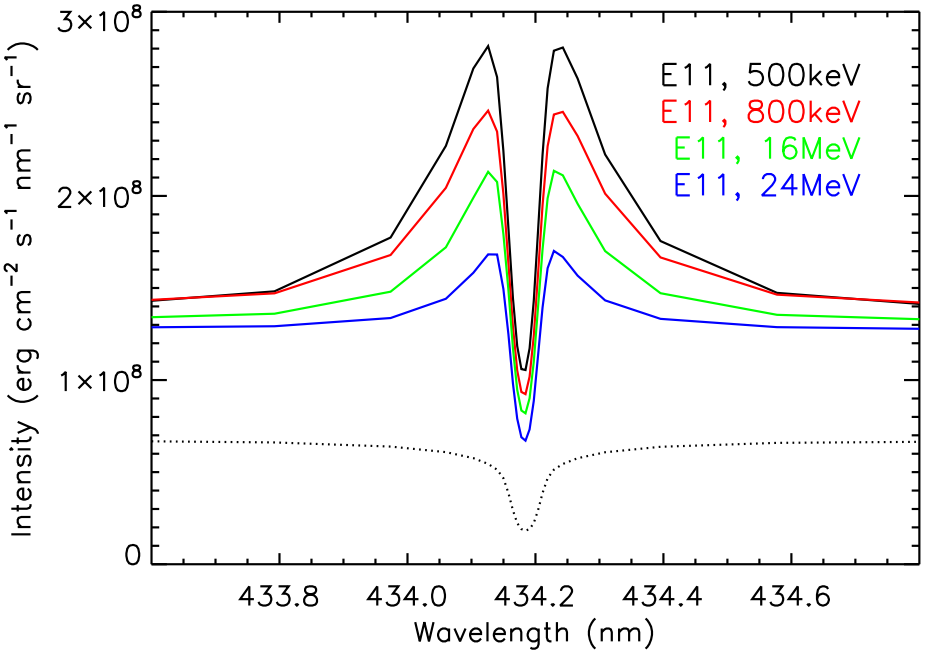

Figure 5.11: Hγ line profiles from models with high E_C. The legend shows the beam flux in units of erg cm^{-2} s^{-1} and E_C. The models with $E_C < 1$ MeV are driven by electron beams, the remaining models are driven by proton beams. The dotted line represents the quiescent line profile.

factor of 0.07 show that the higher order Balmer lines are significantly weaker than the Ca II K&H lines along with the elevated continuum and the visible Balmer jump. These spectral signatures match the best with those seen in the experiment with the direct energy deposition in the TMR and the upper photosphere (Section 5.4.1).

5.5 Summary

The models in this chapter show that the significance of the initial atmospheric conditions, the beam description, and the return current increase with the beam energy flux. For beams dominated by protons, the return current has a negligible effect. It was also shown that the Balmer line suppression can be well reproduced by energy deposition at the TMR and the lower chromosphere. This can be achieved by particle beams with extremely high E_C.

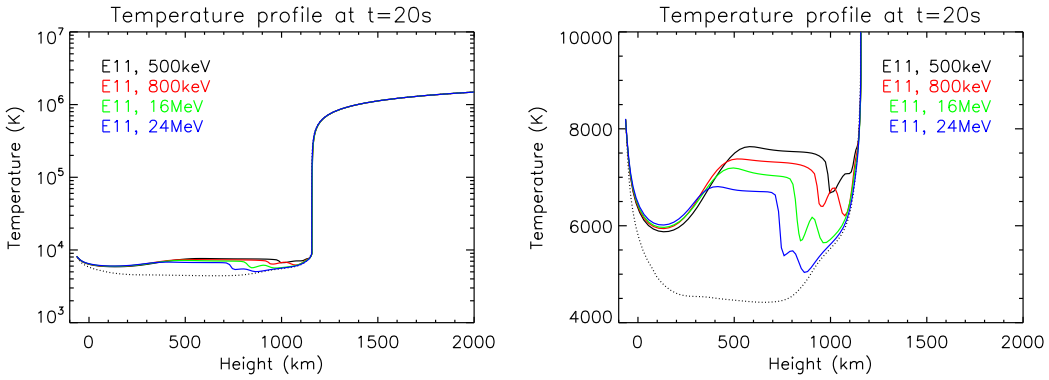

Figure 5.12: Temperature profiles of the models with high E_C. The legend shows the beam flux in units of erg cm^{-2} s^{-1} and E_C. The models with $E_C < 1$ MeV are driven by electron beams, the remaining models are driven by proton beams. The dotted line marks the initial temperature profile.

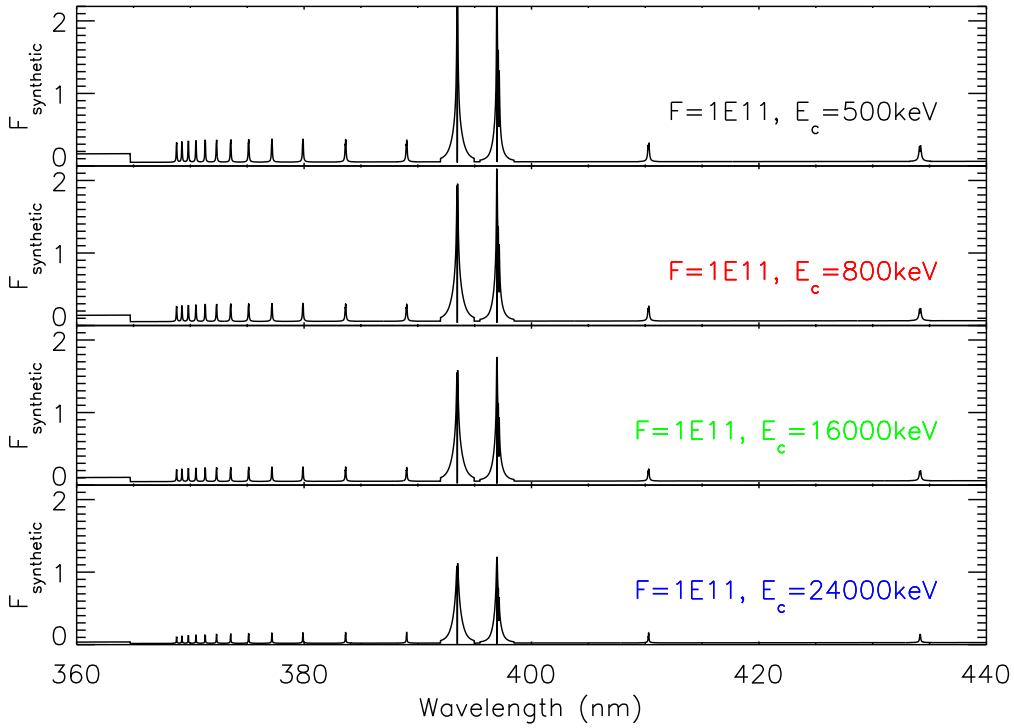

Figure 5.13: Relative flare excess for models with high E_C. The legend shows the beam flux in units of erg cm^{-2} s^{-1} and E_C. The models with $E_C < 1$ MeV are driven by electron beams, the remaining models are driven by proton beams. The filling factor was 0.07.

Chapter 6

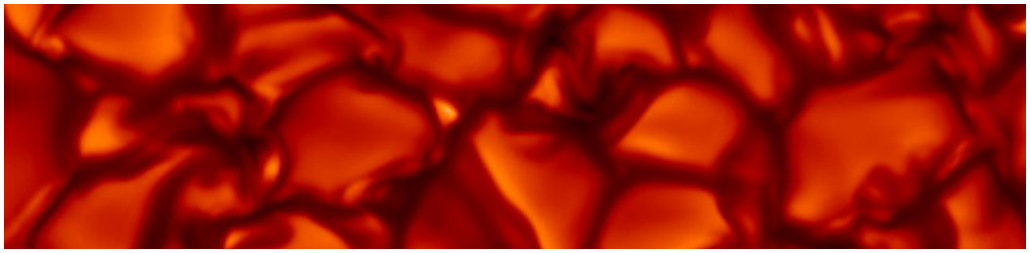

Models constrained with observations

We are the most afraid

of those demons

that we conceive

ourselves.

Chapter 3.1 showed that in the studied event the value of the E_C and power in non-thermal beams cannot be derived directly from the X-ray spectroscopic data. The next step was to create a grid of both electron and proton beam-driven models with the aim to reproduce the same spectral features. The beam parameters ranged from those commonly observed in solar flares, up to some very exotic ones. Once a match was found, the beams were confronted with the RHESSI and Fermi constraints. The results presented in this chapter were published in Procházka et al. (2018, 2019).

6.1 Observational constraints

As direct heating of the TMR was able to reproduce spectra with only a weak emission in the Balmer lines and clearly visible emission in the Ca II H&K lines, we had to investigate if particle beam with certain parameters can also reproduce these observational characteristics. Since RADYN allows us to model beams with a single type of particles, two grids of models were created. One with electrons and one with protons. All simulations lasted 60 s. A rapid onset of the beam (0.1 s) was followed with 30 s of steady flux and a 3 s decay. During the remaining 27 s the atmosphere was allowed to relax. Snapshots at $t = 20$ s were used to calculate spectra that employed the RH code and these spectra were analysed.

A comparison between models and observations employed the following criteria:

1. The Hγ/Ca II K peak ratio

   Based on IS observations, as described in Section 3.1, the Hγ/Ca II K peak ratio had to be ≤ 0.1. The criterion was hardened, since the ratio estimated in Figure 3.7 (0.15) was based on a maximal height of Hγ line still within the fluctuations. However, the actual measured height was lower.

2. Power within RHESSI/Fermi observed range

   For every value of E_C, the maximal electron/proton beam flux was derived from X-ray/γ-ray observations (Tables 3.1 and 3.3, respectively).

3. Positive contrast in the continuum at 615 nm

   Despite the fact that a quantitative criterion can be set based on HMI data, it was shown by Švanda et al. (2018) that in regions with strong magnetic field, the continuum levels are not reliable.

   Unlike the first criterion, the 615 nm contrast was investigated in pure flaring spectra, since the HMI data allowed to analyse the individual flaring pixels.

   The synthetic spectra, 615 nm is the wavelength closest to the HMI working wavelength.

On top of the above set criteria, the continuum redward of the Balmer jump (364.7 nm) and a rise in the Hγ line (434.159 – 434.186 nm) related to the initial value in the RH synthetic spectra, were analysed. The temperature at 300 km above the photospheric floor and the penetration depth of the beam were read out. The penetration depth was defined as a range of depths where volumetric beam heating reached at least 10% of its maximum value across the whole atmosphere.

6.2 Electron beam-driven models

In electron beam-driven models E_C was chosen to cover a wide range of observed values (20 – 120 keV) that reflect parameters found in the literature. The step was chosen to be 20 keV to provide a relatively fine grid. Four values were chosen for the electron flux. The choice was based on the estimated power in non-thermal electrons during the flare peak ($\sim 10^{27}$ erg s^{-1}, 5th panel of Figure 3.16) and a flaring area in the continuum at 617 nm ($1.1\times10^{17} - 3.3\times10^{17}$ cm^2, Section 3.3). The selected values of flux are 10^9, 3×10^9, 10^{10}, 3×10^{10} erg s^{-1} cm^{-2}. For the lowest flux (10^9) no rise in the 617 nm continuum was detected and models with this flux were not analysed any further. The numerical results for the electron beam-driven models are given in Table 6.1.

The most promising electron beams are those with a flux equal to 3×10^9 erg cm^{-2}

	E_C (keV)	Temperature at z = 300 km (K)	Penetration depth (km)	Rise in cont. > 364.7 nm	Hγ/Ca II K ratio	Rise in core of Hγ	Rise in cont. 615 nm
$F = 3 \times 10^9$ erg cm^{-2} s^{-1}	20	4608	480 – 1158	1.01	0.374	9.18	1.02
	40	4677	410 – 1156	1.01	0.307	6.53	1.03
	60	4630	363 – 1118	1.00	0.122	3.45	1.02
	80	**4617**	340 – 1040	**1.00**	**0.087**	**2.63**	**1.01**
	100	**4614**	316 – 997	**1.00**	**0.074**	**2.25**	**1.01**
	120	4614	293 – 975	0.99	0.065	2.02	1.01
$F = 1 \times 10^{10}$ erg cm^{-2} s^{-1}	20	4723.	433–1164	1.03	0.454	16.79	1.07
	40	4811	433 – 1156	1.04	0.414	14.36	1.10
	60	4990	363 – 1156	1.05	0.356	10.11	1.12
	80	4923	316 – 1149	1.04	0.288	7.68	1.11
	100	4873	293 – 1040	1.03	0.223	6.19	1.09
	120	4844	293 – 975	1.03	0.155	4.58	1.08
$F = 3 \times 10^{10}$ erg cm^{-2} s^{-1}	20	5022.	640–1167	1.11	0.433	25.54	1.21
	40	5336	387 – 1156	1.15	0.431	24.74	1.29
	60	5393	410 – 1156	1.19	0.419	22.15	1.38
	80	5489	340 – 1156	1.22	0.399	17.73	1.43
	100	5642	316 – 1156	1.23	0.367	14.39	1.44
	120	5571	293 – 1147	1.21	0.348	12.22	1.42

Table 6.1: Spectral diagnostics from electron beam-driven models 20 seconds into the simulation for a range of electron beam fluxes (F) and E_C. The signal presented in each waveband is the pure flaring signal relative to the initial/quiescent state. The models that comply with observations are typed in boldface.

s^{-1}. Their Hγ/Ca II K ratios are 0.122 (E_C = 60 keV), 0.087 (80 keV) and 0.074 (100 keV) (Figure 6.1). All these beams showed a positive contrast at 615 nm (1.02, 1.01 and 1.01, respectively) and lie within the observed RHESSI range of energies. For all these models the level of continuum redward of the Balmer jump (364 nm) remained unchanged. Models with a lower E_C produce too strong emission in Hγ. A higher energy flux (1×10^{10} erg cm^{-2} s^{-1} or more) is consistent with RHESSI constraints for E_C = 20 keV only. Such beams trigger too strong emission in Hγ. Also, in these models the level of continuum at 364 nm is increased. Generally, the continuum at 615 nm shows the same trends and higher contrast than the continuum at 364 nm. The contrast in both continua does not rise monotonically with E_C for a given beam flux. The peak moves to higher E_C if the beam flux increases (Figure 7.1).

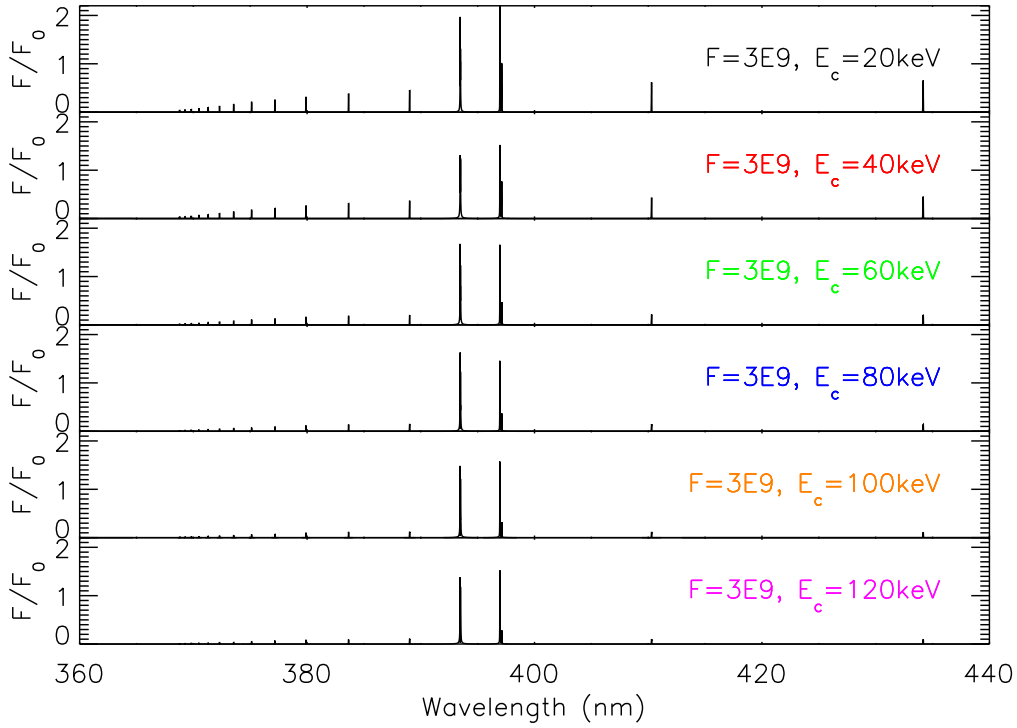

Figure 6.1: Relative flare excess for electron beam-driven models for a filling factor of 0.07.

Broader line profiles were found in models with higher beam flux and E_C. The line core flux was found to decrease with increasing E_C (Figure 6.2). Effects causing line

asymmetry and blue-shifted central reversal, become significant for higher beam fluxes.

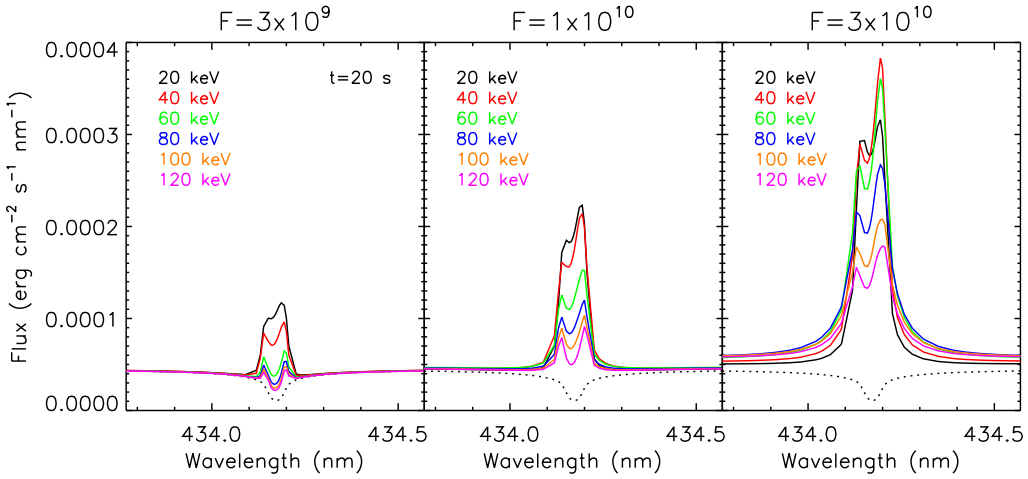

Figure 6.2: Pure Hγ line profiles for electron beam-driven models 20 s into simulation. The title of each box label beam flux in erg cm^{-2} s^{-1}. E_C is colour coded. The dotted line marks quiescent profile.

6.3 Proton beam-driven models

For the proton beam-driven models the same values of beam flux were used as for the electron beam-driven ones. Since the value of E_C cannot be derived from the Fermi data the E_C used in the models was guided by theoretical estimates. Švestka (1970) calculated that protons would need energy $\sim$ 20 MeV to penetrate to the photosphere. Machado et al. (1978) found that if protons were responsible for the TMR heating, the proton spectrum would have to be concentrated in the 10 – 20 MeV range. Machado et al. (1989) calculated that in the chromospheric backwarming scenario the protons would need energy at least 6 MeV to effectively heat the lower chromosphere. As the initial modelling attempts with sub 2 MeV showed strong emission in the Balmer lines, the values of E_C were chosen to be in a range of 2 – 16 MeV. The grid step was chosen to be a double of the previous value of E_C, to cover a relatively large area in the parameter space with a reasonable number of simulations.

E_C (keV)	Temperature at z = 300 km (K)	Penetration depth (km)	Rise in cont. > 364.7 nm	Hγ/Ca II K ratio	Rise in core of Hγ	Rise in cont. 615 nm
erg cm^{-2} s^{-1}						
$F = 3 \times 10^9$						
2000	**4598**	293 – 1078	**0.99**	**0.095**	**2.45**	**1.01**
4000	4621	172 – 907	0.99	0.063	1.77	1.00
8000	4659	73 – 753	0.98	0.046	1.31	1.00
16000	4713	–46 – 618	0.97	0.005	1.01	0.99
erg cm^{-2} s^{-1}						
$F = 1 \times 10^{10}$						
2000	4730.	293 – 1093	1.01	0.167	3.85	1.05
4000	**4803**	**172–907**	**1.00**	**0.094**	**2.53**	**1.06**
8000	4907	49 – 753	0.99	0.079	1.86	1.06
16000	5018	–46 – 618	0.97	0.069	1.35	1.05
erg cm^{-2} s^{-1}						
$F = 3 \times 10^{10}$						
2000	5195.	221 – 1149	1.09	0.429	11.59	1.22
4000	5292	172 – 929	1.10	0.116	3.70	1.25
8000	5440	49 – 753	1.10	0.103	2.54	1.27
16000	5591	–53 – 618	1.08	0.101	1.99	1.27

Table 6.2: Spectral diagnostics derived from proton beam-driven models for a range of proton fluxes and E_C. The data are presented in an identical way as in Table 6.1.

The numerical results for the proton beam-driven models are in Table 6.2.

The Hγ line in Figure 6.3 shows a similar pattern to electron beam-driven models with a more pronounced central reversal. However, the line tends to be weaker.

Of the modelled proton beams, a flux equal to 3×10^9 erg cm^{-2} s^{-1} produced a

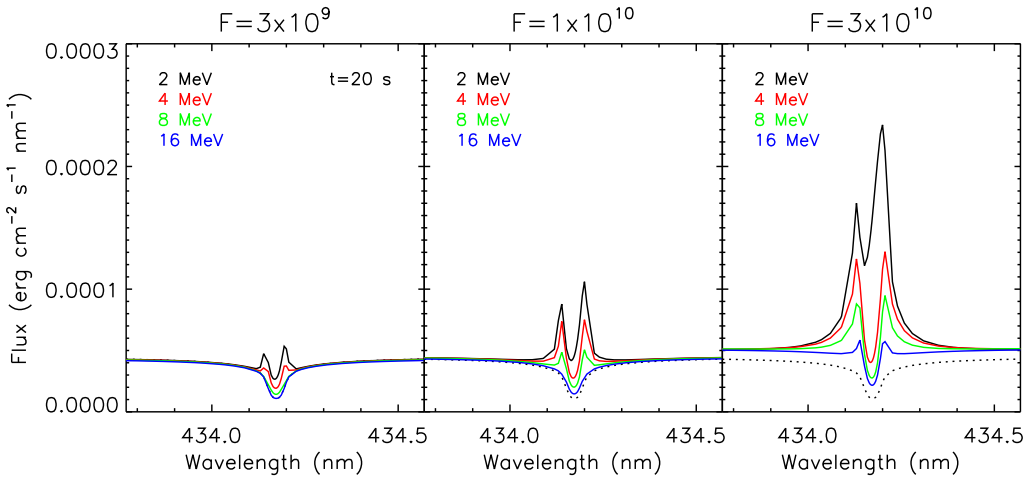

Figure 6.3: Pure Hγ line profiles for proton beam-driven models. The description is identical to Figure 6.2.

positive contrast at 615 nm only for E_C = 2 MeV, where the Hγ vs. Ca II K line ratio was 0.095. For a beam with flux 1×10^{10} erg cm^{-2} s^{-1} *Fermi* detected sufficient beam power if $E_C \leq 3.8$ MeV (Table 3.3). It is unlikely that such a beam would produce a noticeably different result than the one with E_C = 4 MeV. This beam showed a nearly identical Hγ vs. Ca II K ratio (0.094, Figure 6.4), which is very close to the beam mentioned above. A flux equal to 3×10^{10} erg cm^{-2} s^{-1} produced too strong emission in the higher order Balmer lines (E_C = 2 MeV). For the higher values of E_C the beam energy was out of the range observed by *Fermi* (Table 3.3).

6.4 Contribution functions

The contribution functions for the continuum at 615 nm of the favoured electron and proton-beam driven models are shown in Figure 6.5. It shows the atmospheric depths where the flux at the selected wavelength originates. The beam flux appeared to be the most important factor with respect to both the origin of the WL excess emission and WL contrast. A comparison of electron beams with E_C of 80 and 100 keV indicates that higher values of E_C result in a deeper penetration of the beam; however, the flux plays a more important role. From the numerical results in Table 6.3 it is clear that the

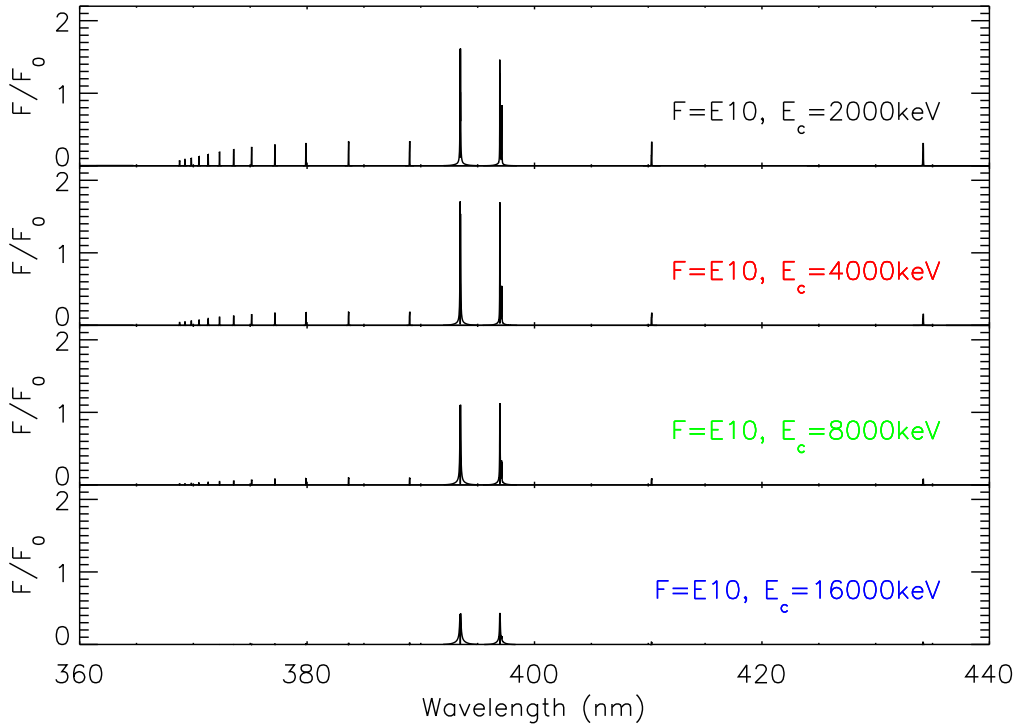

Figure 6.4: Relative flare excess for proton beam-driven models for a filling factor of 0.07.

Flux (erg cm^{-2} s^{-1})	E_c (keV)	Hγ/CaK ratio	WL contrast	Origin of middle 90% WL	Photospheric contribution
(e$^-$) 3×10^9	80	9%	1%	663 – 1060 km	4.1%
(e$^-$) 3×10^9	100	8%	1%	640 – 1040 km	7.0%
(p$^+$) 3×10^9	2000	10%	1%	663 – 1019 km	14.2%
(p$^+$) 1×10^{10}	4000	9%	6%	559 – 863 km	6.2%

Table 6.3: A summary of the beam parameters that are in best agreement with the observations. For the WL emission only the excess is quantified (4th, 5th and 6th columns).

photospheric contribution (defined as the contribution function integrated over heights 0 – 300 km) to the WL excess emission plays a minor role in this event and the excess continuum at 615 nm is predominantly formed in the lower chromosphere, no matter whether it is driven by electron or proton beams. The simulations did not show any significant shifts of the $\tau = 1$ surface, which means that the excess WL emission is optically thin. The resulting enhancement detected in this event was rather minor.

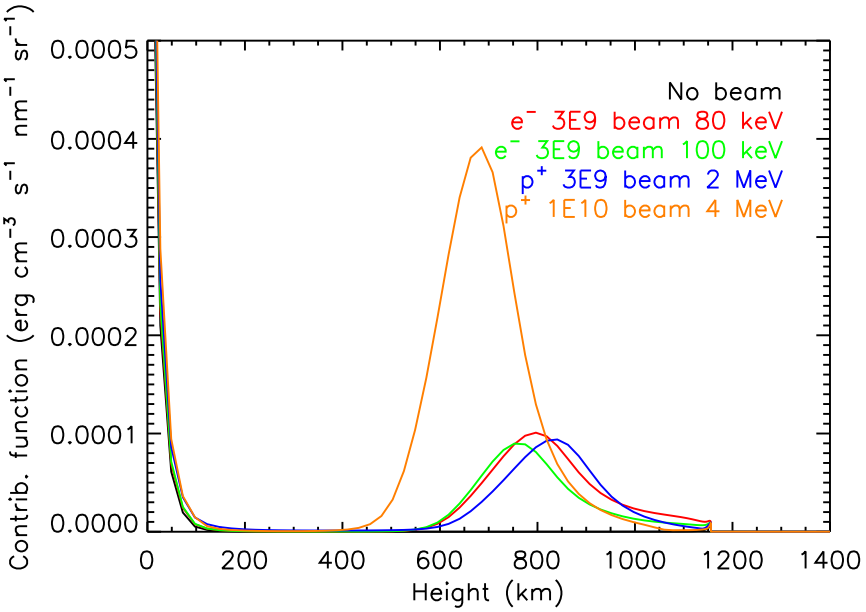

Figure 6.5: Contribution functions to continuum at 615 nm of the favoured electron (e^-) and proton (p^+) beam-driven models.

6.5 Temperature profiles

The temperature profiles in Figure 6.6 show that the electron beam with a flux of at least 1×10^{10} erg cm^{-2} s^{-1} causes a large disturbance in the chromosphere and shifts the transition region to greater geometrical heights. This is always accompanied by emission in the Balmer lines. In contrast, the proton beam-driven models with the same flux leave the upper chromosphere relatively undisturbed. For both electron and proton beams, a temperature rise appears deeper for higher fluxes, while the value of E_C has only a minor effect.

6.6 Hydrogen continuum energy

A detailed analysis of energy input and output into/from the flaring atmosphere revealed that:

1. The WL continuum in the studied event in its essence is the free-bound hydrogen continuum dominated by the Balmer and Paschen continua.

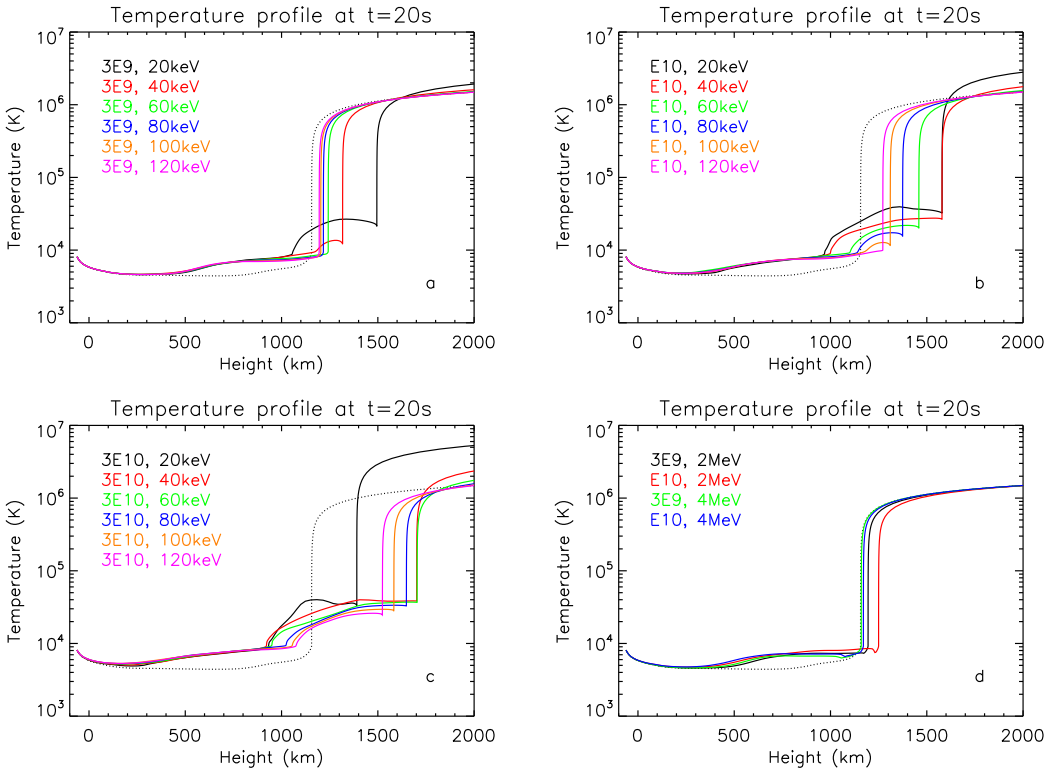

Figure 6.6: Temperature profiles for the electron beam-driven models (panels a, b, and c) and proton beam-driven models (panel d). The dotted line indicates the initial pre-flare atmosphere.

2. Based on the significance of the radiative backwarming, one can distinguish between the low and high energetic regime.

3. The absence of Lyman α and Lyman continuum emission indicates a high value of E_C.

Figure 6.7 shows the radiative losses in both the electron and proton beam scenarios for the studied WLF. The Lyman continuum is negligible, meanwhile the Balmer and Paschen continua dominate the radiative losses. The low energy regime is characterised by the absence of strong emission in the Lyman continuum (the observed light curve is in the top panel of Figure 3.9) and can be linked with the type II WLFs. If the energetic input into the chromosphere is sufficiently high, the emission in the Lyman continuum originating in the upper chromosphere causes a secondary photoionisation in the layer beneath (Figures 6.8 and 6.9). This can be performed by decreasing the E_C and/or increasing of beam flux with respect to the beam parameters that are able

to reproduce the observations. In this layer the Lyman continuum is absorbed and the higher order continua (predominantly the Balmer continuum) reach their maximum. However, this is not the chromospheric backwarming effect described by Metcalf et al. (1990), that leads to the thermal heating of the TMR via Balmer continuum absorption (Figure 6.10).

The energy regime can be easily distinguished from the observed Lyman emission. Figure 6.11 compares spectra of both the models that can reproduce the observations and the typical type I WLF in the vicinity of Balmer and Lyman jumps and Lyman α. The spectra show that the height of Balmer jump does not depend on the presence of low energy particles, but it is proportional to the total beam energy input. This is in contrast with the behaviour of the Lyman jump that is sensitive to energy input from the low energy particles that deposit their energy in the top chromosphere where the Lyman emission originates. The Lyman α line shows only a negligible change from the quiet profile in the models with beams that are able to reproduce the observations. Figure 6.12 shows a steep decline of both the Lyman vs. Balmer continuum flux ratio and Lyman vs. Balmer α flux ratio with increasing E_C. This reaches ~zero within the calculated range of E_C for the beam flux not greater than 10^{10} erg cm^{-2} s^{-1}. The radiative losses were calculated as an integral of dE/dt over the atmospheric heights greater than 300 km. The radiative gains were neglected.

6.7 Model uncertainties

Below we consider the most significant sources of error in this analysis.

1. Model geometry

   One dimensional models of the solar atmosphere cannot reproduce properly events located deep in the atmosphere and close to the limb. The models used in

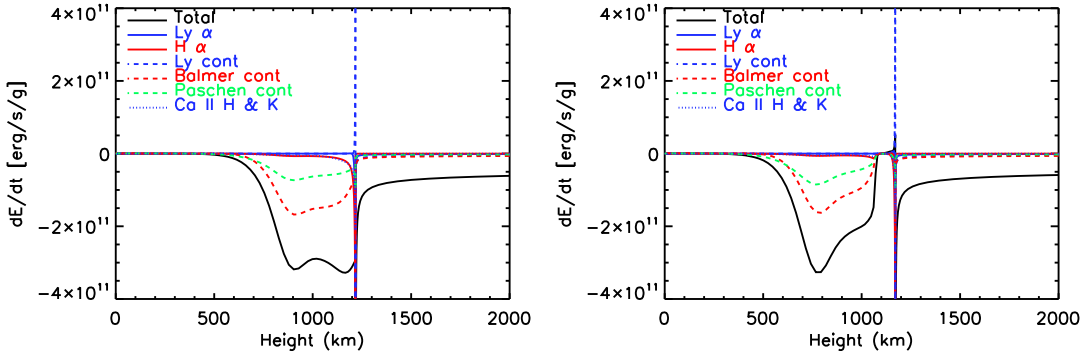

Figure 6.7: Radiative gains in the solar atmosphere due to the precipitation of electron (left) and proton (right) beams that are able to reproduce the observations (left: F = 3×10^9 erg cm^{-2} s^{-1}, E_C = 80 keV, right: F = 1×10^{10} erg cm^{-2} s^{-1}, E_C = 4 MeV).

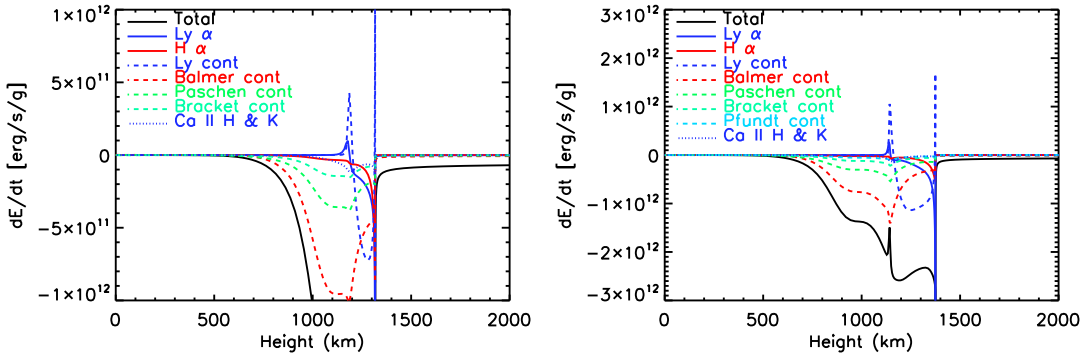

Figure 6.8: Radiative gains in the solar atmosphere due to the precipitation of electron beams. Left: F = 3×10^9 erg cm^{-2} s^{-1}, E_C = 40 keV, right: F = 1×10^{10} erg cm^{-2} s^{-1}, E_C = 80 keV.

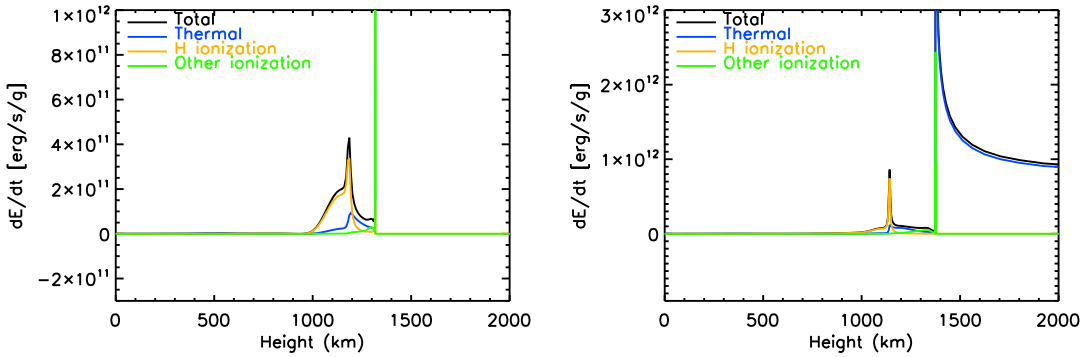

Figure 6.9: Ionising and heating rates in the solar atmosphere due to the precipitation of electron beams. Left: F = 3×10^9 erg cm^{-2} s^{-1}, E_C = 40 keV, right: F = 1×10^{10} erg cm^{-2} s^{-1}, E_C = 80 keV.

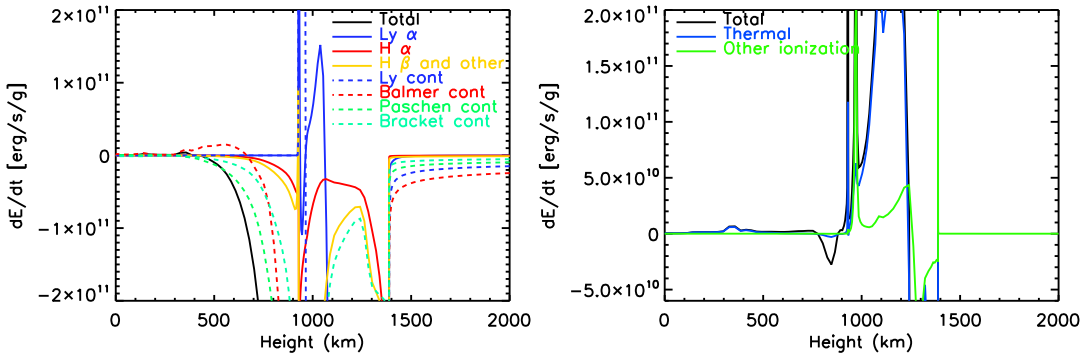

Figure 6.10: Radiative gains (left) and total energy balance (right) in the solar atmosphere due to the precipitation of a standard electron beam (F = 3×10^{10} erg cm^{-2} s^{-1}, E_C = 20 keV). Radiative backwarming of the TMR due to the Balmer continuum absorption is located at heights $\sim 300 - 500$ km above the photospheric floor.

this work have calculated the intensity as seen from an angle deviated by 27.5°, 60° and 83.5° from normal to the surface (Figure 6.13). In a situation where the event takes place close to the limb, a larger angle should be used. But this would show the event 'naked', meanwhile in real observations the event is seen though a thick layer of overlying quiet atmosphere (if not located on top). Since 3D models are not available, as a compromise the flux was used instead of the intensity in order to obtain quantitative results. For a comparison, numerical results based on the intensity as seen in an angle deviating by 27.5° in electron beam-driven models are shown in Table 6.4. The numbers are not qualitatively different, but the most promising models (E_C = 80 and 100) do not show a positive contrast at 615 nm that is greater than 1%. The Hγ/Ca II K ratio is only marginally different for the relevant models. The same is true for proton beam-driven models.

It is expected that the flare intensity decreases as the light travels through the overlying atmosphere but this decrease cannot be quantified, so the absolute line peaks cannot be compared with the observed ones. For this reason the Hγ vs. Ca II K line ratio was used instead, since the cores of both lines originate at similar atmospheric heights as seen in Figure 6.14.

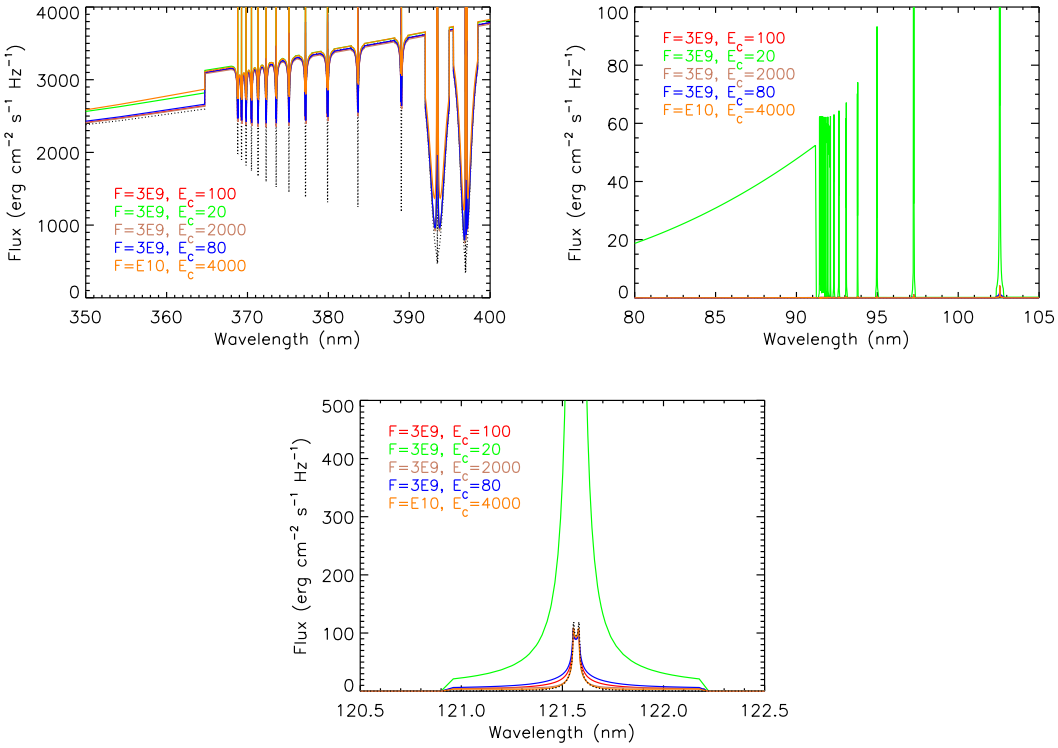

Figure 6.11: RH synthetic spectra of the higher order Balmer (Lyman) series and Balmer (Lyman) jump from both the models that are able to reproduce the observations and a typical type I WLF (green) are in the upper left (right) panel. Synthetic spectral profile of the Lyman α line is in the bottom panel. The legend shows the beam flux in the units of erg cm^{-2} s^{-1} and E$_C$ in the units of keV. The models with E$_C$ of tens (thousands) of keV are driven by electrons (protons). The dotted lines mark the quiescent profiles.

2. Beam distribution

   The beam applied in this work used a constant flux for 27 seconds, however the HXR data show a bursty character that could be better described by a series of triangular functions. Despite of the fact that each magnetic loop connected with such 'burst' has its footpoint at a different spatial location, some authors attempted to model the flare with a multithread setup to imitate the heating function as precisely as possible (Rubio da Costa et al. 2016). Such approach is important in order to reproduce the spectral signatures especially during the decay phase (Warren 2006).

   However, most authors modelled flares using single triangular functions (Brown et al. 2018; Druett & Zharkova 2018) or Gaussian function (Simões et al. 2017).

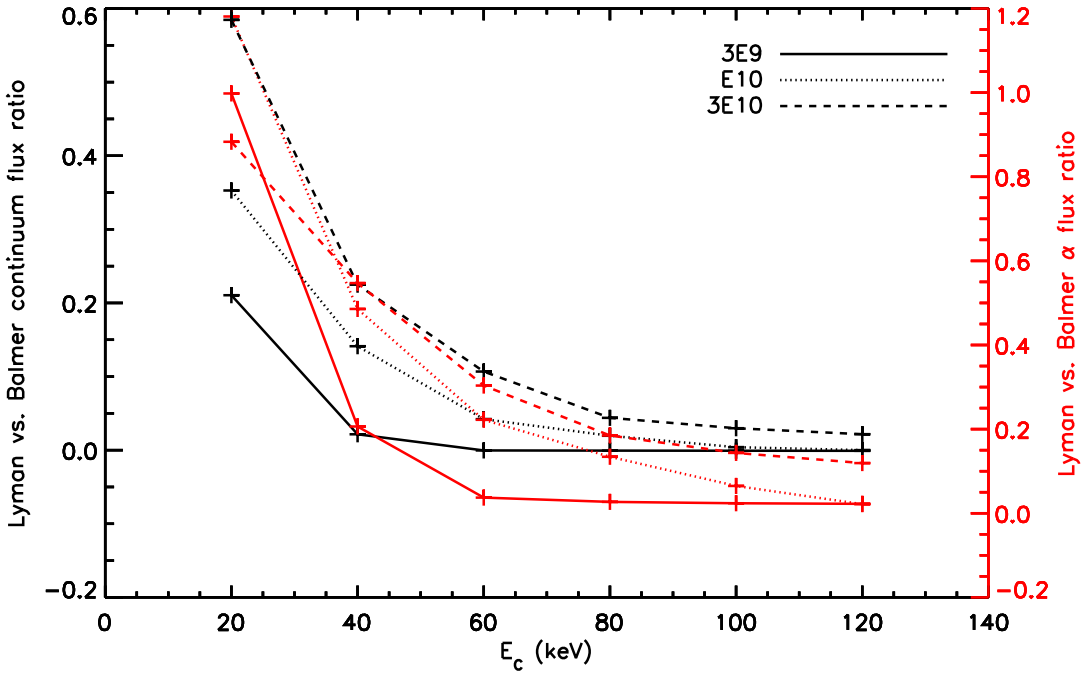

Figure 6.12: Energy loss ratios in the Lyman and Balmer continua (black) and Lyman and Balmer α lines (red) for electron beam-driven models. The legend denotes the electron beam flux.

Since the aim of this work was to study the beam interaction with the flaring atmosphere with respect to the beam parameters, it was more convenient to apply the studied beams with a constant beam flux for sufficiently long time to allow the atmosphere enough time to respond and reach a prospective new equilibrium. Abbett & Hawley (1999a) and Kowalski et al. (2016) chose a similar approach to study electron beams within a broad range of the energy flux (from 1×10^9 up to 5×10^{11} erg cm^{-2} s^{-1}). The results show that for the lower energy particle beams the line profiles in Figures 6.16 and 6.17 do not evolve significantly once the atmosphere responds on the initial heating shock.

3. The role of the filling factor

   Our filling factor estimate is based on IS's Hα context images that suffer from atmospheric seeing. Only images with the best seeing conditions were analysed. Ten points were chosen manually along the image aperture and used to fit a circle (Figure 6.15). The aperture's image was blurred, so the circle's diameter was

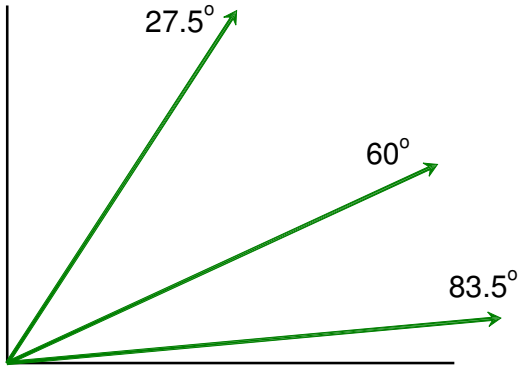

Figure 6.13: Geometry of the modelled atmosphere. Arrows show the directions in which the intensity was calculated (27.5°, 60° and 83.5°), the atmosphere's axis matches the vertical line.

		E_C (keV)	Rise in cont. > 364.7 nm	Hγ/Ca II K ratio	Rise in cont. 615 nm
F = 3×10^9	erg cm^{-2} s^{-1}	20	1.00	0.33	1.01
		40	1.00	0.34	1.01
		60	0.99	0.125	1.01
		80	0.99	0.088	1.00
		100	0.99	0.076	1.00
		120	0.99	0.068	1.00
F = 1×10^{10}	erg cm^{-2} s^{-1}	20	1.00	0.40	1.04
		40	1.01	0.35	1.05
		60	1.01	0.32	1.06
		80	1.00	0.30	1.06
		100	1.00	0.24	1.04
		120	0.99	0.17	1.04
F = 3×10^{10}	erg cm^{-2} s^{-1}	20	1.03	0.37	1.12
		40	1.04	0.37	1.16
		60	1.06	0.35	1.21
		80	1.07	0.34	1.24
		100	1.07	0.34	1.25
		120	1.06	0.33	1.24

Table 6.4: Spectral diagnostics from electron beam-driven models 20 seconds into the simulation for a range of electron beam fluxes (F) and E_C. For the spectral diagnostics the intensity at an angle of 27.5° was used instead of the flux.

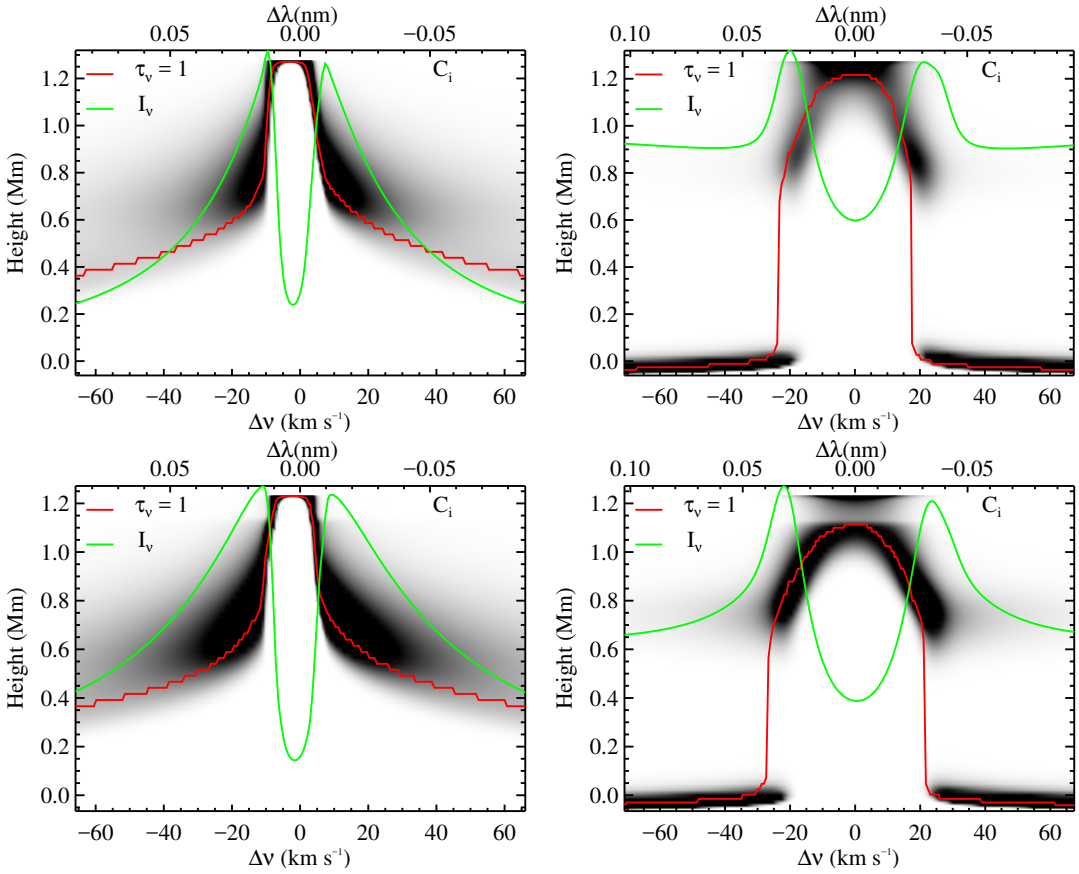

Figure 6.14: RH contribution functions for Ca II K (left) and Hγ (right) lines in the F = 3×10^9 erg cm^{-2} s^{-1}, E_C = 100 keV electron beam-driven model (upper row) and the F = 1×10^{10} erg cm^{-2} s^{-1}, E_C = 4 MeV proton beam-driven model (lower row). The $\tau = 1$ surface and line profile are marked with red and green, respectively. The areas with darker shadow contribute to the total intensity greater than areas with lighter shadow.

reduced to match only the area that was analysed by the spectrometer with certainty. The threshold for flaring pixels identification (twice the median value in the image) was chosen based on a visual match. Six images recorded between 9:04:23 and 9:04:41 UT were analysed this way and the filling factor was calculated (0.078 ± 0.003). Figure 6.15 shows that the area identified as flare is rather overestimated and may serve as an upper estimate for the filling factor. If the threshold for the flare detection is increased to 2.2 times the median, the filling factor decreases to 0.057. However, the filling factor does not affect the

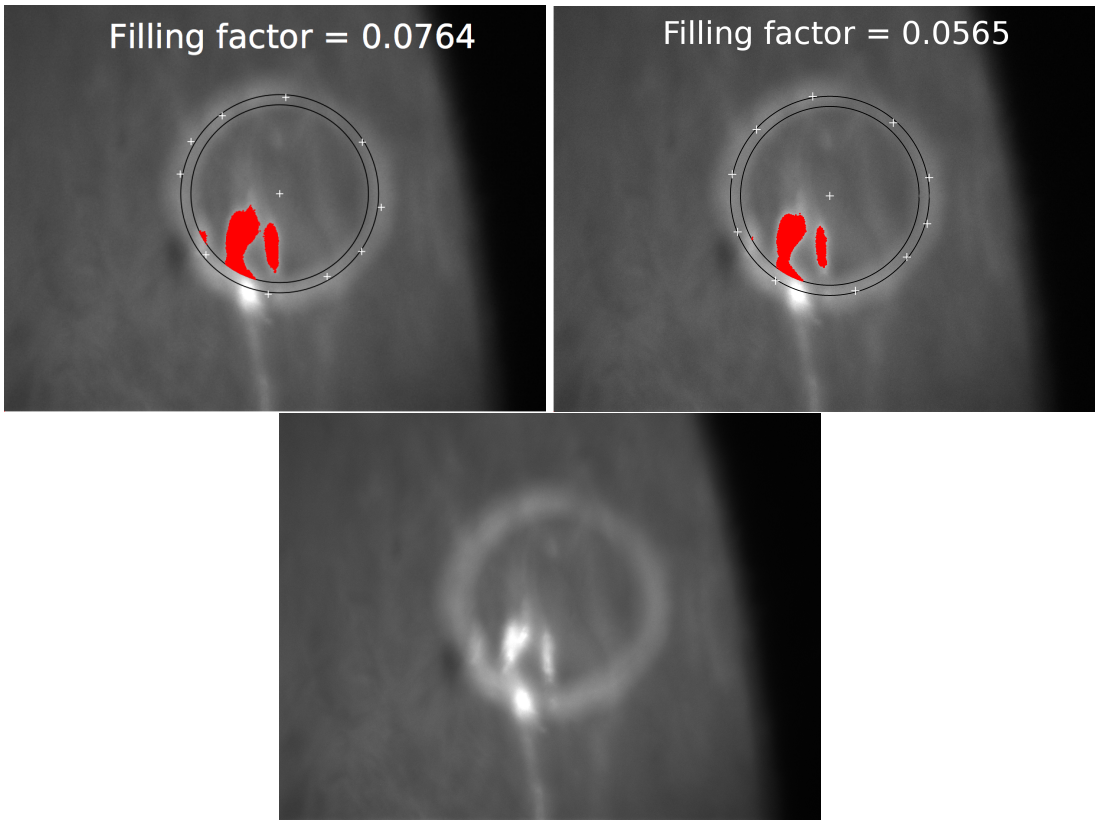

Figure 6.15: Estimates of Hα filling factor during the flare peak when threshold for flaring pixels equal to 2*median (upper left) and 2.2*median (upper right) are applied. Bottom picture: original image recorded at 9 : 04 : 32 UT. Flare area is red coloured.

Hγ/Ca II K ratio, since according to Equation 5.5

$$\begin{aligned} F_{synthetic} &= \frac{F_{flare} * ff + F_{non-flare} * (1 - ff) - F_{non-flare}}{F_{non-flare}} \\ &= ff * \frac{F_{flare} - F_{non-flare}}{F_{non-flare}}, \end{aligned} \tag{6.1}$$

the $F_{synthetic}$(Hγ)/$F_{synthetic}$(Ca II K) ratio does not depend on the ff. The filling factor therefore does not influence the match between the observed and synthetic spectra.

4. The flaring area in WL

   Based on HMI continuum difference imaging (Figure 3.14), two estimates of the flaring area in the continuum at 617 nm were made and consequently the beam flux was determined. Tables 3.1 and 3.3 show the maximum flux for both area

estimates and it is clear that the less conservative estimate restricts the parameter space so much so that no beam would comply with observations. It is unlikely that the flaring area could have been even smaller that the one marked with the smaller contours. It is also unlikely that the geometric distortion was different from the calculated factor 2.5, since the position of the flare was known with high precision.

5. Hγ/Ca II K ratio

   In order to minimise seeing effects, the spectra recorded over 30 s were averaged and the measurement of the Ca II K line height and fluctuations of continuum were carried out using this single spectrum. Figure 3.7 shows that the estimated 0.15 Hγ vs. Ca II K ratio is the upper limit, but the emission at the wavelength of Hγ was lower. However, even if the upper limit of the ratio was used, it would concede that the F = 3×10^9 erg cm^{-2} s^{-1}, E_C = 60 keV beam can reproduce the observations. This beam's E_C is still out of the range of the commonly observed values.

6. HMI WL contrast

   It has been noted that the HMI contrast is not reliable in areas with strong magnetic fields but the error cannot be estimated (Švanda et al. 2018). However, this did not play an important role in our analysis because the requirement from the models was to provide any increase of flux at 615 nm. There was no other instrument observing the flare in WL, so the HMI data are still the best to use.

7. Step in parameter space

   When determining a grid of models, a computation time has to be considered. Since a preliminary analysis of the beam parameter space had been performed, the parameter space could be well explored while keeping the total computation time reasonable. The grid was dense enough to show trends in the investigated parameters and provide positive results. A finer grid of proton beam-driven simulations would help to better locate the beam with a good match, but the results

would not be qualitatively different.

8. Time at which the simulations were evaluated

   As shown in Figures 6.16 and 6.17, the emission in the Hγ line is usually fully developed at $t = 20$ s, so there is no prospect of significant quantitative changes in longer lasting simulations. In the first few seconds of the electron beam simulations with lower E_C, the emission in Hγ flares up and then decreases, meanwhile the simulations with $E_C \geq 60$ keV show more gradual rise and then the intensity remains rather steady. Figure 6.17 suggests that some beams would need 30 or 40 seconds to reach a plateau, but do not suggest that the intensity would decrease to levels yielding to Hγ vs. Ca II K ratio close to 0.1.

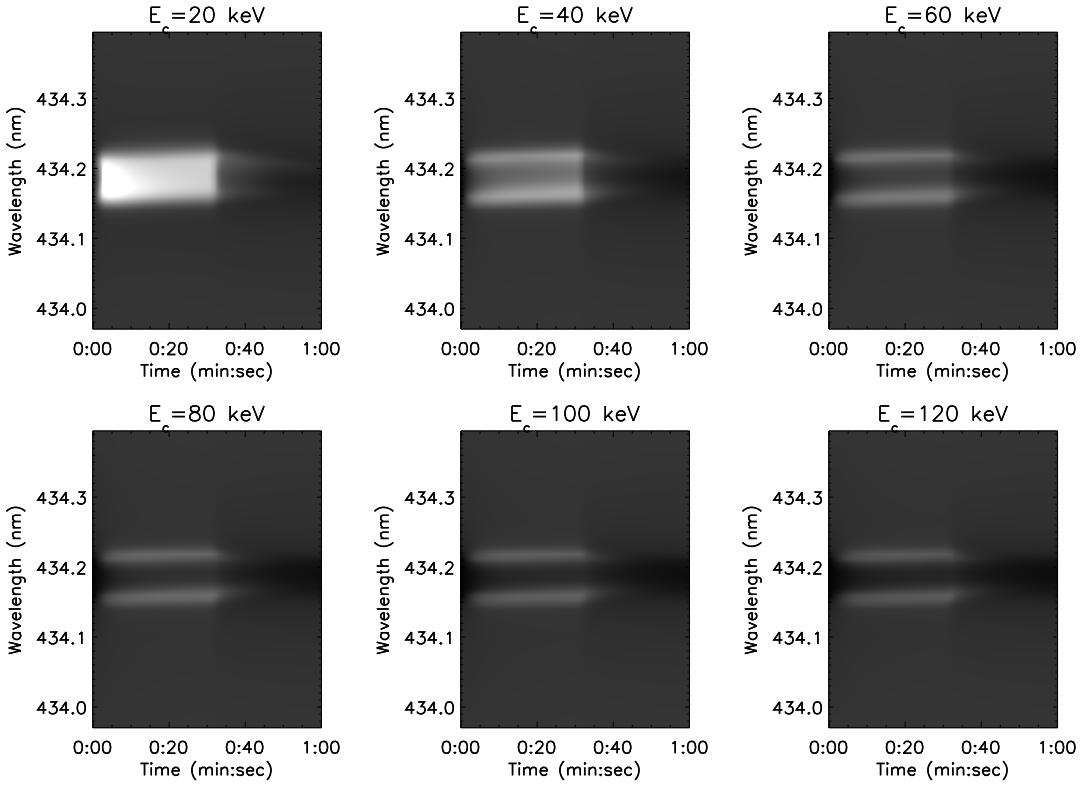

Figure 6.16: Evolution of the Hγ line profile in electron beam-driven models with a flux equal to 3×10^9 erg cm^{-2} s^{-1}.

9. Use of the Hγ line as a representative of the Balmer series

   Synthetic spectra in Figures 5.6, 5.10, 6.1 and 6.4 show that the Hγ line well

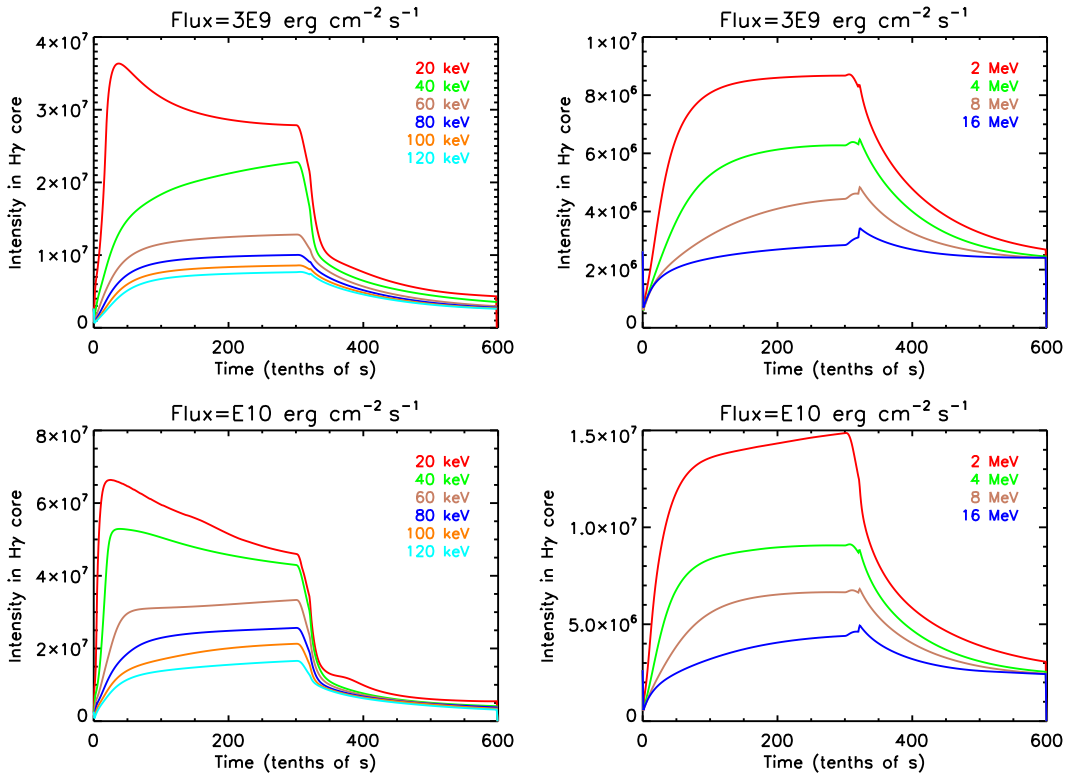

Figure 6.17: Evolution of the Hγ line core in selected electron beam-driven models (left panels) and proton beam-driven models (right panels).

aligns with the other higher order Balmer lines and do not show any irregularities with respect to other higher order lines of the series.

6.8 Comparison with comparing codes

HYDRO2GEN (Kobylinskii & Zharkova 1996; Zharkova & Zharkov 2007; Druett & Zharkova 2019) is a radiative hydrodynamic 1D code that successfully reproduced the large red-shift observed in the Hα line of a C1.5 flare (Druett et al. 2017). The code uses a Lagrangian coordinate ξ that stands for the column depth (ranging from 10^{17} cm^{-2} at the top of the chromosphere to 10^{23} cm^{-2} in the lower photosphere), instead of the coordinate along the flaring loop used in RADYN. The initial atmosphere is consistent with the quiet solar atmosphere excluding the corona. When the particle beam is injected at the top of the chromosphere, the hydrodynamic response generates a new flaring atmosphere with its own corona and compresses the underlying chromosphere

and photosphere towards higher column depths. Such flaring atmosphere is consistent with the flaring atmosphere used in this thesis (QS.SL.HT) that is also compressed compared to the standard quiet RADYN atmosphere (QS.SL.LT).

HYDRO2GEN considers a 5-level plus continuum hydrogen atom only that allows to model the mixed electron-proton beams (Zharkova & Zharkov 2015). This is probably the largest downside of HYDRO2GEN, since is does not allow to model line profiles of other elements in the solar atmosphere. However, unlike the RADYN code, the HYDRO2GEN code considers full non-LTE radiative transfer and takes into account the collisional excitation and ionization of hydrogen from all exited states. On the other hand, the non-LTE approach that includes statistical equilibrium at every time step, (assuming that the timescale for the radiative processes is much shorter than the hydrodynamic characteristic time), does not allow for non-equilibrium ionization. This effect was investigated by Brown (2019), who compared the RADYN output with the RH output incorporating both the CRD and PRD. They found that once the particle beam ceases, the statistical equilibrium is a poor assumption and the non-equilibrium effects become pronounced. The RADYN code is the only code of those named in this thesis that uses a full time-dependent solution for the radiative transfer equation and thus results automatically in non-equilibrium ionization. The recombination rates in HYDRO2GEN are much lower than the ionisation rates, yielding to a long-lasting Lyman emission after the particle beam stops. The radiative losses are calculated within the hydrodynamic part of the code. This is also different in RADYN, where both parts are run independently and pass the solutions to each other.

The particle beam heating function in the HYDRO2GEN is found from the solution of the continuity equation (Syrovatskii & Shmeleva 1972):

$$\frac{\partial}{\partial s}[vN(E,s)] + \frac{\partial}{\partial E}\left[\left(\frac{\mathrm{d}E}{\mathrm{d}s}\right)vN(E,s)\right] = 0, \tag{6.2}$$

where $\mathrm{d}E/\mathrm{d}s$ represents the energy loss, v is the velocity, E is the kinetic energy, and $N(E,s)$ is the concentration of fast particles with energy E at a distance s along the

flaring loop. We recall that in this thesis the beam energy losses were based on the solution of the kinetic Fokker-Planck equation (Equation 5.3). Under the conditions in the flaring chromosphere the principal energy losses are collisional due to the Coulomb interaction with the ambient electrons, protons, and neutral atoms:

$$-\left(\frac{\mathrm{d}E}{\mathrm{d}s}\right) = \frac{2\pi e^4 Z^2 n}{mv^2} \ln \frac{m^3 v^4}{\pi e^2 n \hbar^2} \equiv a\frac{n}{E}[\mathrm{eV}^2\ \mathrm{cm}^2], \tag{6.3}$$

where n is the particle concentration in the ambient plasma, and a is defined as:

$$a = 1.3 \times 10^{-13}\left[\ln \frac{E}{mc^2} - \frac{1}{2}\ln n + 38.7\right][\mathrm{eV/cm}]. \tag{6.4}$$

6.9 Summary

Both the electron beam and proton beam-driven models presented in this chapter were confronted with the observational constraints presented in Chapter 3. The models that comply with the constraints were analysed and it was found that the WL emission at 615 nm originates in the lower chromosphere. The top chromosphere was not disturbed, which is consistent with the lack of emission in the Lyman series originating there. The suppressed Balmer emission is consistent with the weak particle beam together with the strong background radiation in the near-UV/visible wavelength range.

Chapter 7

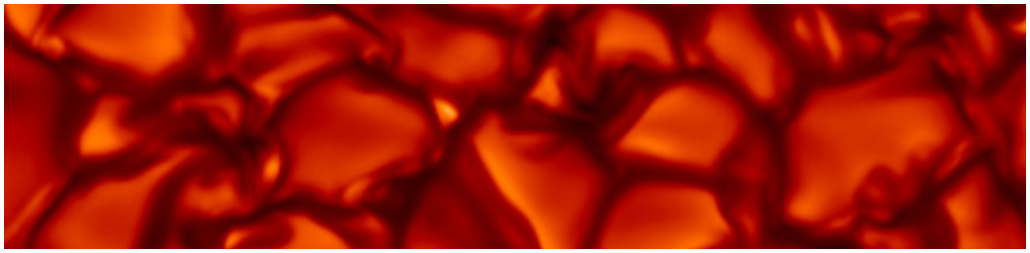

Concluding remarks and future work

If you think that you are not

big enough to change something

try to sleep

with a mosquito.

This work brought together a unique set of ground-based and space-based observations of an X-class solar flare and state-of-the-art radiative hydrodynamics models. The broadband NUV/visible high-cadence spectra are especially unique and have never been analysed before. The suppressed emission in both Lyman and Balmer lines is extraordinary during X-class flares. Together with the detected WL emission the reproduction of the spectral signatures poses a challenging task for radiative hydrodynamic modelling. The studied X1.0 event showed an extremely hard electron spectrum, which makes it difficult to estimate an accurate value for E_C. In such a hard spectrum, the flattening of the photon spectrum below E_C is likely to be the same regardless of the value of E_C. It is therefore difficult to obtain a definite set of beam parameters that can reproduce the observations. However, the observations restrict the parameter space to a relatively small area where commonly observed beams do not lie (Figure 7.1).

The modelling approach produced two electron and two proton beams that can reproduce the observations within the uncertainties. Of these four models, the 1×10^{10} erg cm^{-2} s^{-1}, 4 MeV proton beam produced the highest WL contrast at 615 nm (1.06) that agrees best with the value observed by HMI. The other three models had a lower beam flux and showed contrast of only 1.01, which is lower than the observed value. There was no increase detected redward from the Balmer jump, ruling out the presence of a hot blackbody component in the photosphere.

Further examination showed that electrons do not penetrate as deep as protons (316 versus 172 km above the photospheric floor), which is consistent with the lower temperature in the upper photosphere (4614 versus 4803 K) found in the electron beam-driven models. The models also show that electron beams with the beam parameters within the energy range allowed by RHESSI deliver their energy in the upper chromosphere ($\sim$ 1150 km), except from beams with F = 3×10^9 erg cm^{-2} s^{-1}, $E_C \geq 80$ keV. For proton beams, it is easier to penetrate through the upper chromosphere without depositing a significant amount of energy there.

Both electron and proton beam-driven models show similar observational trends - the

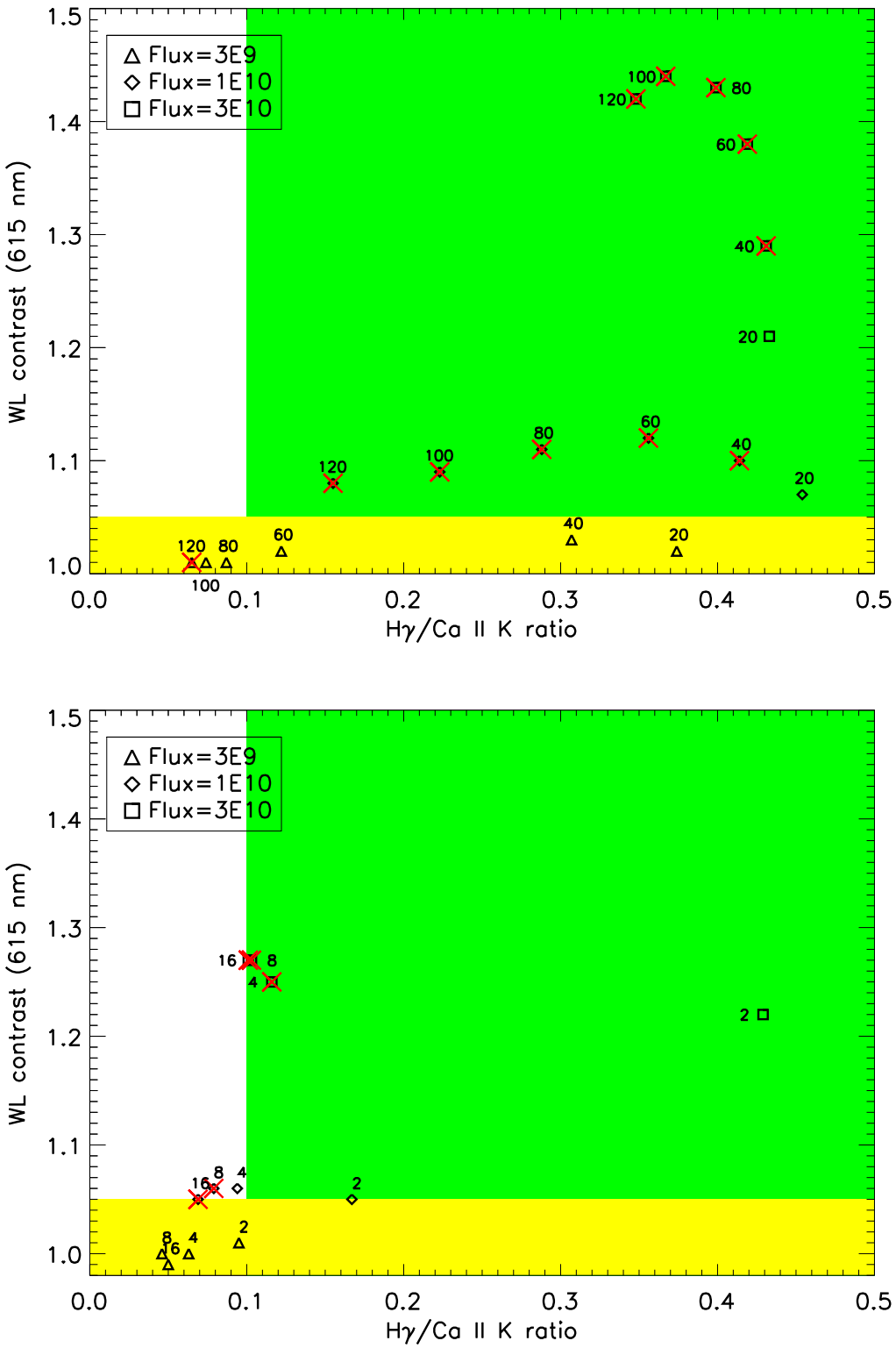

Figure 7.1: Positions of electron (upper panel) and proton (lower panel) beam-driven models along with values of low energy cutoff in a phase diagram showing observational constraints. Green and yellow areas mark parts of the parameter space with Hγ vs. Ca II K ratio greater than 0.1 and WL contrast at 615 nm lower than 1.05, respectively. The models out of range of RHESSI and Fermi constraints are marked with red crosses.

615 nm continuum emission gets stronger with increasing beam flux, but this also triggers stronger emission in the Balmer lines. With increasing E_C the emission in the Balmer lines become significantly weaker, while the continuum at 615 nm shows relatively small changes except for electron beams with a flux of 3×10^9 erg cm^{-2} s^{-1}.

Based on the presented results and a comparison with literature, the following conclusions related to the studied event can be obtained:

1. Spectral signatures of the studied type II WLF can be best reproduced with a relatively weak particle beam that has a high low energy cutoff.

2. Beams with such parameters are rare (Kuhar et al. 2016).

3. Both electron and proton beams can account for the observed type II WLF signatures.

4. The excess continuum emission at 615 nm originates over a broad range of heights in the lower chromosphere with a minor contribution from the photosphere (Figure 6.5).

5. The resulting E_C in this event do not agree with the commonly observed values reported by Fletcher et al. (2007b).

Some additional general conclusions can be stated based on the results presented in this thesis:

1. Proton beams more easily penetrate through the upper chromosphere without triggering a strong emission in the higher order Balmer lines and at the same time can carry more energy.

2. The height of Balmer jump is proportional to the total energy input to the chromosphere, but the Lyman jump is sensitive to low energy particles only. Though, the absence of a Balmer jump indicates solely a low energy particle beam in the

flare, meanwhile the absence of a Lyman jump is the indicator of missing low energy particles in the beam and better characterises the type II WLFs.

3. Solely based on a temporal match between WL emission and the peak of HXR, it cannot be decided if the studied event is a type I or type II WLF. This contradicts the conclusions of Fang & Ding (1995).

4. Only beams that are sufficiently intense can trigger emission in the WL continuum. This contradicts the statement by Jess et al. (2008) that 'there is no reason why WLF emission should not be produced in all flares'.

5. The results do not agree with a conclusion of Fletcher et al. (2007a) that the visible/UV continuum requires an electron beam with a cutoff energy well below 25 keV in order to deliver sufficient energy into the atmosphere.

The conclusions of thesis have re-opened the question of the role of protons in flares. A large statistical study of 38 solar flares of cycle 23 by Emslie et al. (2012), incorporating RHESSI data, allows a comparison with the event studied in this thesis. They found that for 5 of 21 events, in which they were able to estimate the energy in both electron (E > 20 keV) and ion (E > 1 MeV) beams, the energy in ions was greater than the energy in electrons, and in 2 events the energy in ions was more than twice than the energy in the electrons. However, the authors admit that their electron energy estimates suffer from an order of magnitude uncertainty, while the ion energy uncertainty is even larger. They also found that the Spearman's rank correlation coefficient that quantifies a correlation between two quantities, no matter if linear or not, between ion and electron energies, was equal to 0.20. This indicates the existence of beams with various particle compositions and discards the idea of electron beam dominance in all flares.

Indeed, for the event studied in this thesis, the most energetic electron beam consistent with the RHESSI constraints (Table 3.1) has the power of 4.3×10^{26} erg s^{-1}, meanwhile the proton beams consistent with the Fermi constraints (Table 3.3) have powers of 7.06×10^{27} erg s^{-1} for E_C = 2 MeV and 8.82×10^{26} erg s^{-1} for E_C = 4 MeV. Note

that the maximum E_C for the 10^{10} erg cm^{-2} s^{-1} proton beams was 3.8 MeV, therefore the real E_C value was most likely between 2 and 4 MeV.

Watanabe et al. (2017) calculated the energy deposition rate for electron beams in flares of importance M8.7 to X2.2 assuming E_C = 30 keV. The rate was equal to $4.15 \pm 2.72 \times 10^{28}$ erg s^{-1} for WLFs and 3.09×10^{27} erg s^{-1} and 5.97×10^{28} erg s^{-1} for two more examples (X1.2 and X1.0, respectively) where the WL emission was not detected. These numbers put the most energetic electron beam that is still within the RHESSI constraints for the flare studied in this work out of range of any conceivable scenarios involving the standard model. A similar statistic study for proton beams is not available.

One of the limiting factors in solar WLF research is the small number of well observed flares. Broad spectral coverage at high temporal resolution is important to track the changes in continua, especially during the impulsive phase.

IS is a prototype of a new instrument design that can be further developed in order to automate the observations. Since the greatest changes in spectra are expected during the impulsive phase, a proper selection of the observed active region is crucial. A multi-fibre based slit can be used to observe multiple locations simultaneously (Choudhary et al. 2013).

The instrumentation can be improved with an inclusion of additional beam splitters and context imagers working at several different wavelengths. The aim would be to record the Sun on both sides of hydrogen series limits, which try to discover spatial displacements between the origin of the different types of continua.

Another problematic part of flare research is the uncertainty in the determination of the particle beam parameters. RHESSI proved to be a useful instrument but its dynamic range is limited (maximal contrast of the X-ray sources is $\sim 1:100$). Also, since its launch in 2002 it has suffered an advanced level of degradation and its output has to be analysed very carefully. A new generation of solar dedicated X-ray observatories is planned to be launched in the next years. The Spectrometer/Telescope for Imaging X-rays (STIX, Benz et al. 2012) on board of European Space Agency's Solar Orbiter will

use the same approach as RHESSI, but its 32 detectors will provide a better resolution in an energy range 4 - 150 keV. Another successor will be NASA's Focusing Optics X-ray Solar Imager (FOXSI, Krucker et al. 2009) with significantly improved sensitivity when compared to RHESSI, which should observe the Sun in an energy range 3 – 100 keV with a sub-second temporal resolution.

Solar Orbiter is a forthcoming European Space Agency's mission that will carry a new generation of instruments to observe the Sun in the visible, UV and X-ray wavelength range. The models presented in this thesis can be used to predict the type II WLF spectral signatures realistically observable by Solar Orbiter. When the synthetic spectra are convolved with the instrumental profiles (Brown et al. 2018), the outputs can be used to identify the early signs of a flare and help to download only the high quality data. As regards to the modelling work, there is a need for 3D RHD models that can accurately simulate the radiative emission originating in the deep layers of the solar atmosphere as it travels through the overlying layers.

In this thesis we did not investigate the heating due to Alfvén waves that were recently suggested as a potential source for delivering a significant portion of energy into the lower atmosphere (Fletcher & Hudson 2008). Alfvén waves, together with fast-mode and slow-mode MHD waves, are produced in the process of magnetic reconnection due to the relaxation of the originally stressed (stretched and/or twisted) magnetic field lines. Only the waves propagating along the just-reconnected magnetic field lines can effectively transport energy from the reconnection site towards to the denser layers of the atmosphere. Kerr et al. (2016) modified the version of RADYN used in this thesis in order to compare Alfvén waves heating with the electron beam-driven heating in flares and studied the chromospheric Mg II k (279.6 nm) and Ca II (854.2 nm) line profiles in both scenarios. They found that the Alfvén waves led to a flatter heating profile with the main observational difference lying in the Mg II k line profile, which appears single peaked, redshifted, and with an extended blue wing or shoulder. These characteristics match better their observations (Kerr et al. 2015). Most recently Reep et al. (2018) used the HYDRAD code (HYDrodynamics and RADiation, Bradshaw & Mason

2003) and the magneto-hydrodynamics Lagrangian-Eulerian Remap 3D code (Lare3D, Arber et al. 2001) to study travel time effects due to the propagation of Alfvénic waves and the effect of ionization on the wave damping. They found that Alfvén waves ionize the plasma, but once it gets ionized the subsequent waves travel trough yielding deeper penetration. This is qualitatively different from the beam heating scenario, since the beam penetration depth mostly depends on the beam parameters, or, due to chromospheric evaporation, the heating maximum can move slightly to higher geometric heights. In any future work it would be useful to investigate whether Alfvén waves could be responsible for the observed spectral signatures for the flare studied in this thesis.

In the first chapter the four main questions were formulated:

1. What is the difference in the nature of type I and type II WLFs?
2. What type of particle beams can trigger WL emission while leaving the upper chromosphere undisturbed?
3. Where does the WL excess emission originate?
4. What is the emission mechanism of type II WLFs?

Based on the work presented in this thesis, the above questions can be answered in the following way:

1. It was found that type II WLFs differ from type I WLFs in the beam composition. Meanwhile there is no lower limit on E_C in type I WLFs, the E_C has to be significantly higher ($\sim$ 100 keV) in type II WLFs, if the beams are dominated by electrons. Alternatively, the type II WLFs can be dominated by protons.
2. Both electron and proton-dominated beams can trigger WL emission and not disturb the upper chromosphere, if the low energy cutoff is high enough. For more intense beams, the E_C has to be higher. However, for electron beams the

E_C would have to be higher that commonly observed in flares (Table 1 in Fletcher et al. 2007b). Already for flux equal to 1×10^{10} erg cm^{-2} s^{-1} the E_C would have to be well above that of 100 keV, as it results from temperature profiles in Figure 6.6 and Hγ vs. Ca II K ratio in Figure 7.1.

3. For the studied event that is characterised by a rather weak beam flux the WL excess predominantly comes from the lower chromosphere.

4. This work showed that the type II WLFs are consistent with the standard flare model. If the beam flux is low enough and the E_C is high enough, then the particle beam does not completely ionise the top of the chromosphere. The energy deposited into the chromosphere by the particle beam is dominantly balanced out by the radiative free-bound transitions in hydrogen atoms, excluding the Lyman continuum (Figures 6.7).

Bibliography

Abbett, W. P. & Hawley, S. L. 1999a, ApJ, 521, 906

Abbett, W. P. & Hawley, S. L. 1999b, in Astronomical Society of the Pacific Conference Series, Vol. 158, Solar and Stellar Activity: Similarities and Differences, ed. C. J. Butler & J. G. Doyle, 212

Aboudarham, J. & Henoux, J. C. 1986, A&A, 156, 73

Aboudarham, J. & Henoux, J. C. 1987, A&A, 174, 270

Ackermann, M., Allafort, A., Baldini, L., et al. 2017, ApJ, 835, 219

Alexander, D. & Metcalf, T. R. 1997, ApJ, 489, 442

Allred, J. C. 2005, PhD thesis, University of Washington, Washington, USA

Allred, J. C., Kowalski, A. F., & Carlsson, M. 2015, ApJ, 809, 104

Anders, E. & Grevesse, N. 1989, Geochimica Cosmochimica Acta, 53, 197

Arber, T., Longbottom, A., Gerrard, C., & Milne, A. 2001, Journal of Computational Physics, 171, 151

Aschwanden, M. J. 2002, in Bulletin of the American Astronomical Society, Vol. 34, American Astronomical Society Meeting Abstracts #200, 722

Aschwanden, M. J. 2005, Physics of the Solar Corona. An Introduction with Problems and Solutions (2nd edition)

Asplund, M., Grevesse, N., Sauval, A. J., & Scott, P. 2009, Annu. Rev. Astron. Astrophys., 47, 481

Avrett, E. H. & Loeser, R. 1992, in Astronomical Society of the Pacific Conference Series, Vol. 26, Cool Stars, Stellar Systems, and the Sun, ed. M. S. Giampapa & J. A. Bookbinder, 489

Ben-Israel, A. 1966, Journal of Mathematical Analysis and Applications, 15, 243

Benz, A. O., Krucker, S., Hurford, G. J., et al. 2012, in Proceedings of the SPIE, Vol. 8443, Space Telescopes and Instrumentation 2012: Ultraviolet to Gamma Ray, 84433L

Bespalov, P. A., Zaitsev, V. V., & Stepanov, A. V. 1988, Solar Phys., 114, 127

Bissaldi, E., von Kienlin, A., Lichti, G., et al. 2009, Experimental Astronomy, 24, 47

Bonanno, A., Schlattl, H., & Paternò, L. 2002, A&A, 390, 1115

Boyer, R., Sotirovsky, P., Machado, M. E., & Rust, D. M. 1985, Solar Phys., 98, 255

Bradshaw, S. J. & Mason, H. E. 2003, A&A, 401, 699

Brown, J. C. 1971, Solar Phys., 18, 489

Brown, S. A. 2019, PhD thesis, University of Glasgow

Brown, S. A., Fletcher, L., Kerr, G. S., et al. 2018, ApJ, 862, 59

Candelaresi, S., Hillier, A., Maehara, H., Brandenburg, A., & Shibata, K. 2014, ApJ, 792, 67

Carlsson, M. 1986, Uppsala Astronomical Observatory Reports, 33

Carlsson, M. 1998, in Lecture Notes in Physics, Berlin Springer Verlag, Vol. 507, Space Solar Physics: Theoretical and Observational Issues in the Context of the SOHO Mission, ed. J. C. Vial, K. Bocchialini, & P. Boumier, 163

Carlsson, M. & Stein, R. F. 1992, ApJL, 397, L59

Carlsson, M. & Stein, R. F. 1994, in Chromospheric Dynamics, ed. M. Carlsson, 47

Carlsson, M. & Stein, R. F. 1995, ApJL, 440, L29

Carlsson, M. & Stein, R. F. 1997, ApJ, 481, 500

Carmichael, H. 1964, NASA Special Publication, 50, 451

Carrington, R. C. 1859, MNRAS, 20, 13

Cavallini, F. 2006, Solar Phys., 236, 415

Chen, P.-F., Fang, C., & Ding, M.-D. D. 2001, Chinese Journal of Astronomy and Astrophysics, 1, 176

Choudhary, D. P., Yurchyshyn, V., & Gosain, S. 2013, in Proceedings of the SPIE, Vol. 8862, Solar Physics and Space Weather Instrumentation V, 88620B

Cox, A. N. & Pilachowski, C. A. 2000, Physics Today, 53, 77

Crotser, D. A., Woods, T. N., Eparvier, F. G., Triplett, M. A., & Woodraska, D. L. 2007, in Proceedings of the SPIE, Vol. 6689, Solar Physics and Space Weather Instrumentation II, 66890M

Czerny, M. & Turner, A. F. 1930, Zeitschrift für Physik, 61, 792

De Pontieu, B., Title, A. M., Lemen, J. R., et al. 2014, Solar Phys., 289, 2733

Dennis, B. R. 1985, Solar Phys., 100, 465

Dennis, B. R. & Schwartz, R. A. 1989, Solar Phys., 121, 75

Ding, M. D., Fang, C., & Yun, H. S. 1999, ApJ, 512, 454

Donati-Falchi, A., Falciani, R., & Smaldone, L. A. 1985, A&A, 152, 165

Dorfi, E. A. & Drury, L. O. 1987, Journal of Computational Physics, 69, 175

Druett, M., Scullion, E., Zharkova, V., et al. 2017, Nature Communications, 8, 15905

Druett, M. K. & Zharkova, V. V. 2018, A&A, 610, A68

Druett, M. K. & Zharkova, V. V. 2019, A&A, 623, A20

Emslie, A. G. 1978, ApJ, 224, 241

Emslie, A. G. 1980, ApJ, 235, 1055

Emslie, A. G. & Brown, J. C. 1985, ApJ, 295, 648

Emslie, A. G., Dennis, B. R., Shih, A. Y., et al. 2012, ApJ, 759, 71

Emslie, A. G., Miller, J. A., & Brown, J. C. 2004, ApJL, 602, L69

Evans, J. S., Strickland, D. J., Woo, W. K., et al. 2010, Solar Phys., 262, 71

Fang, C. & Ding, M. D. 1995, A&AS, 110, 99

Faurobert, M., Fang, C., Corbard, T., et al. 2012, European Astronomical Society Publications Series, 55, 385

Fischler, M. A. & Bowles, J. C. 1981, Communications of the ACM, 24, 15

Fletcher, L., Dennis, B. R., Hudson, H. S., et al. 2011, Space Sci. Rev., 159, 19

Fletcher, L., Hannah, I. G., Hudson, H. S., & Metcalf, T. R. 2007a, ApJ, 656, 1187

Fletcher, L., Hannah, I. G., Hudson, H. S., & Metcalf, T. R. 2007b, in Astronomical Society of the Pacific Conference Series, Vol. 368, The Physics of Chromospheric Plasmas, ed. P. Heinzel, I. Dorotovič, & R. J. Rutten, Heinzel

Fletcher, L. & Hudson, H. S. 2008, ApJ, 675, 1645

Freeland, S. & Handy, B. 1998, Solar Physics, 182, 497

Gaunt, J. A. 1930, Philosophical Transactions of the Royal Society of London. Series A, Containing Papers of a Mathematical or Physical Character, 229, 163

Gluckstern, R. L. & Hull, M. H. 1953, Physical Review, 90, 1030

Gray, D. F. 2005, The Observation and Analysis of Stellar Photospheres

Griem, H. R., Kolb, A. C., & Shen, K. Y. 1959, Phys. Rev., 116, 4

Handy, B. N., Acton, L. W., Kankelborg, C. C., et al. 1999, Solar Phys., 187, 229

Hao, Q., Guo, Y., Dai, Y., et al. 2012, A&A, 544, L17

Heinzel, P. & Kleint, L. 2014, ApJL, 794, L23

Heinzel, P., Kotrč, P., Sobotka, M., Zloch, F., & Scherbakova, Z. A. 1986, Contributions of the Astronomical Observatory Skalnate Pleso, 15, 171

Hiei, E. 1982, Solar Phys., 80, 113

Hirayama, T. 1974, Solar Phys., 34, 323

Hock, R. A., Chamberlin, P. C., Woods, T. N., et al. 2012, Solar Physics, 275, 145

Högbom, J. A. 1974, A&AS, 15, 417

Holman, G. D. 2003, ApJ, 586, 606

Holman, G. D. 2012, ApJ, 745, 52

Holman, G. D., Aschwanden, M. J., Aurass, H., et al. 2011, Space Sci. Rev., 159, 107

Hubeny, I. 1985, Bulletin of the Astronomical Institutes of Czechoslovakia, 36, 1

Hubeny, I. 1997, in Lecture Notes in Physics, Berlin Springer Verlag, Vol. 497, Stellar Atmospheres: Theory and Observations, ed. J. P. De Greve, R. Blomme, & H. Hensberge, 1

Hubeny, I. & Mihalas, D. 2014, Theory of Stellar Atmospheres

Hudson, H. S., Fletcher, L., & Krucker, S. 2010, Mem. Societa Astronomica Italiana, 81, 637

Hudson, H. S., Wolfson, C. J., & Metcalf, T. R. 2006, Solar Phys., 234, 79

Hurford, G. J., Schwartz, R. A., Krucker, S., et al. 2003, ApJL, 595, L77

Ireland, J., Tolbert, A. K., Schwartz, R. A., Holman, G. D., & Dennis, B. R. 2013, ApJ, 769, 89

Jensch, A. 1959, Jenaer Rundschau, 4, 91

Jess, D. B., Mathioudakis, M., Christian, D. J., et al. 2010, Solar Phys., 261, 363

Jess, D. B., Mathioudakis, M., Crockett, P. J., & Keenan, F. P. 2008, ApJL, 688, L119

Kennedy, M. B., Milligan, R. O., Allred, J. C., Mathioudakis, M., & Keenan, F. P. 2015, A&A, 578, A72

Kerr, G. S. & Fletcher, L. 2014, ApJ, 783, 98

Kerr, G. S., Fletcher, L., Russell, A. J. B., & Allred, J. C. 2016, ApJ, 827, 101

Kerr, G. S., Simões, P. J. A., Qiu, J., & Fletcher, L. 2015, A&A, 582, A50

Kleint, L., Heinzel, P., Judge, P., & Krucker, S. 2016, ApJ, 816, 88

Knight, J. W. & Sturrock, P. A. 1977, ApJ, 218, 306

Kobylinskii, V. A. & Zharkova, V. V. 1996, Advances in Space Research, 17

Kopp, R. A. & Pneuman, G. W. 1976, Solar Phys., 50, 85

Kosugi, T., Makishima, K., Murakami, T., et al. 1991, Solar Phys., 136, 17

Kotrč, P. 2009, Central European Astrophysical Bulletin, 33, 327

Kotrč, P., Procházka, O., & Heinzel, P. 2016, Solar Phys., 291, 779

Kowalski, A. F., Allred, J. C., Daw, A. N., Cauzzi, G., & Carlsson, M. 2016, ArXiv e-prints

Kowalski, A. F., Allred, J. C., Uitenbroek, H., et al. 2017, ApJ, 837, 125

Kowalski, A. F., Hawley, S. L., Carlsson, M., et al. 2015, Solar Phys., 290, 3487

Kowalski, A. F., Hawley, S. L., Holtzman, J. A., Wisniewski, J. P., & Hilton, E. J. 2010, ApJL, 714, L98

Kowalski, A. F., Hawley, S. L., Holtzman, J. A., Wisniewski, J. P., & Hilton, E. J. 2012, Solar Phys., 277, 21

Kramers, H. A. 1923, The London, Edinburgh, and Dublin Philosophical Magazine and Journal of Science, 46, 836

Krucker, S., Christe, S., Glesener, L., et al. 2009, in Proceedings of the SPIE, Vol. 7437, Optics for EUV, X-Ray, and Gamma-Ray Astronomy IV, 743705

Kuhar, M., Krucker, S., Martínez Oliveros, J. C., et al. 2016, ApJ, 816, 6

Li, X. Q., Song, M. T., Hu, F. M., & Fang, C. 1997, A&A, 320, 300

Lin, R. P., Dennis, B. R., Hurford, G. J., et al. 2002, Solar Phys., 210, 3

Lin, R. P. & Hudson, H. S. 1976, Solar Phys., 50, 153

Lin, R. P. & Schwartz, R. A. 1987, ApJ, 312, 462

Litvinenko, Y. E. 1999, ApJ, 515, 435

Livshits, M. A., Badalian, O. G., Kosovichev, A. G., & Katsova, M. M. 1981, Solar Phys., 73, 269

Luzum, B., Capitaine, N., Fienga, A., et al. 2011, Celestial Mechanics and Dynamical Astronomy, 110, 293

Machado, M. E., Avrett, E. H., Falciani, R., et al. 1986, in The lower atmosphere of solar flares, p. 483 - 488, ed. D. F. Neidig, 483–488

Machado, M. E., Emslie, A. G., & Avrett, E. H. 1989, Solar Phys., 124, 303

Machado, M. E., Emslie, A. G., & Brown, J. C. 1978, Solar Phys., 58, 363

Machado, M. E. & Linsky, J. L. 1975, Solar Phys., 42, 395

Machado, M. E. & Rust, D. M. 1974, Solar Phys., 38, 499

Maehara, H., Shibayama, T., Notsu, S., et al. 2012, Nature, 485, 478

Makishima, K., Murakami, T., Nishimura, J., et al., eds. 1977, The modulation collimator as an imaging device

Martínez Oliveros, J.-C., Hudson, H. S., Hurford, G. J., et al. 2012, ApJL, 753, L26

Massone, A. M., Emslie, A. G., Kontar, E. P., et al. 2004, ApJ, 613, 1233

Matthews, S. A., van Driel-Gesztelyi, L., Hudson, H. S., & Nitta, N. V. 2003, A&A, 409, 1107

Mauas, P. J. D. 1990, ApJS, 74, 609

Mauas, P. J. D. & Falchi, A. 1996, A&A, 310, 245

McClintock, W. E., Rottman, G. J., & Woods, T. N. 2005, Solar Phys., 230, 225

McMaster, W. H. 1954, American Journal of Physics, 22, 351

McTiernan, J. M. & Petrosian, V. 1990, ApJ, 359, 524

Meegan, C., Lichti, G., Bhat, P. N., et al. 2009, ApJ, 702, 791

Mein, P. 1977, Solar Phys., 54, 45

Mertz, L. N., Nakano, G. H., & Kilner, J. R. 1986, Journal of the Optical Society of America A, 3, 2167

Metcalf, T. R., Alexander, D., Hudson, H. S., & Longcope, D. W. 2003, ApJ, 595, 483

Metcalf, T. R., Canfield, R. C., & Saba, J. L. R. 1990, ApJ, 365, 391

Metcalf, T. R., Hudson, H. S., Kosugi, T., Puetter, R. C., & Pina, R. K. 1996, ApJ, 466, 585

Mihalas, D. 1978, Stellar atmospheres /2nd edition/

Miller, J. A. & Roberts, D. A. 1995, ApJ, 452, 912

Milligan, R. O. & Chamberlin, P. C. 2016, A&A, 587, A123

Milligan, R. O., Kerr, G. S., Dennis, B. R., et al. 2014, ApJ, 793, 70

Murphy, R. J., Kozlovsky, B., Share, G. H., Hua, X.-M., & Lingenfelter, R. E. 2007, ApJS, 168, 167

Neidig, D. F. 1983, Solar Phys., 85, 285

Neidig, D. F. 1989, Solar Phys., 121, 261

Neupert, W. M. 1968, ApJL, 153, L59

Pesnell, W. D., Thompson, B. J., & Chamberlin, P. C. 2012, Solar Phys., 275, 3

Peterson, L. & Winckler, J. R. 1958, Physical Review Letters, 1, 205

Pettersen, B. R. 1989, Solar Phys., 121, 299

Potts, H., Hudson, H., Fletcher, L., & Diver, D. 2010, ApJ, 722, 1514

Procházka, O. 2014, Master's thesis, Astronomical Institute of Charles University, Prague

Procházka, O., Milligan, R. O., Allred, J. C., et al. 2017, ApJ, 837, 46

Procházka, O., Reid, A., & Mathioudakis, M. 2019, submitted to ApJ

Procházka, O., Reid, A., Milligan, R. O., et al. 2018, ApJ, 862, 76

Puetter, R. C. 1995, International Journal of Imaging Systems Technology, 6, 314

Radziszewski, K., Rudawy, P., & Phillips, K. J. H. 2007, A&A, 461, 303

Radziszewski, K., Rudawy, P., & Phillips, K. J. H. 2011, A&A, 535, A123

Reep, J. W., Russell, A. J. B., Tarr, L. A., & Leake, J. E. 2018, ApJ, 853, 101

Rubio da Costa, F., Kleint, L., Petrosian, V., Liu, W., & Allred, J. C. 2016, ApJ, 827, 38

Rust, D. M. & Hegwer, F. 1975, Solar Phys., 40, 141

Rutten, R. J. 2003, Radiative Transfer in Stellar Atmospheres

Rybicki, G. B. & Hummer, D. G. 1991, A&A, 245, 171

Rybicki, G. B. & Hummer, D. G. 1992, A&A, 262, 209

Rybicki, G. B. & Lightman, A. P. 1986, Radiative Processes in Astrophysics, 400

Saint-Hilaire, P. & Benz, A. O. 2005, A&A, 435, 743

Sato, J., Kosugi, T., & Makishima, K. 1999, PASJ, 51, 127

Scharmer, G. B. 1981, ApJ, 249, 720

Scharmer, G. B. & Carlsson, M. 1985, Journal of Computational Physics, 59, 56

Scherrer, P. H., Schou, J., Bush, R. I., et al. 2012, Solar Phys., 275, 207

Schou, J., Scherrer, P. H., Bush, R. I., et al. 2012, Solar Phys., 275, 229

Schwartz, R. A., Csillaghy, A., Tolbert, A. K., et al. 2002, Solar Phys., 210, 165

Shibata, K. 1999, in Proceedings of the Nobeyama Symposium, ed. T. S. Bastian, N. Gopalswamy, & K. Shibasaki, Vol. 479, 381–389

Simões, P. J. A., Kerr, G. S., Fletcher, L., et al. 2017, A&A, 605, A125

Smith, D. M., Lin, R. P., Turin, P., et al. 2002, Solar Phys., 210, 33

Struminsky, A. & Gan, W. 2015, in Journal of Physics Conference Series, Vol. 632, Journal of Physics Conference Series, 012081

Sturrock, P. A. 1966, Nature, 211, 695

Suematsu, Y., Tsuneta, S., Ichimoto, K., et al. 2008, Solar Phys., 249, 197

Švanda, M., Jurčák, J., Kašparová, J., & Kleint, L. 2018, The Astrophysical Journal, 860, 144

Syrovatskii, S. I. & Shmeleva, O. P. 1972, Soviet Astronomy, 16, 273

Tremblay, P.-E. & Bergeron, P. 2009, ApJ, 696, 1755

Trottet, G., Raulin, J.-P., Mackinnon, A., et al. 2015, Solar Phys., 290, 2809

Tsurutani, B. T., Gonzalez, W. D., Lakhina, G. S., & Alex, S. 2003, Journal of Geophysical Research (Space Physics), 108, 1268

Uitenbroek, H. 2001, ApJ, 557, 389

Uitenbroek, H. 2002, ApJ, 565, 1312

Ulmschneider, P., Muchmore, D., & Kalkofen, W. 1987, A&A, 177, 292

Švestka, Z. 1966a, Space Sci. Rev., 5, 388

Švestka, Z. 1966b, Bulletin of the Astronomical Institutes of Czechoslovakia, 17, 137

Švestka, Z. 1970, Solar Phys., 13, 471

Valníček, B., Letfus, V., Blaha, M., Švestka, Z., & Seidl, Z. 1959, Bulletin of the Astronomical Institutes of Czechoslovakia, 10, 149

van den Oord, G. H. J. 1990, A&A, 234, 496

Van Doorsselaere, T., Shariati, H., & Debosscher, J. 2017, ApJS, 232, 26

Vernazza, J. E., Avrett, E. H., & Loeser, R. 1981, ApJS, 45, 635

Vidal, C. R., Cooper, J., & Smith, E. W. 1970, JQSRT, 10, 1011

Vidal, C. R., Cooper, J., & Smith, E. W. 1971, JQSRT, 11, 263

Vidal, C. R., Cooper, J., & Smith, E. W. 1973, ApJS, 25, 37

Viereck, R., Hanser, F., Wise, J., et al. 2007, in Proceedings of the SPIE, Vol. 6689, Solar Physics and Space Weather Instrumentation II, 66890K

Vilmer, N., MacKinnon, A. L., & Hurford, G. J. 2011, Space Sci. Rev., 159, 167

Warmuth, A., Holman, G. D., Dennis, B. R., et al. 2009, ApJ, 699, 917

Warmuth, A. & Mann, G. 2016, A&A, 588, A115

Warren, H. P. 2006, ApJ, 637, 522

Watanabe, K., Kitagawa, J., & Masuda, S. 2017, ApJ, 850, 204

Westhoff, R. C., Rose, M. K., Gregory, J. A., et al. 2007, in Proceedings of the SPIE, Vol. 6686, UV, X-Ray, and Gamma-Ray Space Instrumentation for Astronomy XV, 668604

Winglee, R. M., Kiplinger, A. L., Zarro, D. M., Dulk, G. A., & Lemen, J. R. 1991, ApJ, 375, 366

Woods, T. N., Eparvier, F. G., Hock, R., et al. 2012, Solar Phys., 275, 115

Wuelser, J.-P., Lemen, J. R., Tarbell, T. D., et al. 2004, in Proceedings of the SPIE, Vol. 5171, Telescopes and Instrumentation for Solar Astrophysics, ed. S. Fineschi & M. A. Gummin, 111–122

Yu, H.-F., Preece, R. D., Greiner, J., et al. 2016, A&A, 588, A135

Zayer, I., Morrison, M., Pope, T., et al. 1995, in Astronomical Society of the Pacific Conference Series, Vol. 76, GONG 1994. Helio- and Astro-Seismology from the Earth and Space, ed. R. K. Ulrich, E. J. Rhodes, Jr., & W. Dappen, 456

Zharkova, V. & Zharkov, S. 2015, Solar Phys., 290, 3163

Zharkova, V. V. & Gordovskyy, M. 2006, ApJ, 651, 553

Zharkova, V. V. & Zharkov, S. I. 2007, ApJ, 664, 573